MULTI-RESOLUTION SIMULATIONS OF DELTA/DIAMOND WING AERODYNAMICS

A Dissertation

by

JACOB MARTIN COOPER

Submitted to the Office of Graduate and Professional Studies of
Texas A&M University
in partial fulfillment of the requirements for the degree of

DOCTOR OF PHILOSOPHY

Chair of Committee,	Sharath S. Girimaji
Committee Members,	Paul Cizmas
	Diego Donzis
	Hamn-Ching Chen
Head of Department,	Rodney Bowersox

August 2014

Major Subject: Aerospace Engineering

ABSTRACT

This dissertation investigates high angle of attack delta wing flow at multiple resolutions of turbulence closure. The work is divided into four studies. The objectives of each study are: (i) to identify the limits of RANS modeling, (ii) explore the challenges of applying the PANS model to the delta wing flow, (iii) identify the appropriate resolution required to capture specific flow features, and (iv) determine the physical differences between sharp and round leading edge separation.

The outcomes from each of these studies are as follows. Steady-state RANS modeling is shown to be adequate for low and moderate angles of attack, except in regions near the point of primary vortex separation. At low Reynolds number the vortex structure on the forward portion of the wing is mostly laminar and must be fully resolved by the grid in order to capture the physics in the aft region. Also at low Reynolds numbers, it is shown that lower resolution simulations perform adequately in capturing important integral flow features such as pressure coefficient and the locations of the vortex separation and attachment lines. High resolution simulations of low Reynolds number flow do resolve more subtle flow features that do not significantly affect the aerodynamic characteristics. The principle advantages of high resolution simulations are most evident at high Reynolds numbers and high angles of attack. The relationship between scale resolution and observed flow features is established. The simulations establish the key flow feature differences between round and sharp leading edge wing at different length scales of motion. Features of interest are the intensity of the vortex structure, the levels of turbulence, surface streamline patterns, and surface pressure coefficient. Differences between the delta and diamond wing shapes are also identified.

DEDICATION

This work is dedicated to my wife, Angie, my parents, Gary and Lisa, and all of my former teachers at Dulles Elementary, Henderson Elementary, Scharborough Elementary, DeZavala Elementary, Garcia Middle, and Austin High Schools.

ACKNOWLEDGEMENTS

I would like to thank several individuals and organizations who have contributed to my ability to attend graduate school, pursue studies in the aerospace field, and matriculate through Texas A&M University. This research has been supported for the past three years by the NASA NRA #NNXAI61A and I am very grateful for their support of my education. In conjunction with the funding support, I would like to aknowledge the guidance that I have received from Dr. Khaled Abdol-Hamid and Dr. Mohagna Pandya at NASA Langley Research Center for their collaboration with the research associated with the NASA NRA. Dr. Robert Baurle, also at NASA Langley Research Center must also be acknowledged for his tremendous support with the VULCAN CFD code which I have utilized for the entireity of this research. His knowledge of CFD is only outpaced by his patience for those of us who are learning to use it. I would also like to acknowledge Drs. Breitsamter and Hovelmann at the Technische Universitat Munchen for the experimental force and pressure data used throughout this document.

In the Aerospace Engineering department at Texas A&M University, I would like to acknowledge the guidance of Karen Knabe for her dependability and guidance. In addition, Colleen Leatherman was instrumental in organizing the travel arrangements for the conferences which I attended and also for making the arrangements for conferences which were hosted at our department. In both instances, my education was enhanced because of the effort which she gave to make those experiences happen.

Next, thank you to my PhD committee members, Dr. Paul Cizmas, Dr. Diego Donzis, and Dr. Hamn-Ching Chen. Each of the courses which I took from you, whether as an undergraduate or graduate student, were integral to my education.

Your input at my preliminary exam was also beneficial in challenging me to improve the quality of my work for this past year.

Finally, and most importantly, I would like to thank Dr. Sharath Girimaji for taking on the responsibility to be my committee chair and academic advisor for the past five years. I have had the priviledge to take every one of your undergraduate and graduate courses, and I would not have been able to achieve this great accomplishment if it were not for everything you have taught me both inside and outside of the classroom.

TABLE OF CONTENTS

Page

LIST OF FIGURES

FIGURE Page

LIST OF TABLES

TABLE Page

1. INTRODUCTION

1.1 Fluid Dynamics Background

In the aerospace community, aerodynamic performance predictions are made from the use of three methods: (i) aerodynamic analytic theory, (ii) wind tunnel experiments, or (iii) computational fluid dynamics (CFD) simulations. The utility of aerodynamic analytic theory is limited to only the most simple (often trivial) geometries and usually requires so many simplifying assumptions as to render the theory virtually useless in practical application. Wind tunnel experiments have yielded a tremendous amount of aerodynamic data for thousands of airfoils, wings, and fully configured airplanes. However, wind tunnel experiments are limited by measurement techniques and instabilities in freestream conditions, among other issues. As computer processing power has continued to increase over the previous decade, the use of CFD for aerodynamic performance prediction and analysis has increased as well. CFD can be a very useful tool by providing a myriad of flow properties at any point in the flow domain. However, the limitations of CFD are many: cumbersome grid generation, numerical method stability, turbulence modeling accuracy, and limited computational resources. Although the work presented in the following sections utilizes the CFD approach, in practice, each of these three aerodynamic prediction methods should be used in concert with each other throughout the design and development process.

CFD simulations attempt to provide numerical solutions to the Navier Stokes equations which are the governing equations for fluid flow. The Navier Stokes equations are a system of equations which include the continuity equation (conservation of mass) and three equations for conservation of momentum in the three cartesian

directions.

$$\frac{\partial u_i}{\partial x_i} = 0 \tag{1.1}$$

$$\rho \frac{\partial u_i}{\partial t} + \rho u_j \frac{\partial u_i}{\partial x_j} = -\frac{\partial p}{\partial x_i} + \frac{\partial}{\partial x_j}\left(2\mu s_{ji}\right) \tag{1.2}$$

The Navier Stokes equations, while complex (even chaotic) in nature, are simply a manifestation of Newton's Second Law of Motion applied to a continuous medium. In order to numerically solve the Navier Stokes equations, the equations must be discretized using a finite-difference, finite-element, or finite-volume method. In addition, the domain of interest must be discretized, usually done through the use of some grid generation software. The resolution of the grid which is required for a particular simulation is dependent upon many factors, but perhaps the most important factor is turbulence.

Nearly every fluid flow which is of practical interest to the aerospace community is a turbulent flow. For very low speed flows or extremely viscous flows, where viscous diffusion of momentum is dominant, the equations of motion have a steady, predictable solution. This state of fluid flow is called laminar. However, at higher flow speeds or lower levels of viscosity, the inertia of the fluid is able to overcome viscous diffusion and the steady laminar flow becomes unsteady and fluctuations of velocity and pressure are generated in all three dimensions. This state of fluid motion is called turbulent. It can be an esoteric exercise to precisely define what makes a turbulent flow turbulent. Usually, the preferred course of action is to describe the basic properties that all turbulent flows exhibit. Turbulent flows are three-dimensional with swirling motions called eddies. These eddies comprise a wide range of scales; that is, a turbulent flow will have eddies which are as large as the flow geometry and eddies which are many times smaller than the flow geometry. The

greater inertia that the flow possesses, the wider the disparity between the largest and smallest eddies. Turbulent flows are also dissipative because these small eddies dissipate energy from the flow through viscous action. The vorticity contained in the turbulent eddies diffuses mass and momentum very well which means that turbulent flows are also very good at mixing.

It is clear from the preceeding discussion that in any flow the ratio of the inertial forces of the flow to the viscous forces in the flow play the leading role in determining whether a flow is laminar or turbulent. This ratio is the Reynolds number: $Re \equiv \rho U L/\mu$ where ρ is the fluid density, U and L are the characteristic velocity and length scales of the flow respectively, and μ is the fluid viscosity. Returning to the discussion of grid resolution for a turbulent flow, the number of grid cells required to resolve the smallest scale of motion is: $N \sim Re^{9/4}$. Therefore, given a turbulent flow at a particular Reynolds number, at one end of the grid resolution spectrum is a very fine grid which fully resolves even the smallest motions in the flow domain. Using such a grid in a simulation of the Navier Stokes equations is called a direct numerical simulation (DNS). Fully resolved DNS simulations are valuable predictive tools, however they are currently restricted to extremely simple flow geometries and/or very low Reynolds numbers due to the extreme computational cost.

At the other end of the grid resolution spectrum is another approach where a much more coarse grid is used in order to only resolve the mean flow while modeling the effects of any fluctuating scales of motion. Such an approach is possible because the turbulent fluctuations, particularly at small scales, behave in a random manner which allows for the use of averaged statistics. The averaging approach was pioneered by Reynolds [44], who introduced the concept of decomposing the velocity and pressure

fields into the sum of a mean and a fluctuating part.

$$u_i = \overline{U}_i + u_i'; \quad p = \overline{P} + p' \tag{1.3}$$

A spatial or time average is applied to the Navier-Stokes equations and the resulting equations for the mean flow are termed the Reynolds-avgeraged Navier Stokes (RANS) equations.

$$\frac{\partial \overline{U}_i}{\partial x_i} = 0 \tag{1.4}$$

$$\rho \frac{\partial \overline{U_i}}{\partial t} + \rho \frac{\partial}{\partial x_j} \left(\overline{U}_j \overline{U}_i + \overline{u_j' u_i'} \right) = -\frac{\partial \overline{P}}{\partial x_i} + \frac{\partial}{\partial x_j} \left(2\mu S_{ji} \right) \tag{1.5}$$

The RANS equations are identical in form to the full Navier Stokes equations except for the appearance of the $\overline{u_j' u_i'}$ term, which is typically called the Reynolds Stress term. The field of turbulence modeling, and much of the remainder of this paper, is dedicated to understanding this term and deriving an evolution equation for it in order to accurately predict turbulent flows.

A wide range of approaches for modeling the Reynolds stress can be adopted, from very simple algebraic models to very complex evolution equations which can be derived for each term in the Reynolds stress tensor. The exact Reynolds stress evolution equation is the subject of ongoing turbulence modeling research [19]. A simpler, more common approach is the so-called Boussinesq approximation which postulates that the Reynolds stress can be closed via the following constitutive relationship:

$$-\overline{u_i' u_j'} = 2\nu_t S_{ij} - \frac{2}{3} k \delta_{ij}. \tag{1.6}$$

The preceding relationship is analogous to the consitutive relationship for fluid

viscosity which manifests itself in a flow as shear stress. Therefore the ν_t term is called the eddy viscosity, under the analogy that the Reynolds stress is manifested through the interaction of turbulent eddies. One key assumption which is implicit in the Boussinesq approximation is that the principal axes of the Reynolds stress tensor are aligned with the principle axes of the mean flow gradient tensor (S_{ij}). This assumption is invalid for large scale turbulent fluctuations, and thus it is very difficult to develop an appropriate model for the large scale turbulent structures while utilizing such an assumption. The preceeding equation requires closure for the eddy viscosity, ν_t, and the turbulence kinetic energy, k. One common closure approach, the $k-\omega$ model [51], is presented here.

$$\nu_t = \frac{k}{\omega} \tag{1.7}$$

$$\frac{\partial k}{\partial t} + \overline{U}_j \frac{\partial k}{\partial x_j} = P - \beta^* k\omega + \frac{\partial}{\partial x_j}\left[\left(\nu + \frac{\nu_t}{\sigma_k}\right)\frac{\partial k}{\partial x_j}\right] \tag{1.8}$$

$$\frac{\partial \omega}{\partial t} + \overline{U}_j \frac{\partial \omega}{\partial x_j} = \alpha \frac{P\omega}{k} - \beta\omega^2 + \frac{\partial}{\partial x_j}\left[\left(\nu + \frac{\nu_t}{\sigma_\omega}\right)\frac{\partial \omega}{\partial x_j}\right] \tag{1.9}$$

The closure coefficients which are derived from simplified flows such as homogeneous shear, decaying isotropic turbulence, and the log-law, take the following values:

$$\alpha = \frac{13}{25}; \quad \beta = 0.0708; \quad \beta^* = \frac{9}{100}; \quad \sigma_k = 2.0; \quad \sigma_\omega = 2.0 \tag{1.10}$$

When computing a viscous flow, most CFD practicioners in industry today rely upon RANS models which utilize the aforementioned $k-\omega$ or some other similar turbulence model. The widespread use of RANS closure models is due to their ability to deliver a solution with a coarse grid at relatively low computational cost. However, for wall-bounded flows the utility of RANS models is limited to situations

where the streamlines are attached to the surface. In practice, many aerospace flows are much more complex involving areas of flow separation and reattachment. RANS closure models have not shown to be reliable at predicting separation [8], and often drastically over-predict the level of eddy viscosity in separated flow regions [5]. This over-prediction of eddy viscosity effectively reduces the Reynolds number of the simulation inhibiting the development of fine-scale turbulent structures. It is clear that for many applications, especially for flows with large separation, RANS is not capable of delivering the level of resolution which is required by the fluid dynamics community.

Another common approach to numerically simulating a turbulent flow is called a large eddy simulation (LES). The distinguishing feature of the LES model is that it requires a grid which can resolve the majority of the turbulent energy spectrum, and therefore only models the smallest turbulent scales. Whereas the RANS equations are derived by taking a mean of the Navier-Stokes equations, the LES equations are derived by applying a filter to the Navier-Stokes equations. In the filtering process, a cutoff scale Δ is introduced which separates the resolved scales from the subgrid scales. Once filtered, the form of the filtered Navier-Stokes equations is similar to that of the Reynolds Averaged equations:

$$\frac{\partial \overline{U}_i}{\partial x_i} = 0 \tag{1.11}$$

$$\frac{\partial \overline{U}_i}{\partial t} + \frac{\partial}{\partial x_j}\left(\overline{U}_i \overline{U}_j\right) = -\frac{1}{\rho}\frac{\partial P}{\partial x_j} + \frac{\partial}{\partial x_j}\left[\nu \frac{\partial \overline{U}_i}{\partial x_j} + \tau_{ij}\right] \tag{1.12}$$

where τ_{ij} is the sub-grid stress (SGS) term. Smagorinsky [45] proposed the first model for the SGS term by assuming that the sub-grid stresses behave according to

a gradient-diffusion process.

$$\tau_{ij} = 2\nu_T S_{ij}; \qquad \nu_T = (C_s\Delta)^2 \sqrt{S_{ij}S_{ij}} \tag{1.13}$$

where C_s is the Smagorinsky coefficient and is usually set to a constant value. LES has shown considerable improvement in modeling complex separated flows [5]. However, practicioners are doubtful that meaningful, high Reynolds number simulations relevant to the aerospace community are feasible due to the high computational cost of LES [48]. Due to this high computational burden, LES simulations are mostly restricted to canonical flows and academic research.

In recent years a hybrid turbulence modeling paradigm has emerged to bridge the gap between cost-effective RANS simulations and higly resolved, yet expensive LES and DNS. These hybrid methods can broadly be categorized into zonal methods or bridging methods. Detatched-eddy simulation (DES) is an example of a zonal method and is derived in [48]. The DES model blends the efficiency of RANS with the accuracy of LES by employing the RANS model in regions near solid surfaces and LES in regions away from the wall. Such simulations have become very common in industry today. The Partially-averaged Navier Stokes (PANS) model is an example of a bridging method. It is a variable resolution model which can blend smoothly from RANS to DNS through the use of a variable resolution filter. The PANS model is the primary focus of the remainder of this research, and its derivation is provided in the following section.

1.2 PANS Governing Equations

The PANS model is derived by decomposing the flow into the sum of a resolved and unresolved part, followed by applying an arbitrary filter which commutes with

temporal and spatial differentiation to the Navier Stokes equations [9].

$$u_i = \langle u_i \rangle + u_i'; \quad p = \langle p \rangle + p'; \quad \tau\big(u_i, u_j\big) = \langle u_i u_j \rangle - \langle u_i \rangle \langle u_j \rangle \tag{1.14}$$

$$\frac{\partial \langle u_k \rangle}{\partial x_k} = 0 \tag{1.15}$$

$$\frac{\partial \langle u_i \rangle}{\partial t} + \frac{\partial \langle u_i \rangle \langle u_j \rangle}{\partial x_j} = -\frac{\partial \langle p \rangle}{\partial x_i} + 2\nu \frac{\partial \langle s_{ij} \rangle}{\partial x_j} - \frac{\partial \tau\big(u_i, u_j\big)}{\partial x_j} \tag{1.16}$$

After application of the filter, an additional term emerges $\tau\left(u_i, u_j\right)$ which is called the generalized central moment. This filtering approach utilizes an arbitrary filter, and is therefore a general approach. On the other hand, Reynolds averaging employs either a time-average or ensemble-average, which can be viewed as a sub-set of the general averaging employed above. The generalized central moment term is analogous to the Reynolds stress term which appears after Reynolds-averaging and the sub-filter stress (SFS) in the context of LES. The preceding equations are filter invariant, and subsequently the generalized central moment term is invariant to the type of averaging.

The RANS equations resolve only the mean flow and model the entire turbulence energy spectrum. The PANS model is a variable resolution model which purports to model a user-specified portion of the turbulence energy spectrum. The resolution is determined by the filter control parameters:

$$f_k = \frac{k_u}{k}; \qquad f_\varepsilon = \frac{\varepsilon_u}{\varepsilon} \tag{1.17}$$

The parameter f_k, which may vary between zero and unity, specifies the ratio of unresolved-to-total turbulence kinetic energy. A value of zero for f_k indicates that none of the turbulence energy spectrum is unresolved; the entire spectrum must be

resolved by the grid. A value of unity for f_k indicates that the entire spectrum is unresolved which is identical to a RANS simulation. In essence, the f_k parameter specifies the spectral cutoff for the simulation. The following derivation will formally demonstrate that the PANS equations reduce to DNS for $f_k = 0$ and the PANS equations reduce to RANS for $f_k = 1$. The parameter f_ε specifies the ratio of unresolved-to-total dissipation, and it may also vary between zero and unity. The value for f_ε will be unity unless the spectral cutoff is in the dissipative scales. The present derivation will follow a $k-\omega$ paradigm, thus we also must specify the ratio of unresolved-to-total turbulence frequency:

$$f_\omega = \frac{\omega_u}{\omega} = \frac{\varepsilon_u / (\beta^* k_u)}{\varepsilon / (\beta^* k)} = \frac{f_\varepsilon}{f_k}. \tag{1.18}$$

After specification of the spectral cutoff, one must choose an approach to close the generalized central moment term and thereby model the unresolved field. With PANS modeling, we intend to resolve the dynamically important scales, but significantly less scales than a typical LES. Since the cutoff will typically be between RANS and LES, we require a sub-filter closure model which is more sophisticated than LES. For this reason, and the robustness of two-equation RANS models, we choose to use a Boussinesq-like two-equation closure approach for the PANS unresolved field.

$$\tau(u_i, u_j) = -\nu_u \left(\frac{\partial \langle u_i \rangle}{\partial x_j} + \frac{\partial \langle u_j \rangle}{\partial x_i} \right) + \frac{2}{3} k_u \delta_{ij}; \quad \nu_u = \frac{k_u}{\omega_u} = \frac{f_k k}{f_\omega \omega} \tag{1.19}$$

We proceed to derive evolution equations for the PANS unresolved kinetic energy k_u and the unresolved turbulence frequency ω_u, taking inspiration from the original RANS 1988 Wilcox $k-\omega$ model [51] given in Eqs. 1.8 and 1.9. The evolution of kinetic energy for the PANS equations can be found via the definition of the filter

control parameter f_k.

$$\frac{\partial k_u}{\partial t} + \overline{U}_j \frac{\partial k_u}{\partial x_j} = f_k \left(\frac{\partial k}{\partial t} + \overline{U}_j \frac{\partial k}{\partial x_j} \right) + \dot{f}_k k \tag{1.20}$$

This work will only consider constant f_k cases so $\dot{f}_k = 0$. The evolution of unresolved kinetic energy can be written in the classical RANS form:

$$\frac{\partial k_u}{\partial t} + \overline{U}_j \frac{\partial k_u}{\partial x_j} = P_u - \beta^* k_u \omega_u + T_{ku} \tag{1.21}$$

$$P_u = \tau \left(u_i, u_j \right) \frac{\partial \overline{U}_i}{\partial x_j} \tag{1.22}$$

$$T_{ku} = \frac{\partial}{\partial x_j} \left(\frac{\nu_t}{\sigma_k} \frac{\partial k_u}{\partial x_j} \right) \tag{1.23}$$

The RANS kinetic energy equation 1.8 can be substituted into the PANS kinetic energy equation 1.20 to arrive at:

$$\frac{\partial k_u}{\partial t} + \langle u_j \rangle \frac{\partial k_u}{\partial x_j} = f_k \left[P - \beta^* k \omega + \frac{\partial}{\partial x_j} \left(\frac{\nu_t}{\sigma_k} \frac{\partial k}{\partial x_j} \right) \right] + \left(\langle u_j \rangle - \overline{U_j} \right) \frac{\partial k_u}{\partial x_j} \tag{1.24}$$

and the left-hand-side can be rewritten using the proposed evolution of the unresolved kinetic energy:

$$P_u - \beta^* k_u \omega_u + T_{ku} = f_k \left[P - \beta^* k \omega + \frac{\partial}{\partial x_j} \left(\frac{\nu_t}{\sigma_k} \frac{\partial k}{\partial x_j} \right) \right] + \left(\langle u_j \rangle - \overline{U_j} \right) \frac{\partial k_u}{\partial x_j} \tag{1.25}$$

The production and destruction terms can be equated to examine the relationship between RANS and PANS:

$$P_u - \beta^* k_u \omega_u = f_k \left[P - \beta^* k \omega \right] \tag{1.26}$$

and recalling the relationship between PANS and RANS variables $\omega = \omega_u/f_\omega$ and $k = k_u/f_k$:

$$P = \frac{1}{f_k}\left(P_u - \beta^* k_u \omega_u\right) + \beta^* \frac{k_u \omega_u}{f_\omega f_k} \tag{1.27}$$

This relationship will be used in the derivation of the transport equation for ω_u. Likewise, the transport terms can be equated:

$$T_{ku} + \left(\overline{U_j} - \langle u_j \rangle\right) \frac{\partial k_u}{\partial x_j} = f_k \frac{\partial}{\partial x_j}\left(\frac{\nu_t}{\sigma_k}\frac{\partial k}{\partial x_j}\right) = \frac{\partial}{\partial x_j}\left(\frac{\nu_t}{\sigma_k}\frac{\partial k_u}{\partial x_j}\right) \tag{1.28}$$

$$T_{ku} \equiv \frac{\partial}{\partial x_j}\left(\frac{\nu_t}{\sigma_k}\frac{\partial k_u}{\partial x_j}\right) - \left(\overline{U_j} - \langle U_j \rangle\right) \frac{\partial k_u}{\partial x_j} = \frac{\partial}{\partial x_j}\left(\frac{\nu_u f_\omega}{\sigma_k f_k}\frac{\partial k_u}{\partial x_j}\right) - \left(\overline{U_j} - \langle u_j \rangle\right) \frac{\partial k_u}{\partial x_j} \tag{1.29}$$

where $\nu_u = \left(f_k/f_\omega\right)\nu_t$. The $\left(\overline{U_j} - \langle u_j \rangle\right)\left(\partial k_u/\partial x_j\right)$ term on the right-hand-side of the equation represents the transport of unresolved kinetic energy due to the resolved velocity fluctuations. This is the only term in the above equation which requires further closure. There are two approaches to properly closing this term.

The first transport closure approach is to assume that the resolved fluctuating scales do not significantly contribute to the transport of kinetic energy due to the disparate length and time scales of the resolved and unresolved fields. This was shown to be true for PANS $k_u - \varepsilon_u$ closure by Murthi [38]. This assumtion is termed the Zero Transport Model (ZTM) and it leads to the following:

$$\left(\overline{U_j} - \langle u_j \rangle\right) \frac{\partial k_u}{\partial x_j} = 0; \qquad T_{ku} = \frac{\partial}{\partial x_j}\left(\frac{\nu_u}{\sigma_{ku}}\frac{\partial k_u}{\partial x_j}\right); \qquad \sigma_{ku} \equiv \sigma_k \frac{f_k}{f_\omega}. \tag{1.30}$$

The second transport closure approach is to assume that the resolved-scale transport is proportional to the eddy viscosity. This assumption is termed the Maximum

Transport Model (MTM):

$$\left(\overline{U_j} - \langle u_j \rangle\right) \frac{\partial k_u}{\partial x_j} \approx \frac{\partial}{\partial x_j}\left(\frac{\nu_r}{\sigma_k}\frac{\partial k_u}{\partial x_j}\right); \qquad \nu_r = \nu_t - \nu_u; \qquad \sigma_{ku} \equiv \sigma_k. \tag{1.31}$$

After adopting either of these assumtions (ZTM or MTM), the modeling of the PANS unresolved kinetic energy equation is complete.

The PANS unresolved turbulence frequency equation is derived in a similar way starting with the definition of $f_\omega = \omega_u/\omega$ and the RANS equation for ω:

$$\frac{\partial \omega_u}{\partial t} + \overline{U}_j \frac{\partial \omega_u}{\partial x_j} = f_\omega \left(\frac{\partial \omega}{\partial t} + \overline{U}_j \frac{\partial \omega}{\partial x_j}\right) = f_\omega \left(\alpha \frac{P\omega}{k} - \beta\omega^2 + \frac{\partial}{\partial x_j}\left(\frac{\nu_t}{\sigma_\omega}\frac{\partial \omega}{\partial x_j}\right)\right) \tag{1.32}$$

The RANS dependent variables can be expressed in terms of the PANS dependent variables by using the definitions of the filter control parameters.

$$\frac{\partial \omega_u}{\partial t} + \langle u_j \rangle \frac{\partial \omega_u}{\partial x_j} = \alpha \frac{P\omega_u}{k_u} f_k - \beta \frac{\omega_u^2}{f_\omega} + \frac{\partial}{\partial x_j}\left(\frac{\nu_t}{\sigma_\omega}\frac{\partial \omega_u}{\partial x_j}\right) + \left(\langle u_j \rangle - \overline{U}_j\right) \frac{\partial \omega_u}{\partial x_j} \tag{1.33}$$

The RANS kinetic energy production, P is closed via equation 1.27, and the transport due to the resolved fluctuating scales:

$$\frac{\partial \omega_u}{\partial t} + \langle u_j \rangle \frac{\partial \omega_u}{\partial x_j} = \alpha \frac{P_u \omega_u}{k_u} - \beta' \omega_u^2 + \frac{\partial}{\partial x_j}\left(\frac{\nu_u}{\sigma_{\omega u}}\frac{\partial \omega_u}{\partial x_j}\right) \tag{1.34}$$

where the definition of β' emerges after substituting P into the PANS equation

$$\beta' = \alpha\beta^* - \frac{\alpha\beta^*}{f_\omega} + \frac{\beta}{f_\omega} \tag{1.35}$$

Once again, there are two choices for closure of the transport term, and one can

choose to utilize the ZTM assumption leading to:

$$\sigma_{\omega u} \equiv \sigma_\omega \frac{f_k}{f_\omega} \tag{1.36}$$

or the MTM assumption:

$$\sigma_{\omega u} \equiv \sigma_\omega. \tag{1.37}$$

The final form of the PANS $k-\omega$ model equations can be summarized as:

$$\frac{\partial k_u}{\partial t} + \langle u_j \rangle \frac{\partial k_u}{\partial x_j} = P_u - \beta^* k_u \omega_u + \frac{\partial}{\partial x_j}\left[\left(\nu + \frac{\nu_u}{\sigma_{ku}}\right)\frac{\partial k_u}{\partial x_j}\right] \tag{1.38}$$

$$\frac{\partial \omega_u}{\partial t} + \langle u_j \rangle \frac{\partial \omega_u}{\partial x_j} = \alpha \frac{P_u \omega_u}{k_u} - \beta' \omega_u^2 + \frac{\partial}{\partial x_j}\left[\left(\nu + \frac{\nu_u}{\sigma_{\omega u}}\right)\frac{\partial \omega_u}{\partial x_j}\right] \tag{1.39}$$

The RANS closure coefficients are unchanged for α and β^*, while the remaining closure coefficients are modified using the ZTM assumption as given below:

$$\sigma_{ku} \equiv \sigma_k \frac{f_k}{f_\omega}; \qquad \beta' \equiv \alpha\beta^* - \frac{\alpha\beta^*}{f_\omega} + \frac{\beta}{f_\omega}; \qquad \sigma_{\omega u} \equiv \sigma_\omega \frac{f_k}{f_\omega} \tag{1.40}$$

The user can achieve accuracy-on-demand by varying the filter control parameter from a coarse RANS simulation to a fully-resolved DNS simulation, provided that the grid can support such a resolution. The original derivation of the PANS model is performed by Girimaji [10], and its validity has been established in various works: [28], [37], [47], [11], and [27].

1.3 Delta Wing Background and Literature

Recently, the delta wing has received renewed interest due to its potential application in unmanned combat aerial vehicles (UCAVs). In unmanned combat, the

vehicle is expected to encounter a wider flight envelope than a manned aircraft would, including extreme angles of attack and roll. The delta wing geometry is useful in practice because of its ability to maintain lift and its stability and control properties without the need of additional flow control devices at angles of attack which would be well past stall for traditional geometries. The aerodynamic performance of the delta wing must be well understood at these limits of the flight envelope. Delta wing aerodynamics is characterized by large vortices which separate from the leading edge of the wing creating a complex separated flow field. At low angles of attack and low Reynolds numbers the vortical flow is relatively steady, however with increasing angles of attack and Reynolds number, the flow features become progressively more unsteady with increasingly more broad spectrum turbulence. The delta wing has received considerably less attention in literature than traditional wings and airfoils. Although some of the elementary features of the delta wing flow are known, more work needs to be done to establish different features occuring at different scales of resolution. It is also important to establish which small scale features impact the integrated wing properties such as the surface pressure and lift coefficients.

The dominant flow features which are of interest for the delta wing are the location of primary and secondary vortex separation and reattachment, the alignment of the vortex structure, and the location of vortex breakdown. These flow features are dependent upon the wing shape, leading edge radius, leading edge sweep angle, angle of attack, and Reynolds number. As modern UCAVs are likely to employ moderate sweep angles near 50^o, so-called nonslender delta wings warrant further study. The sharp leading edge delta wing presents a less demanding challenge to simulate as compared to the round leading edge case. The computational burden can also be eased by simulating the delta wing at low Reynolds number. Although the low Reynolds number simulations are not representative of realistic flight conditions,

they are useful for evaluating the performance of numerical models at capturing the relevant flow physics.

The literature describing the flow features of sharp leading edge delta wing flow is summarized here. The earliest studies analyzed delta wings with large ($> 60^o$) leading edge sweep angles and sharp leading edges [41] [20] [29] [46]. For delta wings with sharp leading edges, the vortex will always separate at the sharp leading edge, beginning at the wing apex. The abrupt separation creates a shear layer where the fast-moving freestream interfaces with the slow-moving fluid on the suction side of the wing. The shear layer rolls up into a distinct primary vortex and is drawn towards the wing centerline and then down towards the surface of the wing where it reattaches. The intensity of the vortex is highest near the apex of the wing. The tightly-wound vortex behaves like a jet flow, accelerating fluid through its core creating a potent suction on the upper surface of the wing. For a schematic of the vortex flow, see Fig. 1.1.

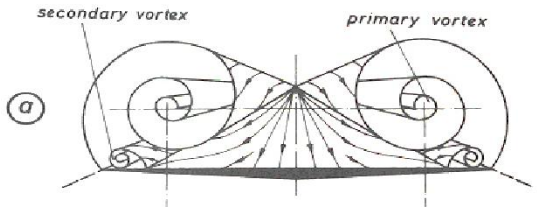

Figure 1.1: Primary and Secondary Vortex Sheets Schematic (Reprinted with permission from: Dietrich Hummel. "On the Vortex Formation Over a Slender Delta Wing at Large Angles of Incidence." Technical Report 15, Technische Universitat Braunschweig, 1978. [20])

After reattachment of the primary vortex, the surface streamlines are drawn outward towards the leading edge due to the presence of the strong suction in the vortex

core. Once the surface streamlines pass the axis of the vortex core, a strong adverse pressure gradient is encountered. Eventually, the adverse pressure gradient causes the reattached flow to separate into a secondary vortex beneath the larger primary vortex, with the opposite sign of vorticity. It is well-known that, compared to a laminar boundary layer, a turbulent boundary layer is able to withstand such an adverse pressure gradient for a greater distance before separating. This is also true for the present vortex flow case; a laminar reattached boundary layer will promote secondary vortex separation and cause the secondary vortex to be located more inboard compared to a turbulent reattached boundary layer. Thus the laminar/turbulent status of the reattached boundary layer plays a role in determining the structure of the primary/secondary vortex formation. In the region close to the wing apex, the traditional primary/secondary vortex structure is steady and appears to be laminar for many cases which have been studied. As expected, for low Reynolds numbers the well-defined primary/secondary vortex structure maintains its integrity for some distance downstream, while high Reynolds number flows experience instabilities which degrade the well-defined structure of the primary/secondary vortices closer to the wing apex. The boundary layer from the lower surface of the wing plays no significant role in the shear layer, especially in the wing apex region where there is insufficient distance for an appreciable boundary layer to develop on the lower surface.

As the vortical structures convect downstream, unsteady instabilities appear. The instabilities pertinent to the separated vortices have been the topic of extensive research. The unsteady instabilities have been attributed to the well known Kelvin-Helmholtz instability by several authors [7], [40], [30], and [14]. Alternatively, Gursul [17] concluded that the dominant unsteadiness arises from the shear layer following a helical path around the vortex core, termed the helical mode instability. On the

interior of the vortex strucutre, the secondary vortex interacts with the primary vortex and the separated shear layer, further complicating the stability and structure of the flow field.

After sufficent distance, the various instabilities in the vortex structure grow and cause the vortex to breakdown. The vortex breakdown is characterized by the loss of a definitive axial vortex core, a switch from a jet-like core to a wake-like region, large velocity fluctuations, and greater turbulence. The breakdown of the primary vortex can adversely influence the performance of the delta wing in a number of ways: buffeting, loss of lift, and unstable pitching and roll behavior. The multi-scale vortical flow features can be seen in Fig. 1.2 which shows the axial vorticity at Re=620,000.

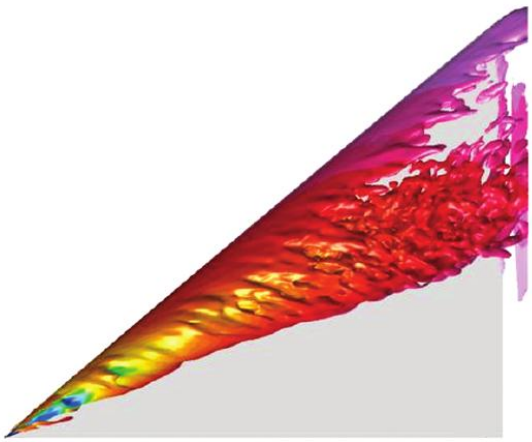

Figure 1.2: Vortical Structures at Large and Small Scales; Re=620,000 [16]

The vortex breakdown process has been the topic of great interest and debate in literature. In general, two separate types of vortex breakdown have been documented: spiral and bubble. In both cases, the location of breakdown is determined by the location where the vortex changes from a jet-like behavior to a wake-like

behavior, and an abrupt expansion in the vortex core. The bubble-type breakdown occurs with a stagnation point along the vortex core, followed by an oval-shaped, symmetric expansion of the core. The spiral-type breakdown exhibits a similar character, however the rapid expansion of the vortex core does not occur symmetrically; instead the streamlines follow a spiral around the expanding core. Gordnier [15] indicates that a 3D stagnation point does not exist for the spiral-type breakdown. The expansion of the vortex core occurs more rapidly for the bubble-type breakdown compared to the spiral-type breakdown. There remains considerable debate as to whether the bubble and spiral breakdown types are the only types of breakdown processes.

As expected, vortex breakdown is affected by the same flow parameters which affect the pre-breakdown vortex structure. An increase in angle of attack tends to move the vortex breakdown location forward until the limit of stall where there is no longer a distinct vortex. An increase in leading edge sweep, however, tends to move the vortex breakdown location aft. The breakdown location for wings with a sharp leading edge is not strongly influenced by Reynolds number, however the Reynolds number does influence the turbulence levels in the wake of the vortex. The presence (or absence) of pressure fluctuations has a profound effect on the breakdown location. The geometry of the wing apex region also plays a significant role in the breakdown dynamics [31], along with the geometry of the leading edge. The location of vortex breakdown may also oscillate over a distance as much as 10% of the wing chord for very large incidence angles. The osciallation appears to be related to the fluid dynamics of the primary vorticies, and not related to facility-related disturbances, the Kelvin-Helmholtz instability, or the helical mode instability due to the disparate frequencies of each [35].

In this work, we will focus our attention on the delta wing geometries with leading

edge sweep angles near 50^o because of their potential for use in UCAVs. The previous literature specific to sharp leading edge delta wings with 50^o leading edge sweep is summarized here. A high-fidelity CFD data set was generated by the direct numerical simulation (DNS) study of Gordnier and Visbal [13]. Their DNS computes a sharp leading edge delta wing with 50^o sweep angle at $Re = 26,000$ at 5^o, 10^o, and 15^o angle of attack using a 6th order compact differencing scheme, with an 8th order low pass spatial filter. The results from [13] mostly include visualizations of flow features such as a dual primary vortex structure, the presence of a strong secondary vortex, and unsteady features such as vortex breakdown, and Rayleigh-Taylor-like instabilities in the vortex shear layer. Gordnier et al [16] have performed 6th-order implicit LES on the same 50^o swept delta wing at more realistic flight Reynolds numbers: $Re = 2.0e5$, $Re = 6.2e5$, and $Re = 2.0e6$ and at an angle of attack $\alpha = 15^o$ which produces a large primary vortex and a distinct location of breakdown. Experimental PIV data were obtained for the two lower Reynolds number. Taylor and Gursul [49] have performed an experimental investigation of a sharp leading edge delta wing with 50^o leading edge sweep. Experiements were performed in a water tunnel to study the delta wing at a low Reynolds number of $26,000$ and in a wind tunnel to study the wing at a high Reynolds number of $660,000$. The locations of the vortex separation and attachment lines are reported for both low and high Reynolds number. These experimental data sets and the aforementioned high fidelity computations are useful as a benchmark for evaluation of turbulence modeling techniques.

In summary, the dominant physics of the vortical flow over sharp leading edge delta wings has been documented. The vortex flow is very complicated inasmuch as it encompasses the entire spectrum between laminar and turbulent, separated and attached, jet-like and wake-like, and a strong large-scale vortex aligned in the streamwise direction which breaks down into small-scale vortices in all three direc-

tions. The complexity of the flow and the levels of turbulence in the flow increase with increasing angle of attack and Reynolds number.

While sharp leading edge wings and airfoils lend themselves to easier computational analysis, structural and manufacturing considerations dictate a modest yet discernible leading edge radius. When leading edge curvature is introduced on a delta wing, forebody separation becomes significantly more complex to simulate and analyze.

The round leading edge delta wing geometry also appears in many flows in nature. For example, Johansson and Norberg [24] studied how aquatic birds generate propulsion with their delta-wing-like webbed feet. Their results shown in Fig. 1.3a indicate

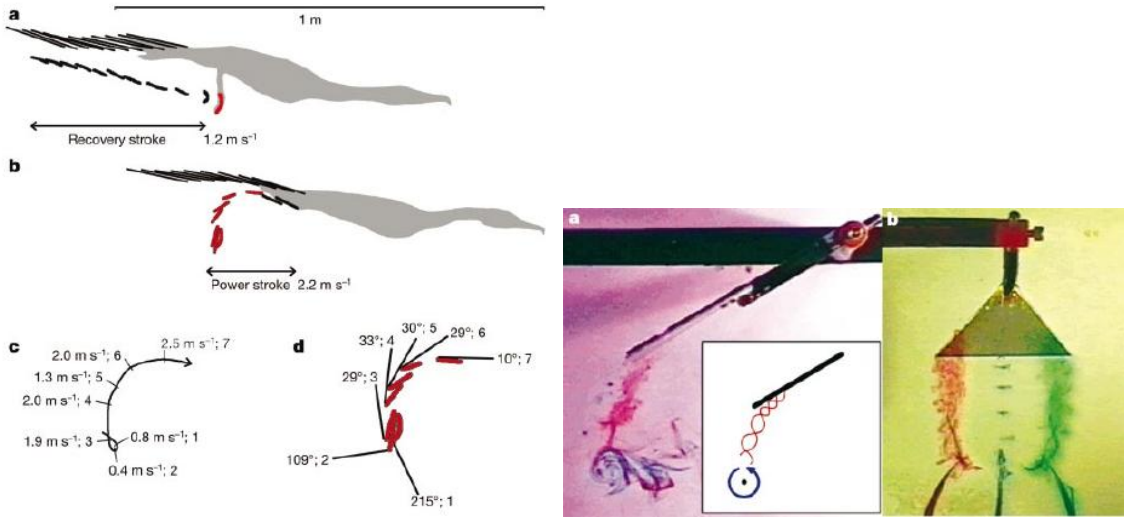

(a) A bird pushing its foot through the power stroke

(b) Vortical flow visualization

Figure 1.3: Visualization of the Vortex Flow Created by a Swimming Bird (Reprinted by permission from Macmillan Publishers Ltd: *Nature, 424(6944):6568* [24] copyright 2003)

that as the bird pushes its feet through the power stroke, the water flows around the foot at an angle of attack well over 100^o and the propulsion is generated from drag. However, after this initial period, the angle of attack decreases to approximately 30^o and the final 60% of the propulsive force is generated from separation-induced vortex lift. Johansson and Norberg [24] also show flow visualization of a semi-slender delta wing with a geometry similar to the webbed foot of the bird. The visualization shown in Fig. 1.3b clearly shows the familiar vortical flow. The vortical flow produced from these swimming birds is more like the vortical flow over the rounded leading edge wings of modern UCAVs than the sharp leading edge flows which have been studied extensively. It is very likely that the flow characteristics show a similar sensitivity to leading edge radius, leading edge sweep, and Reynolds number.

Some of the recent aerospace literature which focuses on the round leading edge delta wing comes from [50] and [42]. The flow physics identified in the literature is now discussed.

For sharp leading edge delta wings, it has been established that the vortex will always separate at the leading edge, beginning at the wing apex. This is not the case for round leading edge delta wings. The separation point is dependent upon many factors including Reynolds number and angle of attack. Hummel [21] provides a schematic in Fig. 1.4 which details the effect that Reynolds number plays in the formation of the primary vortex over slender wings with rounded leading edges. At sufficiently low Reynolds number, there is a region near the wing apex which remains laminar. The flow then undergoes a laminar separation to form the start of the primary vortex. Further aft, the flow transitions to a turbulent flow at the leading edge. Once turbulent, the flow resists immediate separation at the leading edge. There is a small outboard region of turbulent attached flow before the flow undergoes a turbulent separation. At moderate Reynolds number, the region of laminar separation

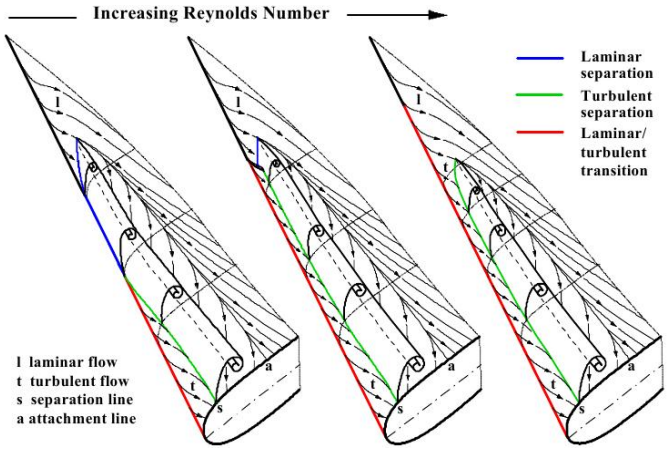

Figure 1.4: Reynolds Number Influence on Round Leading Edge Vortex Formation (Reprinted with permission from: Dietrich Hummel. "Effects of Boundary Layer Formation on the Vortical Flow Above Slender Delta Wings." Number RTO-MP-AVT-111 in RTO AVT Specialists Meeting on Enhancement of NATO Military Flight Vehicle Performance by Management of Interacting Boundary Layer Transition and Separation, Prague, Czech Republic, 2004. [21])

diminishes or is completely eliminated. In this parameter range the separation is almost completely turbulent. Finally at high Reynolds number, the flow completely transitions to turbulence at the leading edge and the primary vortex separation is fully turbulent in nature. Furthermore, as the Reynolds number increases the point of initial separation moves aft on the wing. Clearly the Reynolds number plays a large role in determining the point of separation and type of separation which forms the primary vortex. This dependence is not present in the sharp leading edge wings. In the sharp leading edge case, the primary separation is always fixed at the leading edge and Reynolds number has little effect on the separation. Research by Luckring [32] has investigated the effects of compressibility, Reynolds number, and leading edge radius on delta wings. An increase in Mach number tends to promote separation, while an increase in Reynolds number tends to delay separation. The round

leading edge delta wing creates surface pressure distributions which are wholly unlike those created by sharp leading edge delta wings.

1.4 Dissertation Objectives and Outline

The nonslender, sharp and round leading edge delta wing has received insufficient attention in the literature at the range of α and Re which it is likely to experience in flight. Some of the elementary flow features have been identified. However, the behavior of these flow features at an extensive range of flow parameters has not been established. Such a study is warranted due to the impact that individual vortical flow features have on the aerodynamic performance of the wing. However, identifying a computational method to perform an extensive delta wing study at widely ranging α and Re is complex due to the widely varying scales of motion which may be present. At low Reynolds number, highly resolved DNS simulations are possible. At high Reynolds number, one is restricted to the use of low fidelity RANS modeling. In the intermediate Reynolds number range, hybrid models such as PANS can be employed.

The objective of this dissertation is to apply the PANS model to the high-α delta wing flow at low, moderate, and high Reynolds number at multiple levels of resolution to identify the limits of RANS modeling, explore the challenges of applying the PANS model to the delta wing flow, identify the appropriate resolution required to capture specific flow features, and determine the physical differences between sharp and round leading edge separation.

To achieve this objective, this dissertation is divided into four distinct studies. The specific background and main points of each study are presented in the following sub-sections.

1.4.1 Aerodynamics of Slender Diamond Wings: Reynolds-Averaged Navier Stokes Computations

The round leading edge delta wing geometry is under consideration for use in unmanned combat aircraft. To achieve this, the aerodynamic performance of the delta wing must be well-understood across a wide flight envelope. Computational fluid dynamics (CFD) will play a large role in documenting the flight envelope for modern UCAVs. A NATO (North Atlantic Treaty Organization) aerodynamics study group AVT-183: *Reliable prediction of separated flow onset and progression for air and sea vehicles* has been formed to experimentally and computationally study the semi-slender rounded leading edge diamond wing. The group has established a unit problem geometry for a detailed study.

This study analyzes the Mach number, Reynolds number, and angle of attack effects on the aerodynamic characteristics of the moderately-swept AVT-183 rounded leading edge diamond wing using steady-state RANS modeling techniques. The range of simulated Mach number, Reynolds number, and angle of attack will be determined from the proposed flight conditions of the UCAV application. The objectives of this study are the following:

1. Investigate the role that Reynolds number, Mach number, and angle of attack play on the aerodynamics of the AVT-183 diamond wing.

2. Demonstrate the computational efficiency, but also the weaknesses of RANS for modeling a complex engineering flow with curved surface separation.

3. Identify the limits of steady state RANS modeling, and the areas where high-fidelity models may be able to deliver improved predictions.

1.4.2 Challenges in Variable Resolution Simulations of Separated Flow Over Delta Wings

Variable-resolution simulations of a 50^o swept, sharp leading edge delta wing are performed at low Reynolds number using URANS and PANS turbulence models. The study focuses on the ability of the models to capture the vortex structure both forward and aft of vortex breakdown. The objectives of this study are:

1. Analyze the turbulence levels in the vortex to determine whether they are amenable to PANS modeling.

2. Determine the degree of physical/numerical resolution required to capture different aspects of the delta wing flow features.

3. Identify the main challenges to simulating separated delta wing flows with variable resolution methods.

1.4.3 Variable Resolution Simulations of Sharp Leading Edge Delta Wings at Low and High Reynolds Number

Simulations of nonslender sharp leading edge delta wings are performed using the variable-resolution PANS turbulence model. Flows over a range of Reynolds numbers and angles of attack are simulated. The objectives of this study are

1. Examine the limitations of RANS modeling for sharp leading edge delta wing flow.

2. Determine the delta wing flow features which are able to be captured at vairous levels of turbulence resolution.

3. Explore the limits of PANS modeling at low Reynolds number and the conditions which require a reduction in f_ε.

1.4.4 Variable Resolution Simulations of Round Leading Edge Delta Wings

Simulations of nonslender delta wings with round and sharp leading edges are performed at different scales of resolution using the PANS turbulence model. The delta wing flow features of interest are the intensity of the vortex structure, the levels of turbulence, surface streamline patterns, and surface pressure coefficient. The objectives of this study are:

1. Contrast the aerodynamic performance of round and sharp leading edge delta wings.

2. Establish the key flow feature differences between round and sharp leading edge wing.

3. Identify how the differences in flow features impact the aerodynamic performance of the wings.

2. AERODYNAMICS OF SLENDER DIAMOND WINGS: REYNOLDS AVERAGED NAVIER STOKES COMPUTATIONS

2.1 Introduction

The pursuit of supersonic flight led to the development of wings with large sweep angles, low aspect ratios, and small leading edge radius [33]. These planforms also provide better low-observable characteristics when compared to traditional wing configurations. At high angles of attack, these highly swept wings derive much of their lift from large vortices which are induced from separation at or near the leading edge. The term "slender" is used to define wings which generate a majority of their lift from the separated vortical flow. Slender wings with large sweep angles (greater than 65 degrees), and sharp leading edges have recieved much attention in the literature. Hummel [20] was among the first to formally investigate these complex vortical flows. A typical flow schematic over such a wing is shown in Fig. 1.1. On slender wings with sharp leading edges, the large primary vortex always separates at the wing apex. As the vortices rotate inwards, the flow reattaches on the upper surface and is forced outward towards the wing tip. Here, the flow encounters an adverse pressure gradient due to the presence of the large primary vortex, and may separate forming a secondary vortex.

Recently such diamond wings, but with moderate sweep angles, have become a desirable configuration for Unmanned Combat Aerial Vehicles (UCAVs). The modern UCAV should be a maneuverable vehicle, and should deliver predictable aerodynamic performance at high angles of attack and large roll angles. Modern UCAVs such as the X-47A and X-47B use more of a "semi-slender" wing planform which is characterized by a lower leading edge sweep angle. Both X-47 variants can be seen in Fig.

2.1. The X-47A utilizes a simple semi-slender wing planform with a leading edge sweep of 55^o, while the X-47B utilizes a cranked wing configuration with a leading edge sweep of 54^o and 29^o. The characteristics of the modern UCAV differ from the early slender wings which were studied by Hummel [20] in two main aspects: leading edge sweep and leading edge radius. These semi-slender wing planforms with more moderate leading edge sweep still generate a considerable amount of lift from the separation-induced vortical flow. In addition, realistic wings do have some nominal leading edge radius rather than the sharp leading edge which can significantly alter the aerodynamics of the flow. These configurations have received much less attention in literature than the highly swept slender wing planforms with sharp leading edges.

In order to utilize slender wings on unmanned aircraft, their aerodynamics must be well-understood and documented within a wide flight envelope. Traditional manned aircraft benefit from the presence of a trained pilot handling the controls to avoid placing the vehicle into an aerodynamically unsafe attitude, or to recover from a dangerous condition. An unmanned aircraft will not have this benefit. The limits of the flight envelope must be well-established in order to be programmed into a flight control algorithm. This is particularly challenging due to the fact that during high angle of attack maneuvers slender wings generate the majority of their lift from the separation-induced vortex flow.

Computational fluid dynamics (CFD) will play a large role in documenting the flight envelope for modern UCAVs. A NATO (North Atlantic Treaty Organization) aerodynamics study group AVT-183: *Reliable prediction of separated flow onset and progression for air and sea vehicles* has been formed to examine the aerodynamic characteristics of semi-slender rounded leading edge diamond wings. The group has established a unit problem geometry for a detailed numerical and experimental study. All of the comparisons against experimental data in this paper utilize the AVT-183

force and pressure data [4].

The objective of this paper is to study the Mach number, Reynolds number, and angle of attack effects on the aerodynamic characteristics of the moderately-swept AVT-183 rounded leading edge diamond wing. The range of simulated Mach number, Reynolds number, and angle of attack will be determined from the proposed flight conditions of the UCAV application.

(a) X-47A (b) X-47B

Figure 2.1: Variants of the X-47 UCAV [1]

2.1.1 Brief Literature Survey

There have been several studies performed on sharp leading edge delta wings including very early investigations by Polhamus [41] and Hummel [20]. Studies on rounded leading edge geometries are much smaller in number. Hahn and Drikakis [18] used implicit Large Eddy Simulation (LES) to study a rounded leading edge delta wing with a leading edge sweep of 40 degrees. They conclude that standard RANS methods may be inadequate at predicting the separation and subsequent vortical

flow. Huang et. al. [52] present CFD and experimental results for a variety of delta wings with various leading edge sweeps and leading edge radii. More recently, rounded leading edge slender wings have received attention from Luckring [32] and the 2nd Vortex Flow Experiment (VFE-2) [22]. In this paper we demonstrate that RANS calculations provide an adequately accurate desription of the aerodynamic characteristics of diamond wing flows.

2.1.2 Paper Outline

In Section 2.2, the RANS equations and the computational details are presented. The swept wing configuration and grid details are also given. Also, three Mach and Reynolds number combinations that correspond to take-off, cruise, and combat are identified to characterize the different flight operating conditions. The simulations are performed at various angles of attack at these conditions. The results are then presented in Section 2.3. First, a qualitative examination of the vortex structure is performed at different angles of attack and Reynolds numbers. Next, lift, drag, and surface pressure coefficients at take-off conditions obtained from the simulations are compared against experimental data at different angles of attack. Once the validity of the computational approach is established, simulation results are presented for cruise and combat Reynolds and Mach number combinations. Section 2.4 concludes the paper with a brief discussion.

2.2 Governing Equations and Simulation Features

In this section we first present the RANS governing equations. Then a brief description of the CFD code VULCAN is given. Finally, the flow geometry and parameters are described.

2.2.1 RANS Equations

The results presented in this paper are generated from CFD simulations which solve the Favre Avgeraged Navier-Stokes (RANS) equations. The 1998 Wilcox $k-\omega$ turbulence model is used to close the Reynolds stress term in the mean flow equations. The mean flow equations for mass, momentum, and energy are written in nonorthogonal curvilinear form. However, for the sake of brevity and clarity, we will present the familiar orthogonal cartesian mean flow equations. A more complete description of the governing equations can be found in [23].

The mean flow equations are:

$$\frac{\partial \overline{\rho}}{\partial t} + \frac{\partial}{\partial x_j}\left(\overline{\rho}\widetilde{u}_j\right) = 0 \tag{2.1}$$

$$\frac{\partial}{\partial t}\left(\overline{\rho}\widetilde{u}_i\right) + \frac{\partial}{\partial x_j}\left[\overline{\rho}\widetilde{u}_i\widetilde{u}_j + \delta_{ij}\overline{p} - \overline{\tau_{ij}} + \overline{\rho}\widetilde{u_i'u_j'}\right] = 0 \tag{2.2}$$

$$\frac{\partial}{\partial t}\left(\overline{\rho}\widetilde{E}\right) + \frac{\partial}{\partial x_j}\left[\overline{\rho}\widetilde{H}\widetilde{u}_j - \widetilde{u}_i\overline{\tau}_{ji} + \overline{q}_j - D_{\tilde{k}j}\right] = 0 \tag{2.3}$$

with

$$\overline{\tau}_{ij} = \mu\left(\frac{\partial \widetilde{u}_i}{\partial x_j} + \frac{\partial \widetilde{u}_j}{\partial x_i} - \frac{2}{3}\frac{\partial \widetilde{u}_k}{\partial x_k}\delta_{ij}\right) \tag{2.4}$$

$$\overline{q}_i = -\left(\lambda + \frac{\mu_t}{Pr_t}\right)\frac{\partial \widetilde{T}}{\partial x_j} \tag{2.5}$$

$$D_{\tilde{k}j} = \left(\frac{\mu}{Pr_l} + \frac{\mu_t}{Pr_t}\right)\frac{\partial \widetilde{k}}{\partial x_j} \tag{2.6}$$

$$\overline{p} = \overline{\rho}R\widetilde{T} \tag{2.7}$$

$$\widetilde{h} = \left(\frac{\gamma R}{\gamma - 1}\right)\widetilde{T} \tag{2.8}$$

$$\widetilde{H} = \widetilde{h} + \frac{1}{2}\left(\widetilde{u}^2 + \widetilde{v}^2 + \widetilde{w}^2\right) + \widetilde{k} \tag{2.9}$$

$$\widetilde{E} = \widetilde{H} - \frac{\overline{p}}{\overline{\rho}} \tag{2.10}$$

The Reynolds stress term is modeled by the Boussinesq approximation where:

$$-\overline{\rho}\widetilde{u_i'u_j'} = \mu_t \left[\left(\frac{\partial \widetilde{u}_i}{\partial x_j} + \frac{\partial \widetilde{u}_j}{\partial x_i} \right) - \frac{2}{3}\frac{\partial \widetilde{u}_k}{dx_k}\delta_{ij} \right] - \frac{2}{3}\overline{\rho}\widetilde{k}\delta_{ij} \tag{2.11}$$

$$\mu_t = \rho\frac{\tilde{k}}{\tilde{\omega}} \tag{2.12}$$

The turbulence closure equations of the $k-\omega$ turbulence model used in these simulations are:

$$\frac{d\overline{\rho}\tilde{k}}{dt} = \mu_t S^2 - \rho C_\mu \tilde{k}\tilde{\omega} - \overline{\rho}\tilde{k}\frac{\partial \tilde{u}_i}{\partial x_i} + \frac{\partial}{\partial x_i}\left[(\mu + \sigma_k \mu_t)\frac{\partial \tilde{k}}{\partial x_i} \right] \tag{2.13}$$

$$\frac{d\overline{\rho}\tilde{\omega}}{dt} = \alpha\frac{\tilde{\omega}}{\tilde{k}}\mu_t S^2 - \rho\beta\tilde{\omega}^2 - \overline{\rho}\tilde{\omega}\frac{\partial \tilde{u}_i}{\partial x_i} + \frac{\partial}{\partial x_i}\left[(\mu + \sigma_\omega \mu_t)\frac{\partial \tilde{\omega}}{\partial x_i} \right] \tag{2.14}$$

2.2.2 Simulation Details

The simulations are performed with the code VULCAN (Viscous Upwind aLgorithm for Complex flow ANalysis). It was developed and is maintained by researchers at NASA Langley in Hampton, VA. It is a finite volume, turbulent, non-equilibrium, finite-rate chemical kinetics, Navier-Stokes flow solver for structured, cell-centered, multi-block grids. The code is parallelized using MPI, and the majority of the simulations for this work were performed using 256 processors. The present simulations utilized the Roe upwind scheme and 4th order WENO interpolation with the Wilcox 1998 $k-\omega$ turbulence model. It must be pointed out that VULCAN has many other options available for numerical analysis. The turbulence production-to-dissipation ratio limiter in the code was disabled, and the solution was integrated to the wall without the use of any wall functions. The turbulence closure coefficient values used

in these simulations are reported in Table 2.1.

Table 2.1: Turbulence closure coefficients

C_μ	α	β	σ_k	σ_ω
0.09	0.52	0.072	0.5	0.5

2.2.2.1 Flow Geometry and Grid

The geometry of the AVT-183 diamond wing and the grid which was developed for this test case are shown in Fig. 2.2. The leading edge sweep is 53^o which would place this wing in the "semi-slender" category which has not been studied much in literature. The airfoil is the NACA64A006 which is a cambered 6% thick arifoil. The grid is a structured 56-block grid with $3,027,456$ total cells. The grid boundaries extend 5 chord lengths forward of the wing apex, aft of the trailing edge, above the mean chord line, below the mean chord line, and outboard of the wing tip.

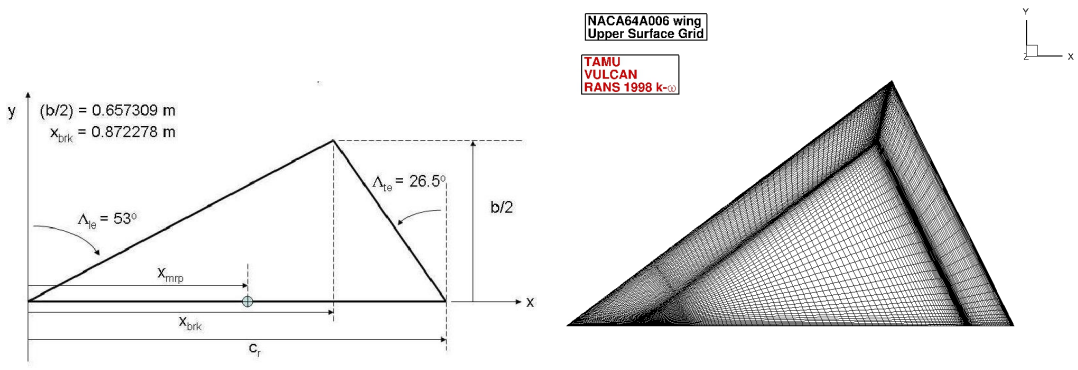

(a) Diamond wing planform (not to scale) [34] (b) Diamond wing half-span grid

Figure 2.2: AVT-183 Diamond Wing Geometry

2.2.2.2 Flow Parameters: Take-off, Cruise, and Combat

In order to simulate conditions which are relevant to UCAV application, this section will attempt to identify the range of Reynolds number, Mach number, and angle of attack typical of flight conditions. The AVT-183 geometry used in this study very closely resembles the geometry of the X-47A UCAV, and some important characteristics of the X-47A are listed here:

Table 2.2: X47A specifications

Wingspan	Chord	Ceiling	Cruise Mach No.	Max. TOW	Planform Area
8.4 m	12 m	40,000 $ft.$	0.45	5,500 $lb.$	50 m^2

2.2.2.3 Test Matrix

Based on these flight conditions, we develop an approximate range of Reynolds numbers and angles of attack that the X-47A will likely experience in flight. The range of Reynolds numbers depends on the altitude, Mach number, and length (mean aerodynamic chord) of the UCAV at any given stage of flight. This study will focus on three separate flight conditions: take-off, cruise maneuvers, and combat maneuvers. At each flight condition, the atmospheric parameters are derived from the standard atmosphere tables in [25], the freestream velocity is derived from the Mach number, and the Reynolds number is determined from the freestream velocity and viscosity. Our objective is to simulate a range of angle of attack - $\alpha = 0^o - 23^o$ - for each flight condition. The Reynolds numbers based on a mean aerodynamic chord of 8 meters for the conditions of take-off, cruise, and combat for the full scale X47A vehicle are 27.95M, 23.58M, and 49.15M respectively. In order to reduce the computational

burden, our simulations will be performed for Reynolds numbers consistent with the mean aerodynamic chord of the experimental model of 0.8 meters, which is one order of magnitude lower than the full scale mean aerodynamic chord. Using these conditions, we develop the test matrix shown in Table 2.3. The take-off condition is nearly identical to the experimental conditions from the AVT-183 working group shown in Table 2.4 .

Table 2.3: Flight conditions test matrix

Condition	Altitude	Mach Number	Unit Reynolds Number [1/m]
Take-off	Sea Level	0.15	3.494M
Cruise	40,000 ft.	0.45	2.947M
Maneuver	10,000 ft.	0.35	6.144M

2.2.2.4 Take-off

The take-off flight condition will simulate what the UCAV will experience during a sea-level takeoff. Modern UCAVs are being developed to take off from aircraft carriers so the condition will be at sea level standard atmospheric conditions.

2.2.2.5 Ceiling Cruise

This will simulate a situation where the UCAV is at its cruise conditions and must abruptly change its angle of attack and roll angle. For this condition we will assume that the aircraft is cruising at an altitude which is near its service ceiling, and its listed cruise Mach number.

2.2.2.6 Combat Maneuver

We will attempt to reproduce a situation where the UCAV is at a lower altitude to engage in combat situation maneuvers. The goal of this research is to test the

limits of the flight envelope so a relatively high Mach number is used in order to achieve a large Reynolds number.

2.3 Results

We now present results from RANS simulations of the AVT-183 diamond wing at various angles of attack, Reynolds numbers, and Mach numbers which are representative of the three flight conditions described in the previos section.

2.3.1 Qualitative Flow Features

We first compare the computed results qualitatively against the benchmark experimental data. Luckring [32] established the effects of Reynolds number, Mach number, and leading-edge bluntness on the aerodynamics on a 65 degree leading edge sweep delta wing. This section will demonstrate the same trends for the AVT-183 delta wing which has a rounded leading edge and 53 degree leading edge sweep.

Figure 2.3 shows the effects of varying the angle of attack. In the figure, contours of pressure coefficient are shown for the upper surface of the wing, and the flow is from left to right. The bottom horizontal edges shown in Fig. 2.3 represent the symmetry plane of the wing. The presence of the separated vortex is visualized as the large streak of negative pressure, the deep red color which emanates from the leading edge of the wing. In Fig. 2.3a which is at $\alpha = 10^o$, the upper surface suction is relatively weak, and the streak of pressure suction is narrow. As the angle of attack increases to $\alpha = 12^o$ as shown in Fig. 2.3b, the magnitude of the pressure suction increases as shown by the darker red contour, the streak emanates from a point further forward on the wing indicating that the primary vortex has separated earlier, and the streak is wider. This trend continues as the angle of attack is further increased to $\alpha = 14^o$ and $\alpha = 16^o$ in Fig. 2.3c and Fig. 2.3d respectively. The magnitude of the suction increases further as shown by the even deeper red contour, the point of primary

vortex separation continues to move forward on the wing, and the vortex continues to widen. These results establish the qualitative trend that the point of primary vortex separation moves forward and the strength of the suction in the vortex region increases for increasing angle of attack. Figure 2.4 shows the effects of varying the

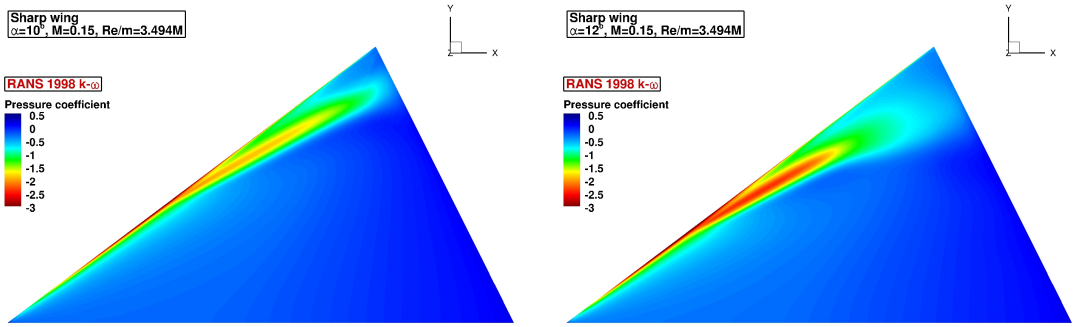

(a) $\alpha = 10^o$

(b) $\alpha = 12^o$

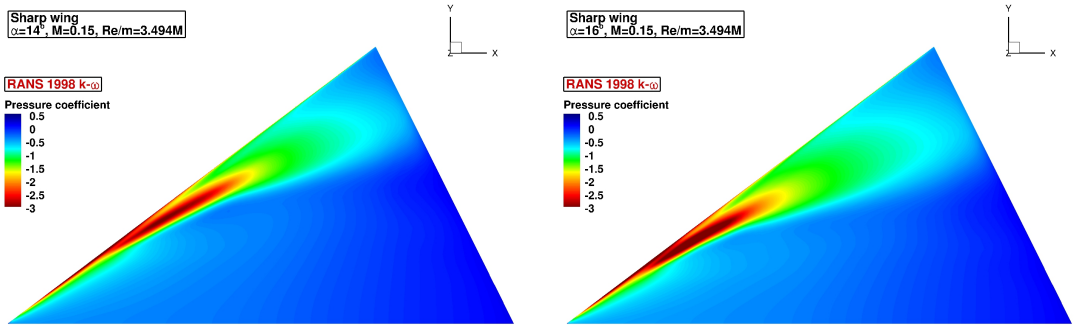

(c) $\alpha = 14^o$

(d) $\alpha = 16^o$

Figure 2.3: Contours of Surface C_p with Varying α; Re/m=3.494M, M=0.15

Reynolds number. Contours of the upper surface pressure coefficient are shown in Fig. 2.4a and Fig. 2.4b for $Re/m = 2.947M$ and $Re = 6.144M$ respectively. There

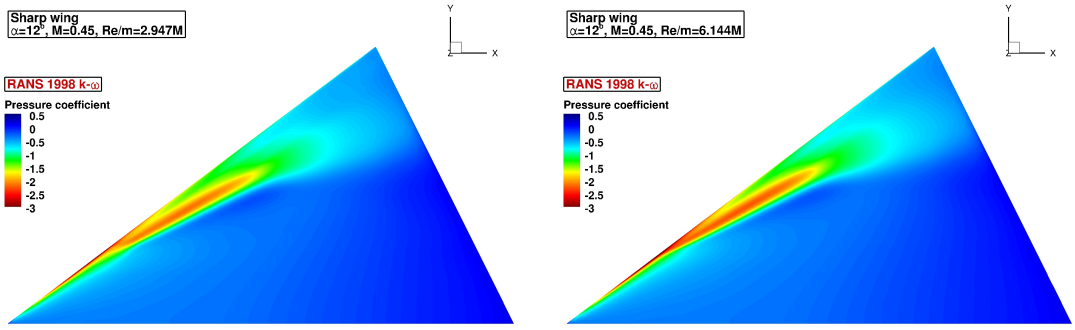

(a) $Re/m = 2.947M$ (b) $Re/m = 6.144M$

Figure 2.4: Contours of Surface C_p with Varying Re; $\alpha = 12^o$, M=0.45

are only small differences between the two figures indicating that Reynolds number plays a more subtle role in the formation of the primary vortex. However, increasing the Reynolds number strengthens the magnitude of the suction in the vortex as seen by the deeper red contours visible in Fig. 2.4b, and the point of primary vortex separation is slightly more aft for the higher Reynolds number case. The higher Reynolds number enables the flow to resist separation longer due to the increased boundary layer turbulence levels. These results establish the qualitative trend that the point of primary vortex separation moves aft and the strength of the suction in the vortex region increases for increasing Reynolds number.

These qualitative comparisons are consistent with the results presented in [32] which are shown in Fig. 2.5. The results indicate the location of the first point of primary vortex separation for three different leading edge radii. For our comparison, we will focus on the medium case. For example, in the Re = 6M case, the point of separation for the medium leading edge case at $\alpha = 14^o$ is at $x_v/c_r = 0.3$. In the Re = 60M case, the point of separation for the medium leading edge case at $\alpha = 14^o$

moves aft to $x_v/c_r = 0.5$. The results clearly demonstrate the qulaitative trend that increasing the Reynolds number *delays* separation. It is also clear that for both the low and high Reynolds number cases that increasing α *promotes* separation. The results from our simulations in Figs. 2.3 and 2.4 match this qualitative trend. The

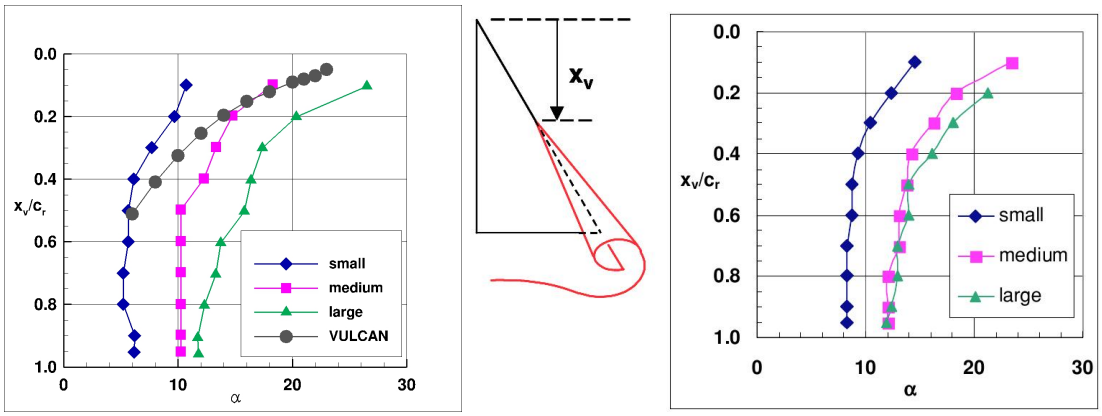

(a) $Re = 6M$ (b) $Re = 60M$

Figure 2.5: Effect of α and Re on Vortex Separation from Luckring [32]

locations of the primary vortex separation for our simulations at combat conditions (Re/m=6.144M and M=0.35) are also plotted on Fig. 2.5a. The data closely follow the results from Luckring's medium leading edge radius case for high angles of attack, and the trend of the separation point moving forward with increasing α is captured. However, for low and moderate angles of attack the results diverge. This can be attributed to the discrepancies between the geometries used in each case. Our simulations use a diamond geometry shown in Fig. 2.2 while Luckring uses a true delta wing geometry shown in the middle of Fig. 2.5.

2.3.2 Validation under Take-off Conditions

The RANS results obtained with VULCAN are validated against the experimental data from the AVT-183 campaign. The VULCAN simulation conditions are very similar to the experimental test conditions. The simulation parameters are outlined in Table 2.4 The experimental data consists of surface C_p plots at angles of attack

Table 2.4: AVT-183 validation conditions

Airfoil	α	Unit Reynolds No.	Mach No.
NACA64A006	$-2^o \rightarrow 20^o$	3.375M	0.15

ranging from -2^o through 20^o. The experimental data included one case where the flow was allowed to transition to turbulence freely and several other cases where the turbulence was forced with trips ranging in size from $110\mu m$ to $550\mu m$. The AVT-183 study group recommends that the $110\mu m$ trip data should be used for comparisons against CFD. All experimental data comparisons made in this paper use this data set. These results can be found in Figs. 2.6 and 2.7. Each sub-figure in Fig. 2.6 and 2.7 shows the surface pressure coefficient at a particular section along the chord of the wing. The specific locations are $x/c_r = 0.1, 0.2, 0.295, 0.305, 0.395, 0.405, 0.5,$ and 0.6. In each pane of Fig. 2.6 and 2.7 there is a suction peak visible at the tip of the wing. This suction peak is due to the curvature of the leading edge causing the flow to be accelerated around from the lower to the upper surface. The primary vortex is visible as another suction peak inboard from the wing tip. The wing tip suction peak and the primary vortex suction peak are highlighted by arrows in Fig. 2.7a. Overall, the sectional pressure coefficients shown in Figs. 2.6 and 2.7 match the experimental data well, except for areas very near the first point of separation,

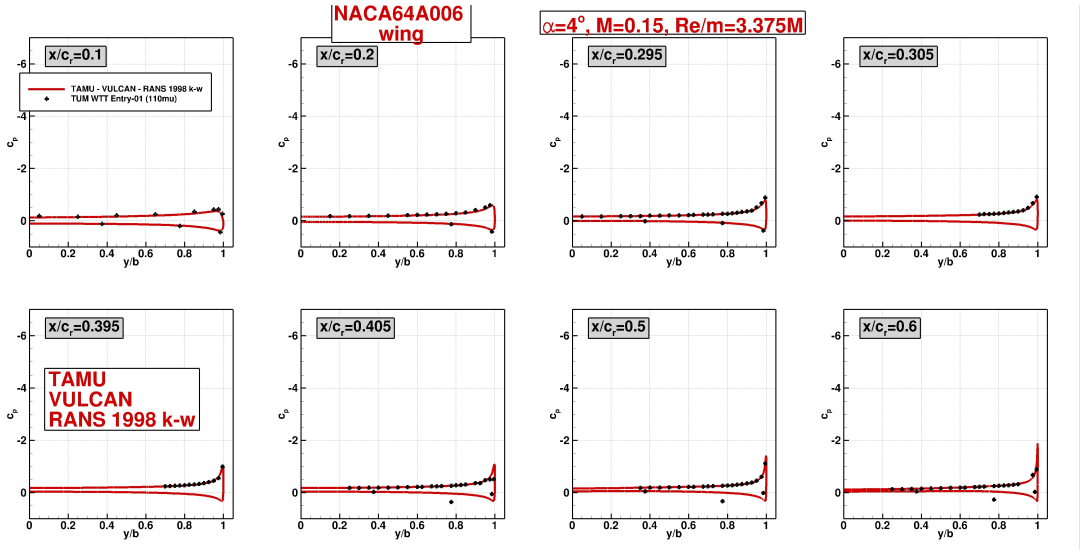

(a) Sectional C_p: $\alpha = 4^o$

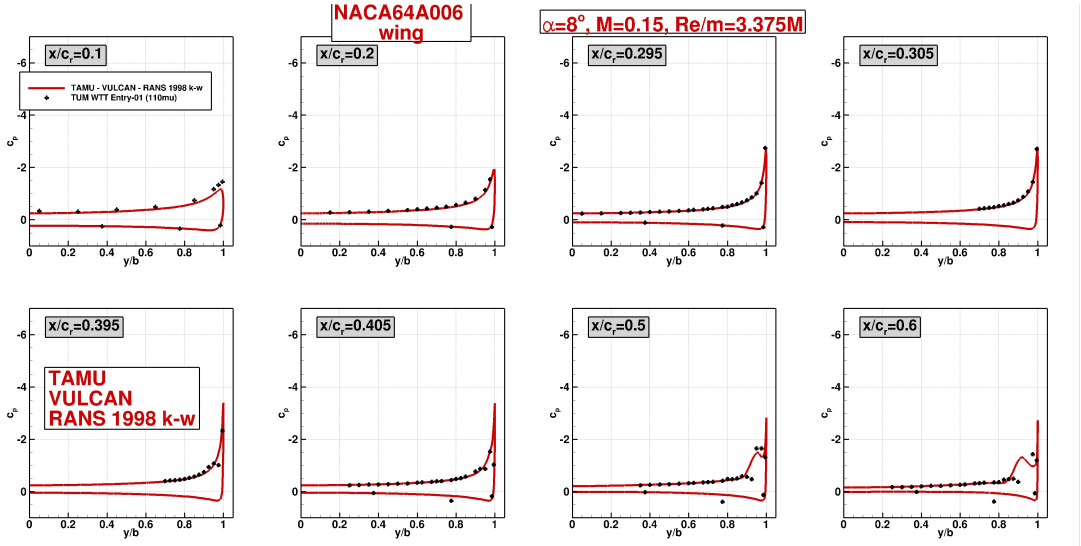

(b) Sectional C_p: $\alpha = 8^o$

Figure 2.6: Sectional C_p Compared Against AVT-183 Experimental Data: $110\mu m$ Turbulence Trip, $\alpha = 4^o$, 8^o

for example see Fig 2.7a at $x/c_r = 0.295, 0.305, 0.395$ and 0.405.

In Fig. 2.6a the vortex has not yet begun to form and the simulations match the data exactly. In Fig. 2.6b we see the first signs of primary vortex formation

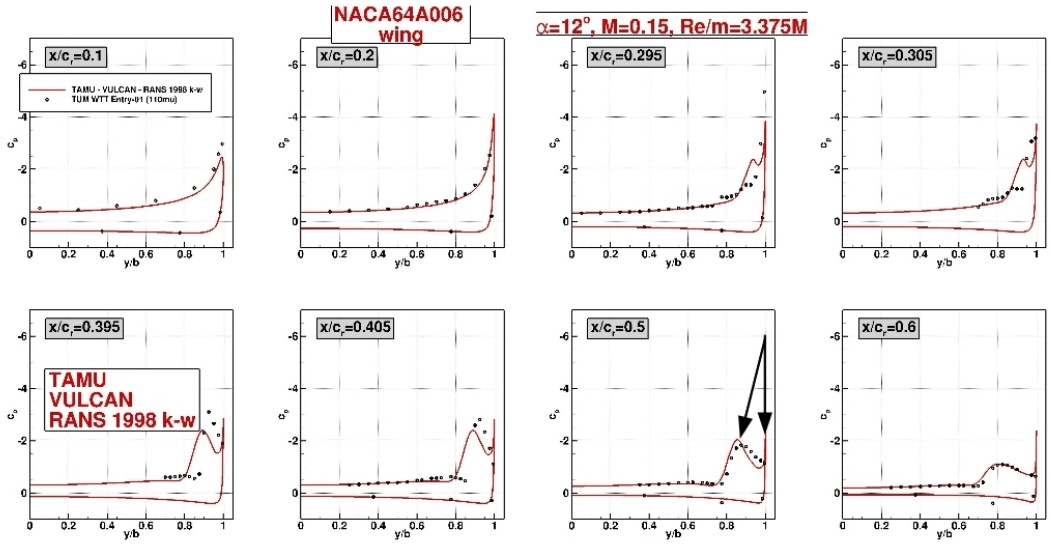

(a) Sectional C_p: $\alpha = 12^o$

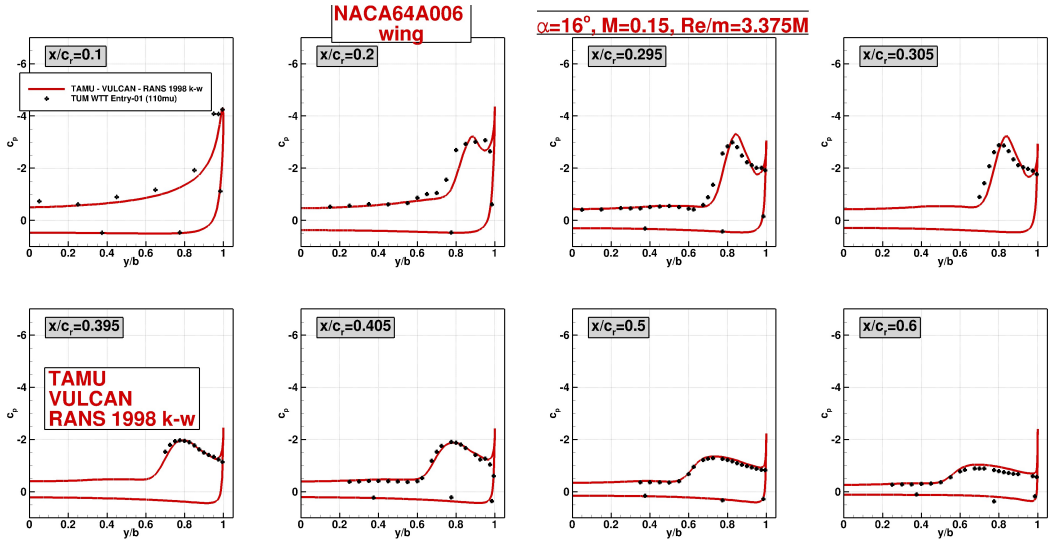

(b) Sectional C_p: $\alpha = 16^o$

Figure 2.7: Sectional C_p Compared Against AVT-183 Experimental Data: $110\mu m$ Turbulence Trip; $\alpha = 12^o$, 16^o

at $x/c_r = 0.5$. Next, in Fig. 2.7a, the simulations predict the formation of the vortex by $x/c_r = 0.295$ while the experimental data does not show vortex formation until $x/c_r = 0.395$. It must be noted that the tripping used in the experiments also affects the precise location of vortex separation. Since the present calculations are fully turbulent, we can only expect approximate agreement. This highlights the difficulty in predicting the onset of vortex formation for rounded leading edge delta wings which has been noted in literature. Apart from this area of initial vortex formation near 30% and 40% chord, the agreement is excellent. Finally, in Fig. 2.7b the vortex is formed by $x/c_r = 0.2$ and the agreement between the simulation and the experiment is good. The simulations were performed for angles of attack ranging from -2^o up through 20^o, but only 4 angles of attack are shown in Figs. 2.6 and 2.7 for the sake of brevity; the other angles of attack show trends similar to the ones presented.

In addition to the sectional pressure coefficient, we also compare C_L and C_D, for the AVT-183 validation case in Fig. 2.8. The theory of thin wings [2] has established that the lift coefficient varies linearly with angle of attack until regions of flow separation form on the suction side of the wing and stall is approached causing the lift curve to inflect downward and eventually peak. However, early research on delta wings by Polhamus [41] describe the benefits of separated vortical flow on the suction side of the wing which increases the lift coefficient above the line predicted by thin wing theory. This incremental increase in lift due to the separated vortical flow over the delta wing is called vortex lift. Our results in Fig. 2.8 show linear growth in C_L with increasing α until approximately $\alpha = 5^o$ at which point the lift begins to gradually increase above the linear reference. This is precisely the angle of attack where the primary vortex begins to form, thus this increase in lift can be attributed to vortex lift. Overall, the lift coefficient is well predicted by the

simulations. Further, the near quadratic growth of C_D observed in experiments is also well replicated by the model calculations. With the completion of VULCAN

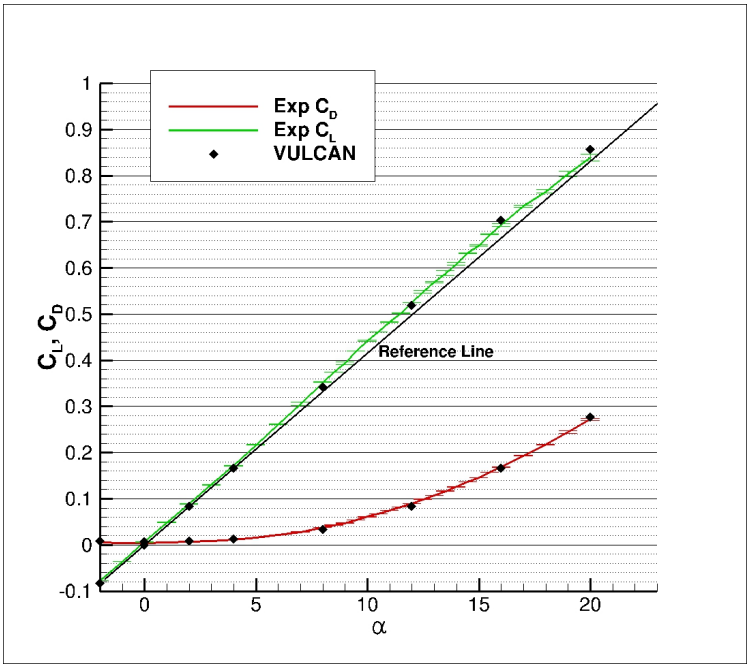

Figure 2.8: C_L and C_D from RANS Simulations Compared to Experimental Data for Validation Conditions

validation in take-off conditions, we proceed to compute aerodynamic characteristics at ceiling cruise and combat conditions.

2.3.3 Aerodynamics Characteristics at Cruise and Combat Parameters

The coefficients of lift and drag for the test matrix of Table 2.3 are shown in Fig. 2.9. The experimental data from the validation case is shown for reference in each figure. The takeoff condition results in Fig. 2.9a agree very well with the experimental data. This is the only case for which we would expect perfect agreement because the takeoff conditions are nearly identical to the experimental conditions which are

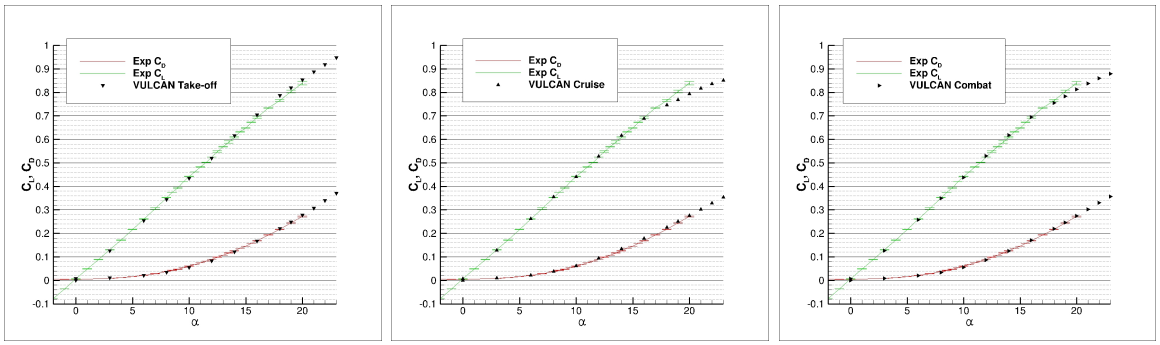

(a) take-off (b) cruise (c) combat

Figure 2.9: C_L and C_D for Each Flight Condition Compared to Experimental Data Under Takeoff Conditions

used for validation. The only discrepancy between the takeoff results compared to the experimental data is a slight overprediction of lift at angles of attack greater than 15^o. The drag coefficient is well predicted by the takeoff simulations. The results for the cruise and combat conditions shown in Fig. 2.9b and Fig. 2.9c differ slightly from the validation experimental data. At cruise conditions, the simulations predict that the lift coefficient departs from the take-off experimental data at $\alpha = 18^o$ and saturates rapidly. The results at combat comditions also show a similar departure from the take-off conditions at $\alpha = 18^o$, but in a more gradual manner. The drag coefficients for the cruise and combat conditions are nearly identical throughout the entire range of α, while the drag coefficient for the takeoff conditions is slightly higher than the other two cases due to the greater induced drag from the higher values of lift coefficient. None of the three cases show evidence of stall by $\alpha = 23^o$. However, the relative drop-off in the lift coefficients in the cruise case does seem to indicate that stall is immenent. The precipitous increase in drag coefficients at the higher angles of attack is also an indication of impending stall.

To obtain a better understanding of impending stall, Fig. 2.10 shows the pressure coefficient contours on the surface at $\alpha = 23^o$. The location of primary vortex

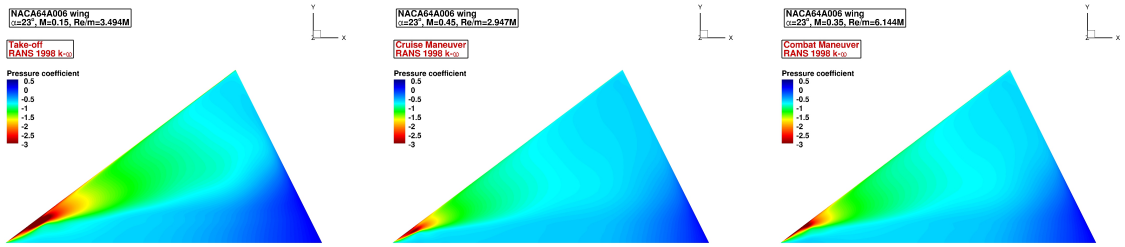

(a) take-off (b) cruise (c) combat

Figure 2.10: Surface C_p at $\alpha = 23^o$

separation is located at the intersection of the deep red contours and the leading edge. This location is very near the apex of the wing for all three cases. For the takeoff case in Fig. 2.10a, the primary vortex is maintained for a short distance near the apex of the wing before it breaks down and washes out into a large area of slightly negative pressure. This is in direct contrast to the cruise and combat cases shown in Fig. 2.10b and Fig. 2.10c where the primary vortex breaks down almost immediately after it has formed and the region aft of the breakdown has less upper surface suction than the takeoff case. Studying the surface pressure coefficient at this high angle of attack yields some insight into the manner in which the wing approaches stall faster at cruise conditions faster than it does at takeoff conditions. It is clear the the primary vortex breaks down much quicker in the cruise case which greatly reduces the lift on the upper surface of the wing, especially the vortex lift which was discussed in the previous section.

For further insight, the surface streamlines and pressure coefficient field at $\alpha = 14^o$

are shown in Fig. 2.11. This angle of attack was chosen for closer examination because the primary vortex is well defined. The important features of the flow which can be visualized from the streamlines are labeled in Fig. 2.11a and the inset in Fig. 2.11b, corresponding to the takeoff conditions. The surface streamlines for the cruise and combat conditions are presented in Fig. 2.11c and Fig. 2.11d respectively. The underlying contours are of surface pressure coefficient, but the color scheme which is chosen here differs from previous surface C_p plots to enhance the visualization of the streamlines. There are many interesting observations which can be made by comparing and contrasting the visualizations in Fig. 2.11. First, the pressure coefficient contours for the cruise and combat conditions in Fig. 2.11c and Fig. 2.11d are noticeably different. The location of primary vortex separation is further aft in the combat case, and the suction from the primary vortex is much stronger in the combat case. Despite these obvious differences between the surface pressure coefficient contours in Fig. 2.11c and Fig. 2.11d, the lift coefficients at this angle of attack (14^o) are practically identical in Fig. 2.9b and Fig. 2.9c.

Next we turn our attention to studying the streamline patterns which can be seen in Fig. 2.11. Near the apex of the wing there is a region of attached flow in all three cases. These streamlines begin on the lower surface of the wing and travel around the rounded leading edge of the wing, remaining attached to the upper surface thereafter. Inspecting Figs. 2.11a, 2.11c, and 2.11d reveals that the length of the attached flow region along the leading edge (X_{attach}) inreases with increasing Reynolds number. This is consistent with aerodynamic theory [25] that the flow is able to resist separation from the adverse pressure gradient experienced while traveling around the leading edge at higher Reynolds number.

After this region of attached flow, the primary vortex forms as the flow is no longer able to remain attached while it traverses around the leading edge. The

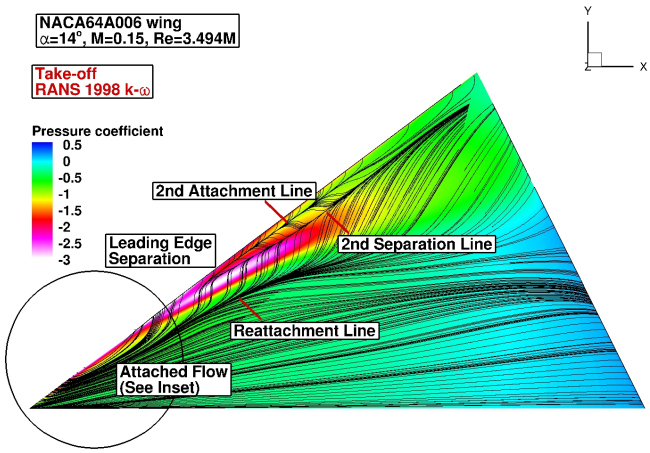

(a) take-off

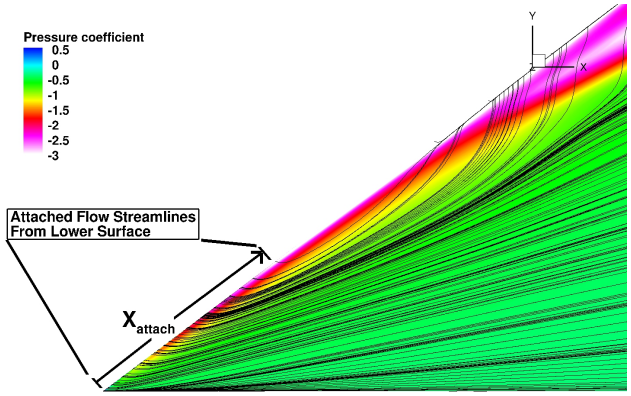

(b) take-off inset

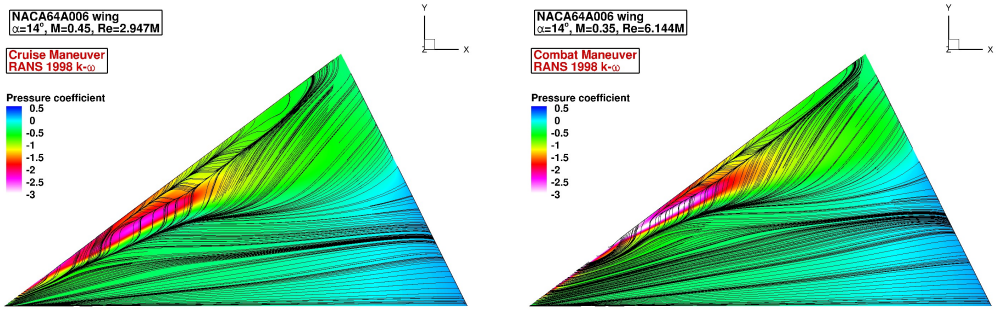

(c) cruise

(d) combat

Figure 2.11: Surface Streamlines and C_p at $\alpha = 14^o$

primary vortex rolls upwards, then inwards towards the wing centerline, and finally downwards towards the surface of the wing where the flow reattaches to the upper surface. This reattachment line is marked on Fig. 2.11a. Once reattached, the flow is pulled outboard by the strong suction in the vortex core. However, once the streamlines traverse the centerline of the vortex, an adverse pressure gradient is encountered. This rapid increase in pressure causes a second vortex to separate from the upper surface underneath the primary vortex. This secondary vortex is much smaller than the primary vortex and rolls upwards, outwards towards the leading edge of the wing, and finally downwards where it reattaches to the upper surface. These secondary separation and reattachment lines are marked on Fig. 2.11a.

There are other interesting flow features which can be gleaned from understanding these streamline patterns. First we compare the reattachment lines for the cruise and combat cases in Fig. 2.11c and Fig. 2.11d. The reattachment line for the combat case is much closer to the vortex core than the reattachment line for the cruise case. This is an indication of a more tightly wound primary vortex for the combat case, with a smaller vortex radius than the cruise case. The surface pressure coefficient contour beneath the primary vortex in the combat case in Fig. 2.11d also shows a greater magnitude of suction which would confirm a tighter, more intense primary vortex.

2.4 Conclusions

This paper investigates the aerodynamic characteristics of rounded leading edge delta wings which are good candidates for use on modern UCAVs. RANS simulations of the delta wings at different flight conditions have been performed. Coefficients of pressure, lift, and drag have been investigated along with surface streamline visualization. The qualitative aerodynamic trends establised in literature have been

confirmed. Recent experimental data from the AVT-183 campaign has been reproduced quite accurately. The flight envelope including take-off, ceiling cruise, and combat maneuver conditions have been examined. Vastly different flow fields and pressure distributions can sometimes yield the same integrated quantities of lift and drag coefficient.

In order to more completely characterize the flight envelope of the UCAV, it would be useful for future studies to simulate the full-span delta wing and include simulations at various roll angles while at a high angle of attack. Due to the complex nature of the separated vortical flow at high angle of attack, one wing may stall prematurely while also in a roll maneuver which should be documented before implementation on a UCAV. These investigations will be undertaken in future works with high fidelity models.

3. CHALLENGES IN VARIABLE RESOLUTION SIMULATIONS OF SEPARATED FLOW OVER DELTA WINGS

3.1 Introduction

Future unmanned combat aerial vehicles (UCAVs) will employ delta wing geometries due to their ability to maintain their stability, control, and lift at high incidence angles. Delta wing aerodynamics at large angles of attack is characterized by large vortices which separate from the leading edge of the wing creating a complex separated flow field. There have been numerous computational and experimental studies performed on delta wings with various leading edge sweep angles and leading edge curvature, [20], [29], [46], [32].

The delta wings which are currently being proposed for use in UCAVs such as the Northrop Grumman X-47A will have moderate leading edge sweep angles ($45^o - 60^o$). A comprehensive high-fidelity delta wing data set was generated by the direct numerical simulation (DNS) study of Gordnier and Visbal [13]. Their DNS computes a sharp leading edge delta wing with 50^o sweep angle at $Re = 26,000$ at 5^o, 10^o, and 15^o angle of attack using a 6th order compact differencing scheme, with an 8th order low pass spatial filter. Although the Reynolds number for their study is significantly lower than the Reynolds numbers expected for flight, these simulations are useful for understanding fundamental flow physics of delta wings and provide an important low Reynolds number benchmark for validating computational tools. The preceeding section investigated round leading edge delta wings and determined that vortical flow regions dominated by complex flow physics, such as the onset of primary vortex separation and progression towards breakdown, require increased numerical fidelity.

The principal objective of this study is to determine the degree of physical/numerical resolution required to capture different aspects of the delta wing flow features. In this study we will employ URANS and PANS to compute the low Reynolds number case of Gordnier and Visbal [13]. The main challenges to simulating delta wing separated flows will be identified.

3.2 PANS Closure Modeling

The results for this study are obtained using the PANS turbulence closure model. PANS is a variable resolution model where the filter control parameters f_k and f_ε determine the resolution of the simulation. The user can achieve accuracy-on-demand by varying the filter control parameter from a coarse RANS simulation to a fully-resolved DNS simulation depending upon the grid size: $f_k \geq 3\left(\Delta/\Lambda\right)^{(2/3)}$ [12] where $\Lambda = k^{(3/2)}/\varepsilon$. The PANS model is uniquely suited to simulate the separated delta wing flow which is comprised of regions which require high fidelity resolution, along with regions where a low fidelity model may be applied. The details of the original derivation of the PANS model can be found in [10], and in the Introduction.

3.3 Simulation and Results

This section presents results for the 50^o leading edge sweep, flat plate delta wing of [13] simulated at $\alpha = 15^o$ with URANS and PANS turbulence models. Comparisons are made against DNS data when possible. In the first subsection, we briefly identify various vortical flow features which should be found in our simulations. In the second subsection, we compute the delta wing flow by performing simulations on the fine DNS grid at flow conditions ($Re = 26,000$) identical to the DNS study. The third subsection provides URANS and PANS results at the same flow conditions using a significantly coarsened grid to determine whether the important flow features can be computed at lower resolutions.

3.3.1 Flow Features and Challenges

According to [13], there are several flow features which one would expect to encounter when simulating such a case. At $\alpha = 15^o$, there should be a distinct primary and secondary vortex, and a subtle tertiary vortex present in the pre-breakdown region. Instabilities should be present in the separated shear layer and within the primary vortex by $x/c = 0.3$. Vortex breakdown should occur in the range of $x/c = 0.40 - 0.54$. After breakdown, the dominant primary and secondary vortices are disintegrated into fine scale structures with no semblance of a dominant vortex.

The flow is nearly laminar before vortex breakdown. However, the laminar vortex is complex featuring steep gradients and separation. The shear layer in this region harbors the instabilities that lead to vortex breakdown and ultimately turbulence. Thus, despite being laminar, the forward vortex region needs high numerical resolution. After vortex breakdown, turbulence develops rapidly in the aft half of the wing. These complex flow features present several challenges to hybrid computations.

To understand the importance of high fidelity computations of the laminar region we perform two sets of hybrid simulations. The first set employs the high resolution DNS grid ensuring accurate simulations of the laminar region. The second set uses a coarse grid in the laminar region and beyond. Contrasting the results can lead to a clearer understanding of the resolution needs of this complex flow.

3.3.2 Comparison of Scheme Order-of-Accuracy

This subsection provides a direct comparison of a 3rd-order upwind and a 4th-order WENO scheme in order to asses the effects of the scheme order-of-accuracy on the simulations. It is clear from Fig. 3.1 that the 3rd-order scheme is too dissipative to capture the small scale structures which are present after vortex breakdown. The

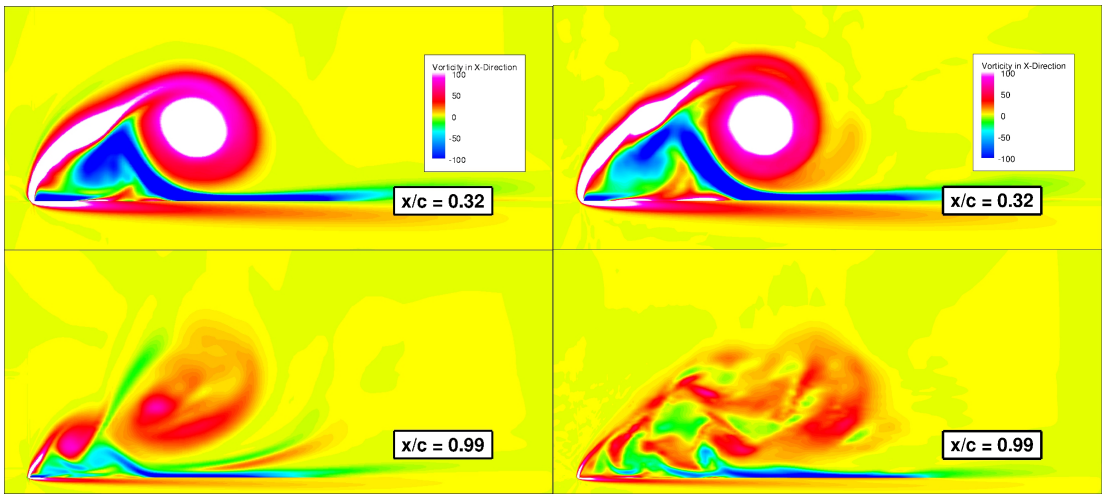

(a) 3rd-order Upwind (b) 4th-order WENO

Figure 3.1: Instantaneous Streamwise Vorticity; PANS $f_k = 0.1$; Re=26,000

4th-order scheme is able to capture the small-scale features and therefore we employ the 4th-order WENO scheme for all future delta wing simulations. The 4th-order scheme is inherently less stable, and therefore the timestep for the 4th-order scheme is approximately half of the time-step required for the 3rd-order scheme. This requirement on the time-step presents an added computational burden, however the increased resolution is worth the extra computational expense if one is interested in capturing small-scale structures. A 6th order scheme was prohibitively expensive for this study.

3.3.3 Low Reynolds Number Fine Grid Simulation and Validation

The first simulations are performed using nearly identical test conditions and an identical grid to the DNS study of Gordnier and Visbal [13]. The only difference between the two simulations is that the present study employs a 4th order spatial discretization scheme while the DNS study utilizes a 6th order scheme. The purpose

of this study is to examine the closure model capability in resolving the various flow features. Despite the fine grid, URANS is not expected to capture many of the turbulent scales of motion. Similarly, PANS is expected to capture the range of scales permitted by f_k specification. By ensuring that the grid resolution is adequate, the ability of the model to resolve flow features can be isolated.

Before starting a PANS simulation, it is useful to complete a URANS simulation to determine the appropriate values for f_k and f_ε. The results shown in Fig. 3.2 are contours of $f_k = 3\,(\Delta/\Lambda)^{(2/3)}$ and turbulent Reynolds number $R_t = k/(\omega\nu)$ for the URANS simulation at 8 streamwise stations along the chord ranging from $x/c = 0.2$ to $x/c = 0.9$. The contours of R_t clearly indicate that the turbulence levels are substantial only in the aft regions after the vortex breakdown. In the forward region, the flow is nearly laminar as expected. This clearly reveals that in the forward region all closure models and DNS should provide similar results as the flow is nearly laminar. Even more importantly, the R_t contours imply that coarsening the grid in the forward region will lead to poor resolution of the laminar vortex evolution.

The other half of Fig. 3.2 shows contours of f_k. These results indicate that the only location where one might expect to see improvement with a PANS simulation is on the aft portion of the wing after breakdown has occurred. The contours indicate that, in the aft region, the grid should support a very low f_k near zero. The implication is clear: in this region, the grid is suitable for DNS.

Following the URANS simulations, we perform PANS simulations at $f_k = 0.5$ and $f_k = 0.1$. One of the few quantitative results presented in [13] is the mean velocity magnitude along a straight line which starts at the wing apex and passes through the core of the primary vortex. The results for the mean velocity magnitude along this line are presented in Fig. 3.3a. The URANS and PANS simulations are all able to capture the mean velocity magnitude to a reasonable degree. It is well established

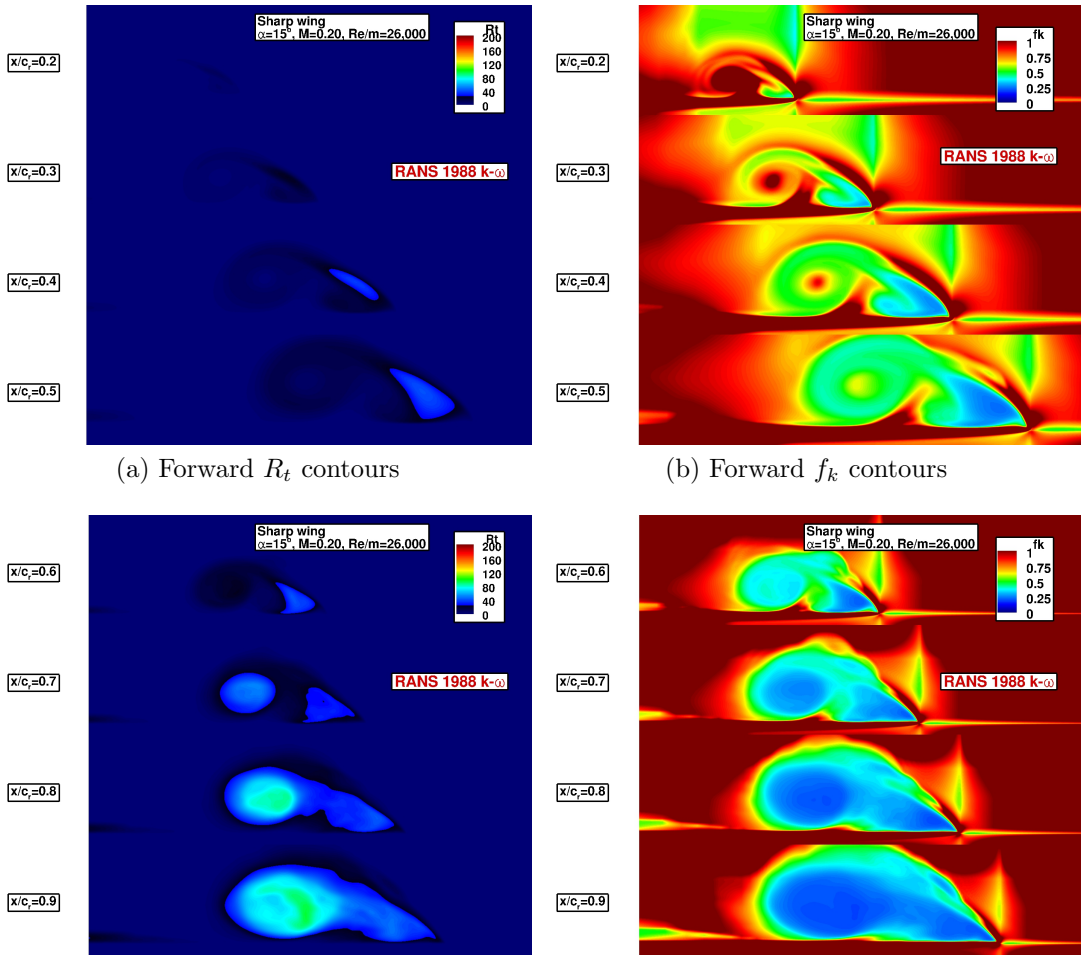

(a) Forward R_t contours

(b) Forward f_k contours

(c) Aft R_t contours

(d) Aft f_k contours

Figure 3.2: URANS Results; Re=26,000; Fine Grid

that the strong primary vortex acts in a jet-like manner accelerating the flow up until vortex breakdown where the vortex acts in a wake-like manner decelerating the flow. This trend is captured by the present simulations. The location of vortex breakdown correlates with the velocity peak, and the present simulations predict an early vortex breakdown compared to the DNS. As the primary vortex undergoes breakdown, the PANS simulations are able to more precisely predict the deceleration of the mean

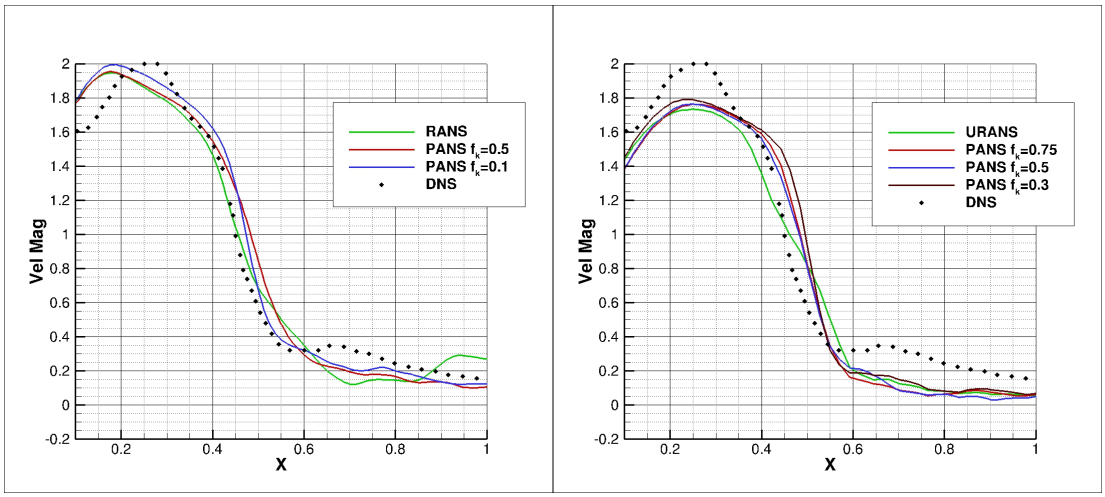

(a) Fine Grid (b) Coarse Grid

Figure 3.3: Mean Velocity through the Vortex Core; Re=26,000

velocity while the URANS simulation predicts a more gradual vortex breakdown.

Figure 3.4 shows instantaneous streamwise vorticity contours before vortex breakdown at $x/c = 0.32$ and after vortex breakdown at $x/c = 0.99$ compared to DNS results at the same locations. Before vortex breakdown there is a distinct primary and secondary vortex which is captured by each simulation at $x/c = 0.32$. After vortex breakdown, the dominant streamwise vorticity is reoriented into spanwise and wall-normal vorticity as the flow becomes fully turbulent. The URANS simulation is clearly much more dissipative compared to the PANS simulations as it is unable to capture the small scale vorticity. The $f_k = 0.5$ and $f_k = 0.1$ PANS simulations are able to resolve increasingly finer scale structures after breakdown much more than the URANS simulation, as expected. The difference between the $f_k = 0.1$ and DNS can be attributed to two reasons: (i) the finer structures are due to fluctuations that carry less than 10% of the turbulence kinetic energy, and (ii) the numerical scheme of PANS is only 4th order compared to the 6th order DNS scheme.

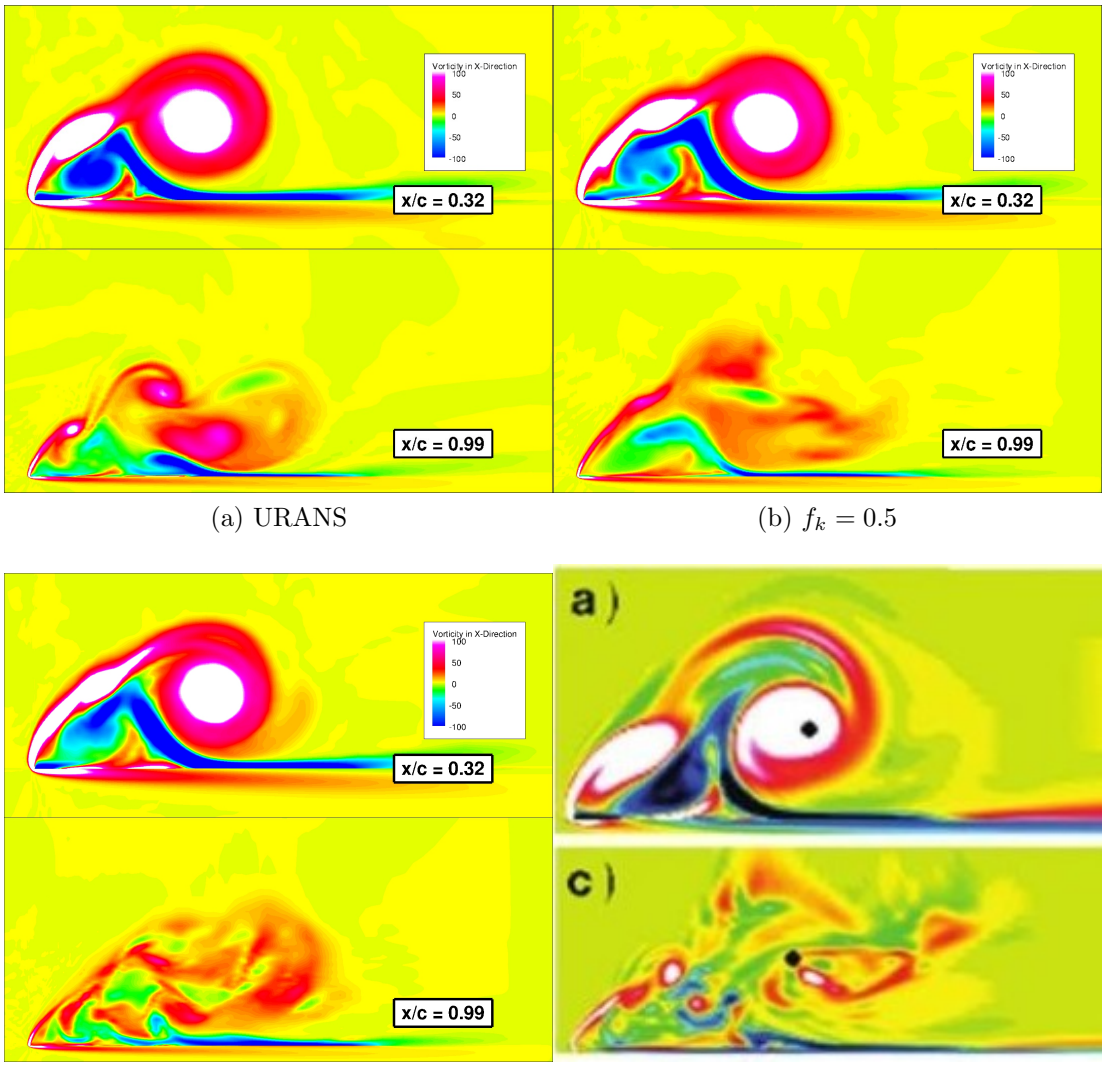

(a) URANS (b) $f_k = 0.5$

(c) $f_k = 0.1$ (d) DNS [13]

Figure 3.4: Istantaneous Contours of Streamwise Vorticity; Re=26,000; Fine Grid

The results for the mean streamwise vorticity are presented in Fig. 3.5. There are very few discernible differences in the mean vorticity between the four simulations. The URANS simulation dissipates the strength of the vorticity in the separated shear layer, while the PANS simulations preserve the intensity of the shear layer vorticity. In addition, the tertiary vortex is resolved slightly better by the PANS simulations

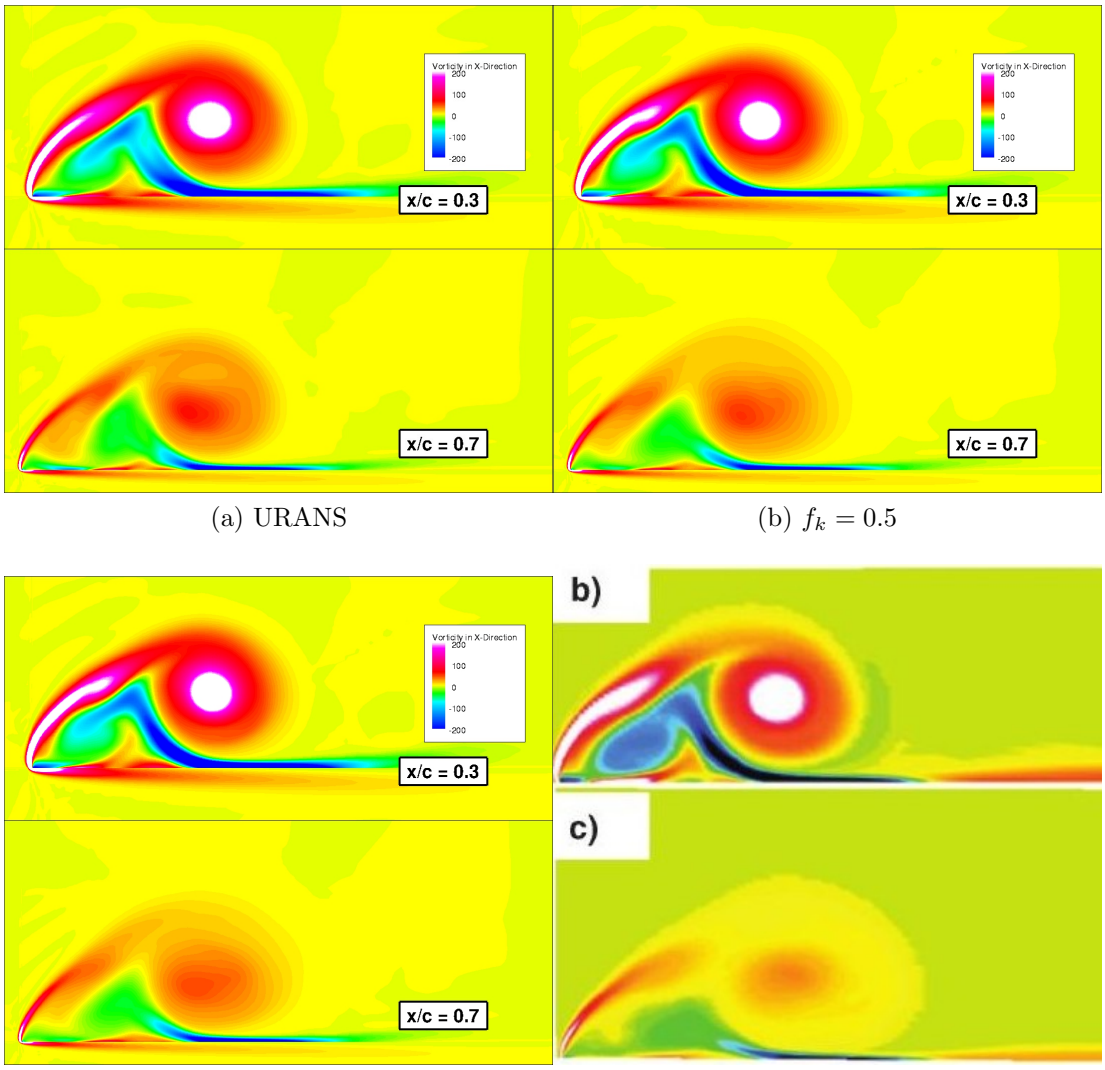

(a) URANS (b) $f_k = 0.5$

(c) $f_k = 0.1$ (d) DNS [13]

Figure 3.5: Mean Contours of Streamwise Vorticity; Re=26,000; Fine Grid

compared to the URANS simulation. However, in general, the URANS simulation performs reasonably well in predicting the mean flow structure which is not entirely unexpected given the low Reynolds number and fine grid resolution. With the mean flow velocity and vorticity reasonably well captured, we consider that the numerical procedure is adequately validated and proceed to perform further PANS calculations

with a coarsened grid.

3.3.4 Low Reynolds Number Coarse Grid Simulations

It is evident from Fig. 3.2 that the coarser grids may not be adequate in the forward region of the wing. The complex vortical flow here is nearly laminar and must be adequately resolved. In the aft region, coarser grids may be used with appropriate closure models. To examinae the effect of under-resolving the laminar portion, we perform computations on a coarser grid. To this end, the original 4.5 million cell DNS grid was coarsened to approximately 0.9 million cells by removing every other grid point in the streamwise and spanwise directions, and removing a small number of grid points in the wall-normal direction while keeping the wall spacing constant.

As in the previous section, we begin with a URANS simulation to determine the turbulence levels in the flow, and the appropriate f_k for the subsequent PANS simulations. Figure 3.6 presents results for the URANS simulation using the coarsened grid at the same flow conditions presented in the previous section. As mentioned before, the contours of R_t demonstrate that the Reynolds number of the flow is too low for any appreciable amount of turbulence to be generated until the most aft areas of the wing. Essentially, the separated vortices remain laminar until breakdown near $x/c = 0.5$. The contours of f_k in Fig. 3.6 reiterate that point. At $x/c = 0.2$, 0.3, and 0.4, the f_k contours in the core of the primary vortex remain at 1.0. This is an indication that there is essentially no turbulence in this solid body rotation vortex, and the vortex simply must be resolved with a finer grid. It is only well after vortex breakdown that enough turbulence is generated to employ any f_k reduction with a PANS simulation.

Before proceeding with the PANS simulations, it must be stated that Fig. 3.6

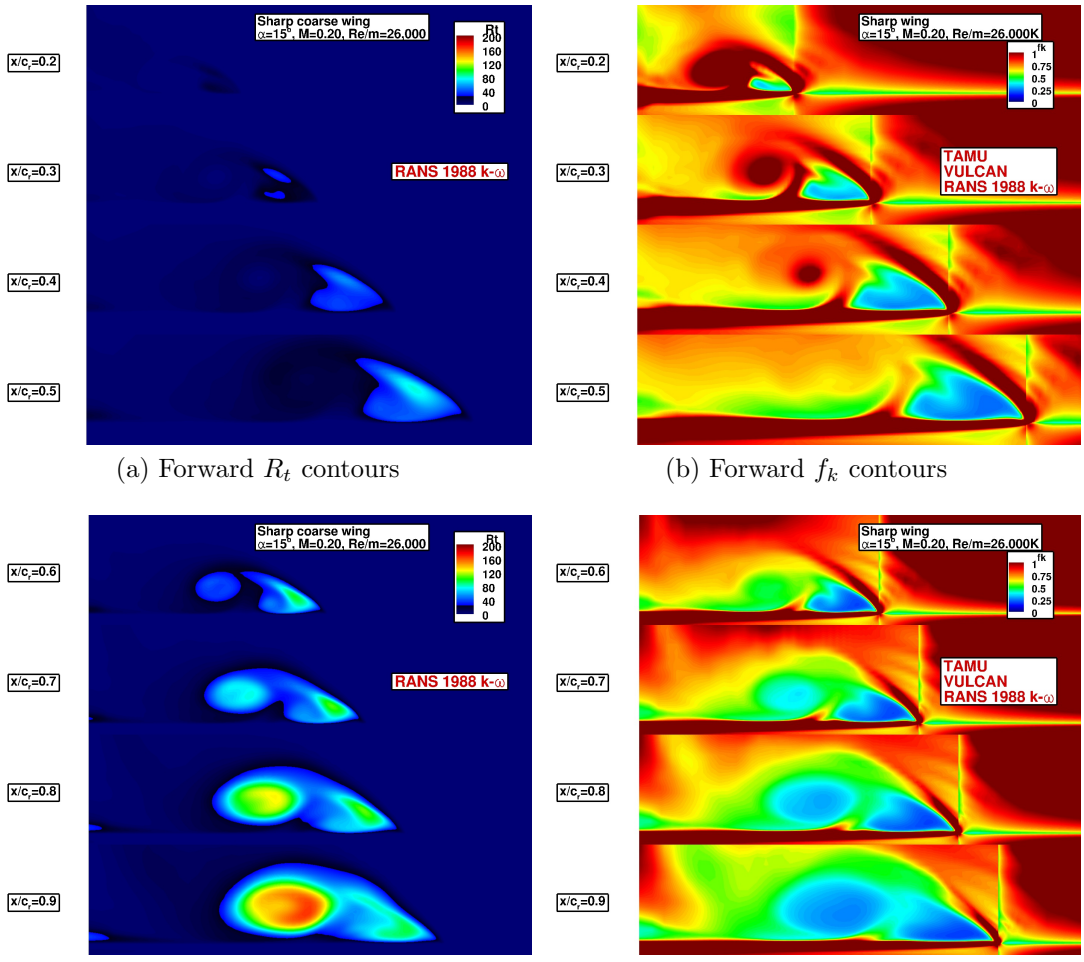

(a) Forward R_t contours

(b) Forward f_k contours

(c) Aft R_t contours

(d) Aft f_k contours

Figure 3.6: URANS Results; Re=26,000; Coarse Grid

indicates that the grid could be quite inadequate for the pre-breakdown region $x/c < 0.5$. As seen in Fig. 3.6, in this region the flow is nearly laminar and the complex features include abrubt flow separation and strong, tight vortices. If these laminar aspects are not adequately resolved over the forward half of the wing, many subsequent turbulent features may be lost despite the fidelity of the closure model.

The mean velocity magnitude along the line which passes through the core of the

primary vortex is shown in Fig. 3.3b beside the fine grid result in Fig. 3.3a. Neither the URANS simulation nor the PANS simulations are able to accurately capture the peak velocity in the vortex core. However, the PANS simulations predict the correct slope of the velocity in the core, while the URANS simulation predicts a more shallow slope indicating a slower, more dissipative breakdown. The velocity in the furthest aft portion of the wing is underpredicted by all simulations. Referring back to Fig. 3.6 which indicates that the laminar vortex requires an adequate grid resolution, the result in Fig. 3.3b demonstrates that the downstream flow features cannot possibly be modeled correctly unless the upstream region is properly resolved.

3.4 Conclusions

While most aerodynamic flows of practical relevance involve high Reynolds numbers, many of the high fidelity experimental and numerical studies are carried out at a much lower Reynolds number. Thus the development of a practical CFD tool can be extensively validated only at low Reynolds number, even though they are purported for use at significantly higher Reynolds number. In this work we perform URANS and PANS simulations of a low Reynolds number sharp leading edge delta wing flow in order to assess their performance against availabe DNS data.

The test case for this work is a sharp leading edge, flat plate delta wing at $\alpha = 15^o$ at a Reynolds number of $Re = 26,000$. We have demonstrated that a preliminary URANS simulation is beneficial in assessing whether a particular flow is likely to benefit from PANS simulations. By studying the contours of turbulent Reynolds number (R_t) and the f_k parameter, it is straightforward to determine if the case will benefit from a PANS simulation. In addition, the f_k contours provide an indication of where an increase in grid resolution may be necessary. The coarse grid results suffer from inadequate grid resolution in the pre-breakdown area. Because of

this upstream deficiency, the remainder of the downstream flow was not accurately predicted. The conclusion is that for this type of separated laminar vortical flow, one must "pay the price" and sufficiently resolve the laminar vortex which is present pre-breakdown. Both the fine grid and the coarse grid cases showed some increase in small scale structure in the PANS simulations compared to the more dissipative URANS simulations.

To realize the full benefit of higher fidelity closure, the flow must exhibit a broad turbulence spectrum. In many near-laminar unsteady flows with under-developed turbulence spectra, DNS, URANS, and PANS will yield similar results for low order statistics. Future work should be done to simulate separated delta wing flows at high Reynolds number where the increased turbulence levels would make the flow more appropriate for fine resolution modeling.

4. VARIABLE RESOLUTION SIMULATIONS OF SHARP LEADING EDGE DELTA WINGS AT LOW AND HIGH REYNOLDS NUMBER

4.1 Introduction

Recently, the delta wing has received renewed interest due to its potential application in unmanned combat aerial vehicles (UCAVs). In unmanned combat, the vehicle is expected to encounter a wider flight envelope than a manned aircraft would, including extreme angles of attack and roll. The delta wing geometry is useful in practice because of its ability to maintain lift and its stability and control properties without the need of additional flow control devices at angles of attack which would be well past stall for traditional geometries. The aerodynamic performance of the delta wing must be well understood at these limits of the flight envelope. Delta wing aerodynamics is characterized by large vortices which separate from the leading edge of the wing creating a complex separated flow field. At low angles of attack and low Reynolds numbers the vortical flow is relatively steady, however with increasing angles of attack and Reynolds number, the flow features become progressively more unsteady with increasingly more broad spectrum turbulence. The delta wing has received considerably less attention in literature than traditional wings and airfoils. Although some of the elementary features of the delta wing flow are known, more work needs to be done to establish different features occuring at different scales of resolution. It is also important to establish which small scale features impact the integrated wing properties such as the surface pressure and lift coefficients.

The dominant flow features which are of interest for the delta wing are the location of primary and secondary vortex separation and reattachment, the alignment of the vortex structure, and the location of vortex breakdown. These flow features are

dependent upon the wing shape, leading edge radius, leading edge sweep angle, angle of attack, and Reynolds number. As modern UCAVs are likely to employ moderate sweep angles near 50^o, so-called nonslender delta wings warrant further study. The sharp leading edge delta wing presents a less demanding challenge to simulate as compared to the round leading edge case. The computational burden can also be eased by simulating the delta wing at low Reynolds number. Although the low Reynolds number simulations are not representative of realistic flight conditions, they are useful for evaluating the performance of numerical models at capturing the relevant flow physics.

There have been computational and experimental studies performed on delta wings with various leading edge sweep angles and leading edge curvature. For the present study, the previous literature specific to sharp leading edge delta wings with 50^o leading edge sweep is most pertinent, and it is summarized here. A high-fidelity CFD data set was generated by the direct numerical simulation study (DNS) of Gordnier and Visbal [13]. Their DNS computes a sharp leading edge delta wing with 50^o sweep angle at $Re = 26,000$ at 5^o, 10^o, and 15^o angle of attack using a 6th order compact differencing scheme, with an 8th order low pass spatial filter. The results from [13] mostly include visualizations of flow features such as a dual primary vortex structure, the presence of a strong secondary vortex, and unsteady features such as vortex breakdown, and Rayleigh-Taylor-like instabilities in the vortex shear layer. Gordnier et al [16] have performed 6th-order implicit LES on the same 50^o swept delta wing at more realistic flight Reynolds numbers: $Re = 2.0e5$, $Re = 6.2e5$, and $Re = 2.0e6$ and at an angle of attack $\alpha = 15^o$ which produces a large primary vortex and a distinct location of breakdown. Experimental PIV data were obtained for the two lower Reynolds number. Taylor and Gursul [49] have performed an experimental investigation of a sharp leading edge delta wing with 50^o leading edge

sweep. Experiements were performed in a water tunnel to study the delta wing at a low Reynolds number of $26,000$ and in a wind tunnel to study the wing at a high Reynolds number of $660,000$. The locations of the vortex separation and attachment lines are reported for both low and high Reynolds number. These experimental data sets and the aforementioned high fidelity computations are useful as a benchmark for evaluation of turbulence modeling techniques. The 50^o-swept sharp leading edge delta wing of [13] was also studied in Section 3 at $Re = 26,000$. The results from this study indicate that the upstream vortex structure is largely laminar and must be well-resolved by the grid in order to accurately compute the downstream vortical flow. If an adequate grid is employed then some of the flow features will be captured by a URANS simulation while other small-scale features require increased model resolution. The 53^o-swept round leading edge diamond wing of the NATO AVT-183 campaign has been studied in Section 2 at $Re = 3,000,000$ using steady-state RANS turbulence modeling. The lift and drag coefficients matched experimental data well, and the surface pressure coefficients also showed good agreement with data except in the area very close to primary vortex separation.

The objective of the present work is to establish the flow features which are present at different levels of turbulence resolution. To accomplish this URANS and PANS simulations at different resolution levels will be carried out at low and high Reynolds numbers. The low Reynolds number case will be compared against the DNS of Gordnier and Visbal [13] while the high Reynolds number case will be compared agaist the ILES of Gordnier et al [16]. This paper is organized in the following manner: Section 4.2 provides a thorough summary of the vortical flow physics. Section 4.3 discusses the PANS turbulence model used for these simulations. Section 4.4 details the CFD tool and flow configurations which are studied. Section 4.5 presents results for the PANS simulations at $Re = 26,000$ and $\alpha = 15^o$ and compares against

existing low Reynolds number data. Section 4.6 presents results for the PANS simulations at $Re = 620,000$ and $\alpha = 15^o$ and 23^o and compares against existing high Reynolds number data. Section 4.7 discusses the conclusions of the results and future work.

4.2 Fundamental Flow Features

The present sutdy is focused on accurate modeling of the pertinent physics of sharp leading edge delta wings. The literature describing the flow features of sharp leading edge delta wing flow is summarized here. The earliest studies analyzed delta wings with large ($> 60^o$) leading edge sweep angles and sharp leading edges [41] [20] [29] [46]. For delta wings with sharp leading edges, the vortex will always separate at the sharp leading edge, beginning at the wing apex. The abrupt separation creates a shear layer where the fast-moving freestream interfaces with the slow-moving fluid on the suction side of the wing. The shear layer rolls up into a distinct primary vortex and is drawn towards the wing centerline and then down towards the surface of the wing where it reattaches. The intensity of the vortex is highest near the apex of the wing. The tightly-wound vortex behaves like a jet flow, accelerating fluid through its core creating a potent suction on the upper surface of the wing. For a schematic of the vortex flow, see Fig. 4.1.

After reattachment of the primary vortex, the surface streamlines are drawn outward towards the leading edge due to the presence of the strong suction in the vortex core. Once the surface streamlines pass the axis of the vortex core, a strong adverse pressure gradient is encountered. Eventually, the adverse pressure gradient causes the reattached flow to separate into a secondary vortex beneath the larger primary vortex, with the opposite sign of vorticity. It is well-known that, compared to a laminar boundary layer, a turbulent boundary layer is able to withstand such an ad-

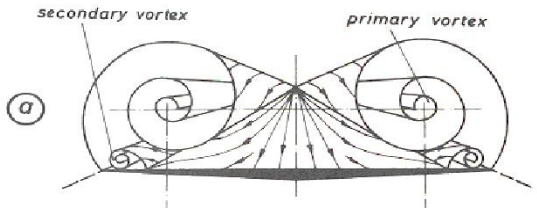

Figure 4.1: Schematic of Primary and Secondary Vortex Flow (Reprinted with permission from: Dietrich Hummel. "On the Vortex Formation Over a Slender Delta Wing at Large Angles of Incidence." Technical Report 15, Technische Universitat Braunschweig, 1978. [20])

verse pressure gradient for a greater distance before separating. This is also true for the present vortex flow case; a laminar reattached boundary layer will promote secondary vortex separation and cause the secondary vortex to be located more inboard compared to a turbulent reattached boundary layer. Thus the laminar/turbulent status of the reattached boundary layer plays a role in determining the structure of the primary/secondary vortex formation. In the region close to the wing apex, the traditional primary/secondary vortex structure is steady and appears to be laminar for many cases which have been studied. As expected, for low Reynolds numbers the well-defined primary/secondary vortex structure maintains its integrity for some distance downstream, while high Reynolds number flows experience instabilities which degrade the well-defined structure of the primary/secondary vortices closer to the wing apex. The boundary layer from the lower surface of the wing plays no significant role in the shear layer, especially in the wing apex region where there is insufficient distance for an appreciable boundary layer to develop on the lower surface.

As the vortical structures convect downstream, unsteady instabilities appear. The instabilities pertinent to the separated vortices have been the topic of extensive research. The unsteady instabilities have been attributed to the well known Kelvin-

Helmholtz instability by several authors [7], [40], [30], and [14]. Alternatively, Gursul [17] concluded that the dominant unsteadiness arises from the shear layer following a helical path around the vortex core, termed the helical mode instability. On the interior of the vortex strucutre, the secondary vortex interacts with the primary vortex and the separated shear layer, further complicating the stability and structure of the flow field.

After sufficent distance, the various instabilities in the vortex structure grow and cause the vortex to breakdown. The vortex breakdown is characterized by the loss of a definitive axial vortex core, a switch from a jet-like core to a wake-like region, large velocity fluctuations, and greater turbulence. The breakdown of the primary vortex can adversely influence the performance of the delta wing in a number of ways: buffeting, loss of lift, and unstable pitching and roll behavior. The multi-scale vortical flow features can be seen in Fig. 4.2 which shows the axial vorticity at Re=620,000.

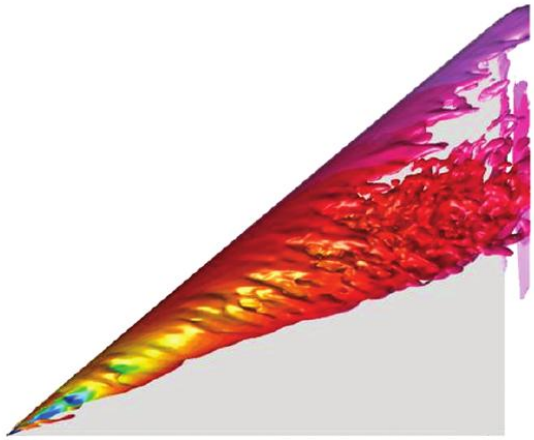

Figure 4.2: Multi-scale Vortical Structures; $Re = 620,000$ [16]

The vortex breakdown process has been the topic of great interest and debate

in literature. In general, two separate types of vortex breakdown have been documented: spiral and bubble. In both cases, the location of breakdown is determined by the location where the vortex changes from a jet-like behavior to a wake-like behavior, and an abrupt expansion in the vortex core. The bubble-type breakdown occurs with a stagnation point along the vortex core, followed by an oval-shaped, symmetric expansion of the core. The spiral-type breakdown exhibits a similar character, however the rapid expansion of the vortex core does not occur symmetrically; instead the streamlines follow a spiral around the expanding core. Gordnier [15] indicates that a 3D stagnation point does not exist for the spiral-type breakdown. The expansion of the vortex core occurs more rapidly for the bubble-type breakdown compared to the spiral-type breakdown. There remains considerable debate as to whether the bubble and spiral breakdown types are the only types of breakdown processes.

As expected, vortex breakdown is affected by the same flow parameters which affect the pre-breakdown vortex structure. An increase in angle of attack tends to move the vortex breakdown location forward until the limit of stall where there is no longer a distinct vortex. An increase in leading edge sweep, however, tends to move the vortex breakdown location aft. The breakdown location for wings with a sharp leading edge is not strongly influenced by Reynolds number, however the Reynolds number does influence the turbulence levels in the wake of the vortex. The presence (or absence) of pressure fluctuations has a profound effect on the breakdown location. The geometry of the wing apex region also plays a significant role in the breakdown dynamics [31], along with the geometry of the leading edge. The location of vortex breakdown may also oscillate over a distance as much as 10% of the wing chord for very large incidence angles. The osciallation appears to be related to the fluid dynamics of the primary vorticies, and not related to facility-related disturbances,

the Kelvin-Helmholtz instability, or the helical mode instability due to the disparate frequencies of each [35].

In summary, the dominant physics of the vortical flow over delta wings has been documented. The vortex flow is very complicated inasmuch as it encompasses the entire spectrum between laminar and turbulent, separated and attached, jet-like and wake-like, and a strong large-scale vortex aligned in the streamwise direction which breaks down into small-scale vortices in all three directions. The complexity of the flow and the levels of turbulence in the flow increase with increasing angle of attack and Reynolds number. In order to asses the ability of current turbulence models at capturing the relevant flow features, we choose to move forward with a study of a nonslender, 50^o-swept, sharp leading edge delta wing.

4.3 Description of the PANS Turbulence Model

This work utilizes the PANS $k-\omega$ model which is derived by Lakshmipathy [26]. The PANS model purports to provide variable resolution of the turbulence energy spectrum. This is achieved by applying an arbitrary filter to the Navier Stokes equations, in contrast to an average which would produce the RANS equations. The velocity and pressure fields are decomposed into the sum of a resolved and unresolved portion, in constrast to the sum of a mean and fluctiating portion as in Reynolds decomposition. The application of an arbitrary filter is discussed in Germano [9], and the resulting equations are:

$$u_i = \langle u_i \rangle + u_i'; \quad p = \langle p \rangle + p'; \quad \tau\big(u_i, u_j\big) = \langle u_i u_j \rangle - \langle u_i \rangle \langle u_j \rangle \tag{4.1}$$

$$\frac{\partial \langle u_k \rangle}{\partial x_k} = 0 \tag{4.2}$$

$$\frac{\partial \langle u_i \rangle}{\partial t} + \frac{\partial \langle u_i \rangle \langle u_j \rangle}{\partial x_j} = -\frac{\partial \langle p \rangle}{\partial x_i} + 2\nu \frac{\partial \langle s_{ij} \rangle}{\partial x_j} - \frac{\partial \tau\big(u_i, u_j\big)}{\partial x_j} \tag{4.3}$$

After application of the filter, an additional term emerges $\tau(u_i, u_j)$ which is called the generalized central moment. This filtering approach utilizes an arbitrary filter, and is therefore a general approach. On the other hand, Reynolds averaging employs either a time-average or ensemble-average, which can be viewed as a sub-set of the general averaging employed above. The generalized central moment term is analogous to the Reynolds stress term which appears after Reynolds-averaging and the sub-filter stress (SFS) in the context of LES. The preceding equations are filter invariant, and subsequently the generalized central moment term is invariant to the type of averaging. The PANS model is a variable resolution model which purports to model a user-specified portion of the turbulence energy spectrum. The resolution is determined by the filter control parameters:

$$f_k = \frac{k_u}{k}; \qquad f_\varepsilon = \frac{\varepsilon_u}{\varepsilon} \tag{4.4}$$

The parameter f_k, which may vary between zero and unity, specifies the ratio of unresolved-to-total turbulence kinetic energy. A value of zero for f_k indicates that none of the turbulence energy spectrum is unresolved; the entire spectrum must be resolved by the grid. A value of unity for f_k indicates that the entire spectrum is unresolved which is identical to a RANS simulation. In essence, the f_k parameter specifies the spectral cutoff for the simulation. The parameter f_ε specifies the ratio of unresolved-to-total dissipation, and it may also vary between zero and unity. The value for f_ε will be unity unless the spectral cutoff is in the dissipative scales. The present derivation will follow a $k-\omega$ paradigm, thus we also must specify the ratio of unresolved-to-total turbulence frequency:

$$f_\omega = \frac{\omega_u}{\omega} = \frac{\varepsilon_u / (\beta^* k_u)}{\varepsilon / (\beta^* k)} = \frac{f_\varepsilon}{f_k}. \tag{4.5}$$

After specification of the spectral cutoff, one must choose an approach to close the generalized central moment term and thereby model the unresolved field. With PANS modeling, we intend to resolve the dynamically important scales, but significantly less scales than a typical LES. Since the cutoff will typically be between RANS and LES, we require a sub-filter closure model which is more sophisticated than LES. For this reason, and the robustness of two-equation RANS models, we choose to use a Boussinesq-like two-equation closure approach for the PANS unresolved field.

$$\tau\left(u_i,u_j\right)=-\nu_u\left(\frac{\partial\langle u_i\rangle}{\partial x_j}+\frac{\partial\langle u_j\rangle}{\partial x_i}\right)+\frac{2}{3}k_u\delta_{ij};\quad \nu_u=\frac{k_u}{\omega_u}=\frac{f_k k}{f_\omega\omega} \tag{4.6}$$

We proceed to derive evolution equations for the PANS unresolved kinetic energy k_u and the unresolved turbulence frequency ω_u, taking inspiration from the original RANS 1988 Wilcox $k-\omega$ model [51]. The full details of the derivation can be found in [26]. The final form of the PANS $k-\omega$ model equations can be summarized as:

$$\frac{\partial k_u}{\partial t}+\langle u_j\rangle\frac{\partial k_u}{\partial x_j}=P_u-\beta^* k_u\omega_u+\frac{\partial}{\partial x_j}\left[\left(\nu+\frac{\nu_u}{\sigma_{ku}}\right)\frac{\partial k_u}{\partial x_j}\right] \tag{4.7}$$

$$\frac{\partial \omega_u}{\partial t}+\langle u_j\rangle\frac{\partial \omega_u}{\partial x_j}=\alpha\frac{P_u\omega_u}{k_u}-\beta'\omega_u^2+\frac{\partial}{\partial x_j}\left[\left(\nu+\frac{\nu_u}{\sigma_{\omega_u}}\right)\frac{\partial \omega_u}{\partial x_j}\right] \tag{4.8}$$

The RANS closure coefficients are unchanged for α and β^*, while the remaining closure coefficients are modified as given below:

$$\sigma_{ku}\equiv\sigma_k\frac{f_k}{f_\omega};\qquad \beta'\equiv\alpha\beta^*-\frac{\alpha\beta^*}{f_\omega}+\frac{\beta}{f_\omega};\qquad \sigma_{\omega u}\equiv\sigma_\omega\frac{f_k}{f_\omega} \tag{4.9}$$

The user can achieve accuracy-on-demand by varying the filter control parameter from a coarse RANS simulation to a fully-resolved DNS simulation, provided that the

grid can support such a resolution. The derivation of the PANS model is originally performed by Girimaji [10], and it has been applied to numerous flows for validation: [28], [37], [3], [47], [11], and [27].

4.4 Numerical Tool and Flow Geometry

The simulations are performed with the CFD code VULCAN (Viscous Upwind aLgorithm for Complex flow ANalysis). The code was developed and is maintained by researchers at NASA Langley in Hampton, VA. It is a finite volume, turbulent, non-equilibrium, finite-rate chemical kinetics, Navier-Stokes flow solver for structured, cell-centered, multi-block grids. The code is parallelized using MPI, and the majority of the simulations for this work were performed using ~ 500 processors. The present simulations utilized the PANS turbulence model at various levels of resolution. The results labeled as URANS are PANS $f_k = 1.0$ simulations, which is equivalent to the 1988 Wilcox $k - \omega$ model. The Roe upwind scheme is used with 4th order WENO interpolation, although the code has many other schemes available. The turbulence production-to-dissipation ratio was limited to 200 in order to aid in robustness of the simulations, and the solution was integrated to the wall without the use of any wall functions.

The wing geometry studied in this work is a 50^o swept, half-span, flat plate delta wing. The grid used for this study is the same 4.48M cell single-block grid which was used for the work of Gordnier and Visbal [13]. The grid domain extends 1 chord length forward of the wing apex, 1.5 chord lengths aft of the wing trailing edge, and 2 chord lengths above and below the upper and lower surfaces of the wing. Gordnier and Visbal [13] provide a dicussion of the grid development details, including grid refinements which were made in the vortex region to provide adequate flow resolution. The high Reynolds number simulations utilized a grid with the same

4.48M cells but the mesh was refined in the near-wall region. The mean results are averaged over approximately 10 flow-through times. Each flow-through time required approximately 9,400 processor-hours. The freestream flow conditions used for this work are presented in Table 4.1.

Table 4.1: Freestream conditions

Mach Number	Reynolds Number	α
0.2	26,000; 620,000	15^o; 23^o

4.5 PANS Simulation Results at Low Reynolds Number

Before starting a PANS simulation, it is useful to complete a URANS simulation to determine the appropriate values of f_k and f_ε for subsequent PANS simulations. Figure 4.3 is a schematic of a typical turbulence energy spectrum where the length, time, and velocity scales are shown for the large, energy-containing scales and the small, dissipative scales. The definitions of the largest ($L = k^{3/2}/\varepsilon$) and smallest ($\eta = (\nu^3/\varepsilon)^{1/4}$) turbulence scales from Fig. 4.3 allows for one to compute the width of the turbulence spectrum in the flow. The ratio of the largest-to-smallest turbulence scales (L/η) is presented in the contours of Fig. 4.4. The width of the turbulence spectrum within the vortex core is essentially unity until $x/c = 0.5$ where breakdown occurs. In the aft portion of the wing, the turbulence spectrum widens, but only to approximately $L/\eta \approx 250$, or less than 3 decades. Because the turbulence spectrum for this case appears to be relatively narrow, we expect that the URANS and PANS simulation results will not differ much, except in the regions well after vortex breakdown.

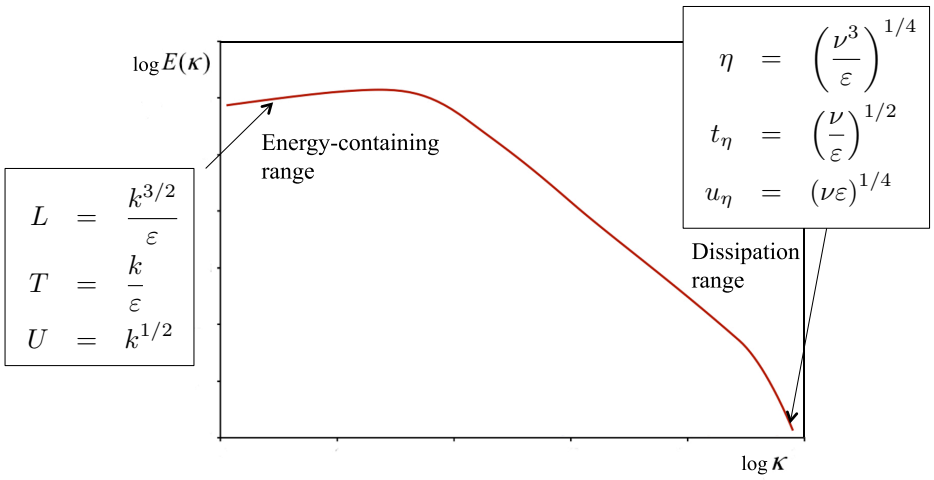

Figure 4.3: Turbulence Energy Spectrum

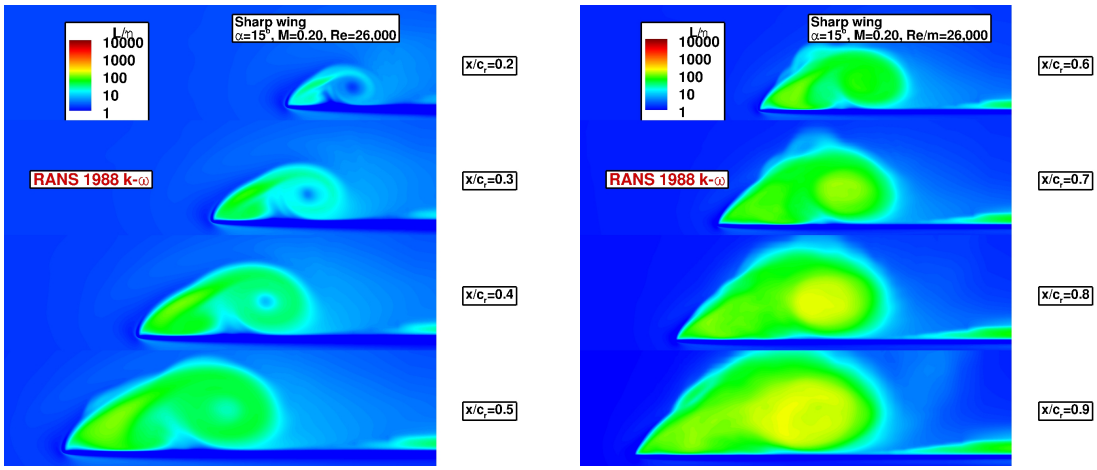

(a) Forward L/η contours

(b) Aft L/η contours

Figure 4.4: URANS L/η Results; $\alpha = 15^o$; $Re = 26,000$

4.5.1 Integrated Results

Following the URANS simulations, we perform PANS simulations at $f_k = 0.5$ and $f_k = 0.1$ while holding $f_\varepsilon = 1.0$. Results for integrated quantities such as C_p,

mean vorticity, and the locations of primary vortex separation and reattachment will be presented first.

In Taylor and Gursul [49], the spanwise location of the primary vortex core is shown for many experiments and computational studies ([39], [36], [13]) as a function of Reynolds number and α. These data are reproduced here, with the results from the present simulations added to the data set in Fig. 4.5a. The PANS simulations at $f_k = 0.5$ and $f_k = 0.1$ both predict the same vortex core location and their data points are combined into a single PANS data point. The PANS data are also essentially identical to the URANS data point. In essence, the location of the vortex core can be accurately captured by a URANS or PANS simulation. Figure 4.5b

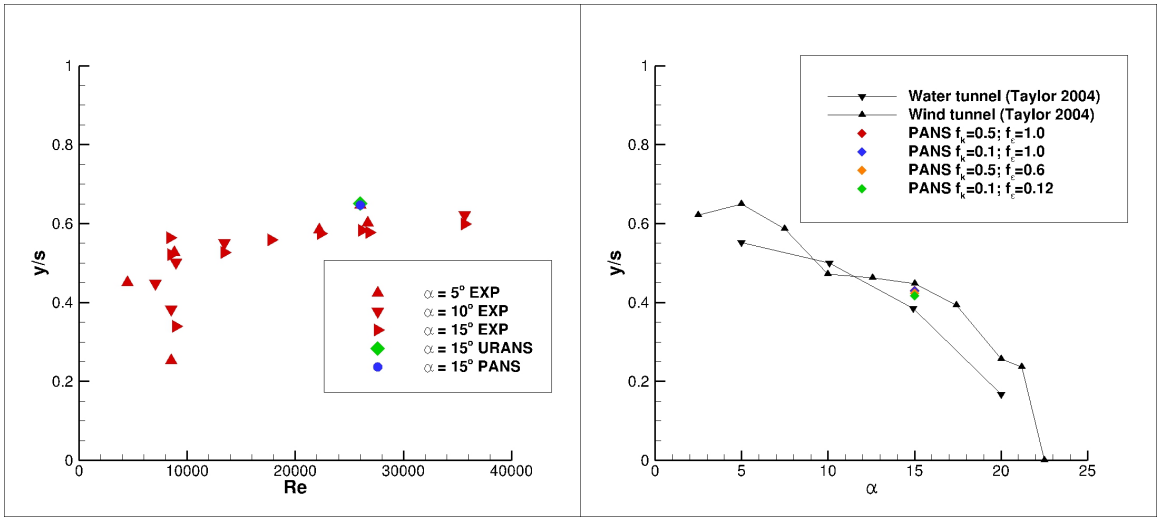

(a) Location of primary vortex core

(b) Location of primary vortex reattachment

Figure 4.5: Mean Primary Vortex Statistics

shows the spanwise location of the primary vortex reattachment line compared with experimental data from Taylor and Gursul [49]. The water tunnel and wind tunnel

experiments were carried out at $Re = 26,000$ and $Re = 660,000$ respectively. The PANS simulations show some variation with changing values for f_k and f_ε, however, all the simulations are consistent with the experimental data.

The pressure coefficient on the upper surface of the wing is shown in Fig. 4.6 at several stations along the chord. The URANS and PANS simulations are all

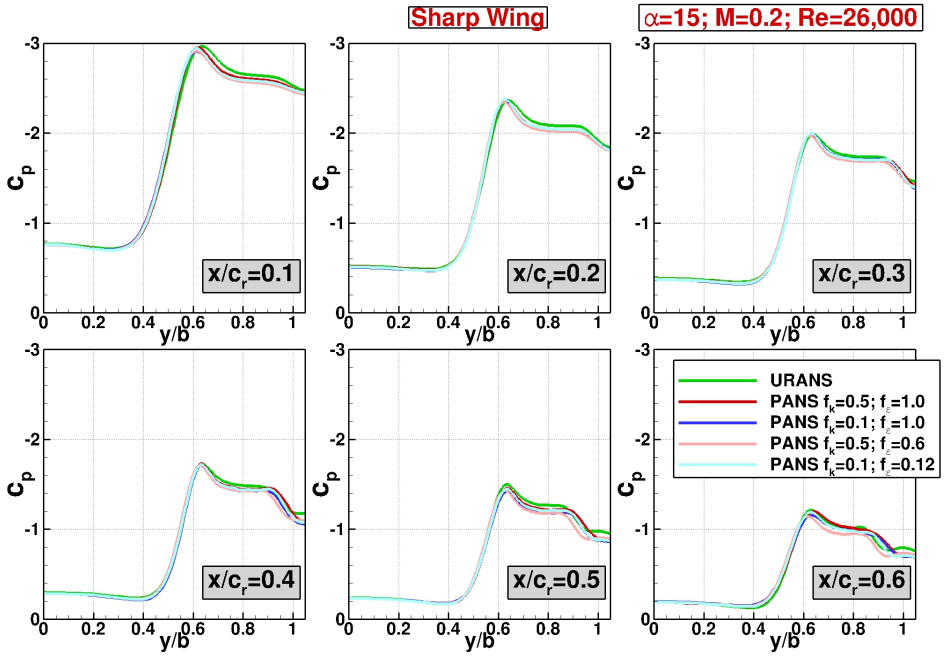

Figure 4.6: Mean Surface C_p; $\alpha = 15^o$; $Re = 26,000$

essentially identical through $x/c = 0.3$. Small differences between the simulations begin to appear at $x/c = 0.4$ and the differences amplify moving aft on the wing. The message, once again, is that in the forward region of the wing the flow is nearly laminar and the results are independent of the choice of turbulence model, provided adequate grid resolution.

The mean streamwise vorticity can be seen at $x/c = 0.3$ and $x/c = 0.7$ in Fig.

4.7. The results from the DNS of Gordnier and Visbal are shown in Fig. 4.7d, while the present simulation results are shown in Figs. 4.7a, 4.7b, and 4.7c. In Fig. 4.7

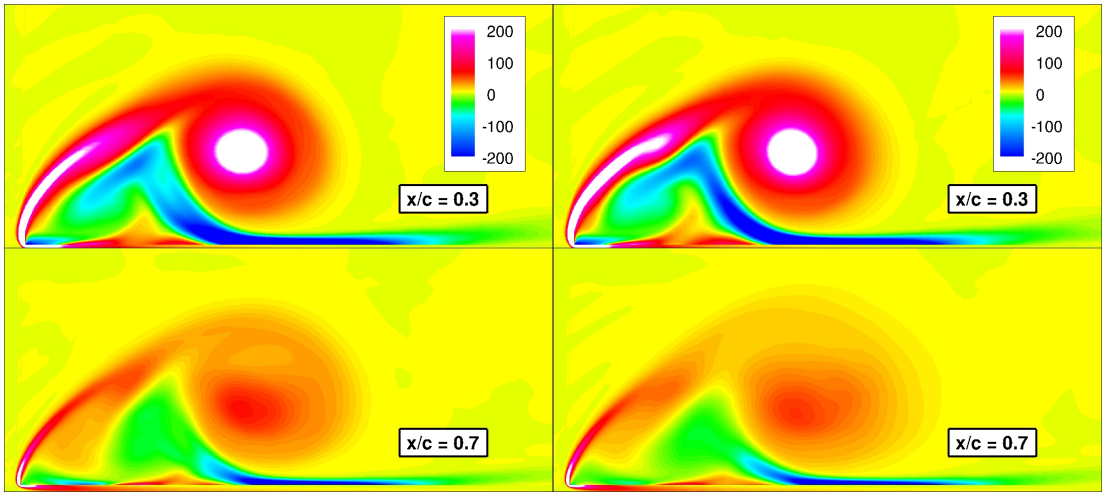

(a) URANS

(b) PANS $f_k = 0.5$

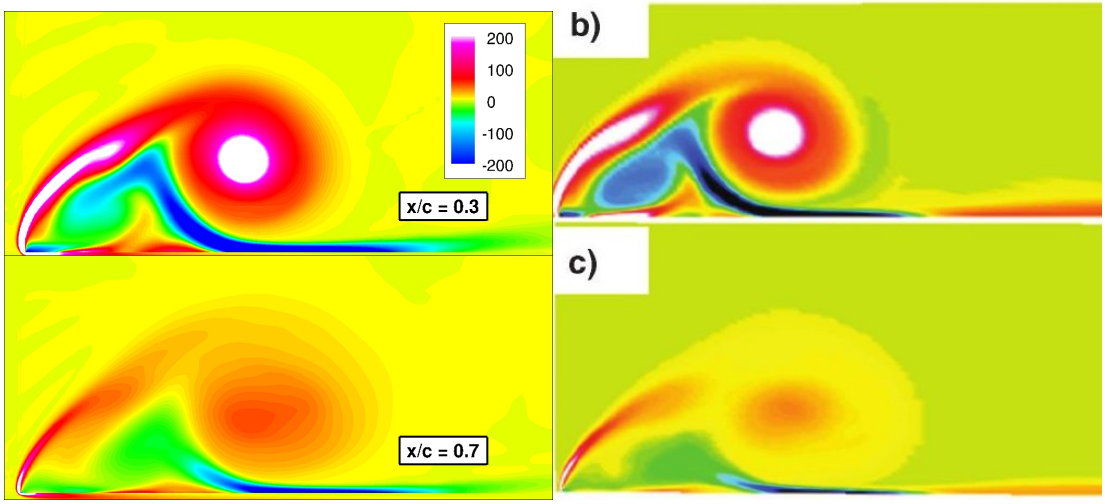

(c) PANS $f_k = 0.1$

(d) DNS [13]

Figure 4.7: Mean Axial Vorticity at $x/c = 0.3$ and $x/c = 0.7$; $\alpha = 15^o$; $Re = 26,000$

the flow is into the page. The primary vortex separates from the surface of the wing

on the left side of the figures, rolls upwards, and then towards the wing centerline on the right side of the figures. The high concentration of positive vorticity in the core at $x/c = 0.3$ is an indication of the strength of the primary vortex before breakdown occurs. At $x/c = 0.7$ the core has lost the intense concentration of vorticity which indicates that breakdown has already occured by this point. The secondary vortex can also be visualized in the green and blue contours beneath the primary vortex. A small tertiary vortex can also be seen in the slightly red contours beneath the secondary vortex. The URANS and PANS simulations are all able to capture the mean vorticity in the flow over the wing. However, there are a few features which are not captured by the URANS simulation. First, the separated shear layer contains very intense vorticity in the DNS results. The URANS simulation does not capture the intensity of the shear layer vorticity, while the PANS simulations do predict a more intense shear layer. Next, the same observation can be made regarding the negative vorticity in the secondary vortex; the URANS simulation does not capture the intensity of the streak of negative vorticity leading into the secondary vortex, while the PANS simulations are able to capture this feature. However, the differences between the URANS and PANS simulation are very minor due to the fact that the turbulence spectrum is narrow.

4.5.2 Effects of Increased Model Resolution

The previous section showed the flow features which could be accurately captured by a either a URANS or PANS simulation. In this section we identify which aspects of the flow require a reduced f_k PANS simulation to accurately capture. The instantaneous vortical structure of the flow is presented in Fig. 4.8 compared against the flow structures seen in DNS. The DNS results are presented for the full wing while the URANS and PANS results are only presented for the semi-span wing. The re-

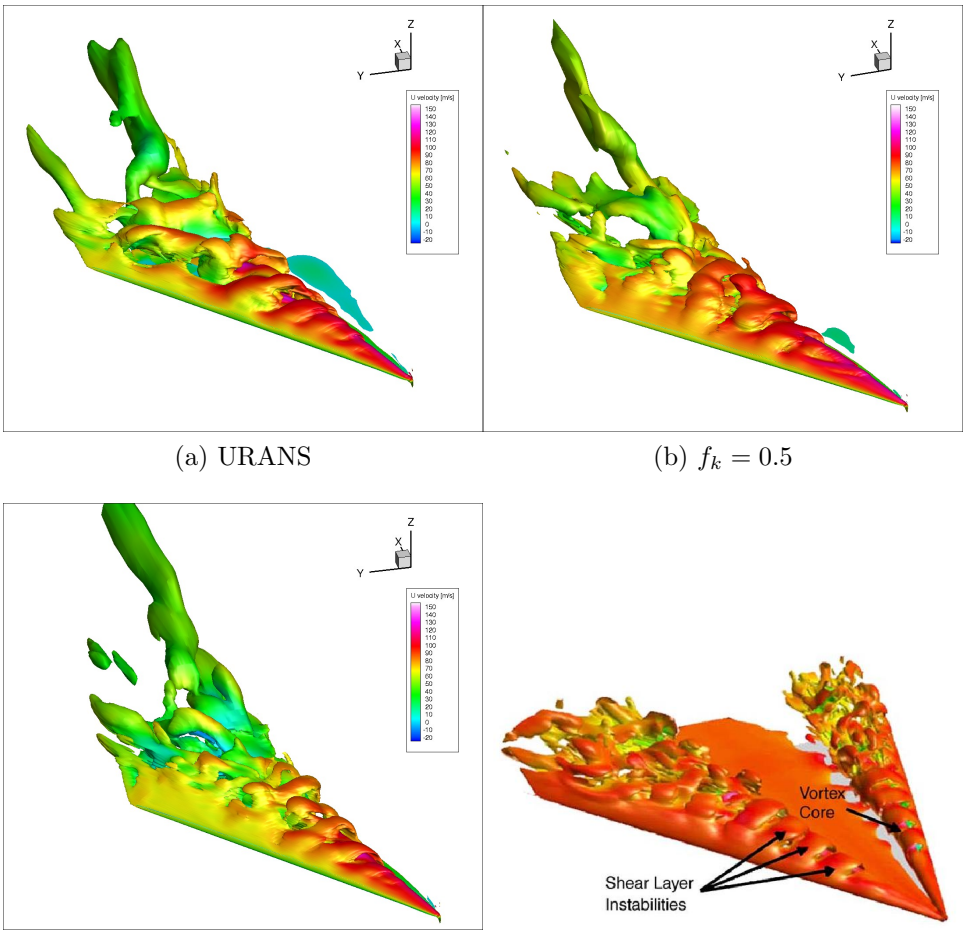

(a) URANS (b) $f_k = 0.5$

(c) $f_k = 0.1$ (d) DNS [13]

Figure 4.8: Isosurface of Streamwise Vorticity; $\alpha = 15^o$; $Re = 26,000$

sults clearly show an increase in small scale structure as f_k is reduced. The URANS results only capture the largest unsteady structures, while the $f_k = 0.1$ results are able to resolve many of the finer structures after vortex breakdown. While the DNS results do exhibit even finer structures than the $f_k = 0.1$ results, this can likely be attributed to the 4th order scheme which the PANS simulations used, compared to the 6th order scheme which the DNS used.

In Fig. 4.9 we present instantaneous streamwise vorticity contours at $x/c =$

0.32 which is before vortex breakdown and $x/c = 0.99$ which is well after vortex breakdown. The results from the DNS of Gordnier and Visbal [13] are shown in Fig. 4.9d, the present URANS simulation result is shown in Fig. 4.9a and the results from our PANS simulations are shown in Fig. 4.9b for $f_k = 0.5$ and Fig. 4.9c for $f_k = 0.1$. The DNS results in Fig. 4.9d at $x/c = 0.32$ clearly show the primary, secondary, and tertiary vortex structure. In addition, there is another area of very strong positive vorticity just above the leading edge of the wing. This is the dual primary vortex structure which is discussed in [13]. At $x/c = 0.99$ the primary vortex has clearly broken down because there is no discernable dominant vortex. The PANS results also show the strong primary, secondary, and tertiary vortex structure at $x/c = 0.32$ and vortex breakdown by $x/c = 0.99$. However, the $f_k = 0.5$ results do not show the fine-scale structures which are visible in the DNS results. In fact, these instantaneous results more closely resemble the time-averaged results in Fig. 4.7b. After vortex breakdown the vorticity is more washed out and there is limited fine-scale structure. The results for $f_k = 0.1$ in Fig. 4.9c show more unsteady features and fine-scale structure at $x/c = 0.32$ as compared to the $f_k = 0.5$ case. There is also a dual primary vortex which forms outboard of the main primary vortex. At $x/c = 0.99$ the vortex has broken down. There are many more fine scale structures in the $f_k = 0.1$ results compared to the $f_k = 0.5$ results.

We qualitatively compare the structure of instantaneous x-vorticity to the DNS of Gordnier and Visbal [13] in Fig. 4.10 on a vertical slice through the core of the primary vortex. The URANS, PANS $f_k = 0.5$, and PANS $f_k = 0.1$ results are shown in Figs. 4.10a, 4.10b, and 4.10c respectively. The URANS vorticity result clearly shows an absence of small scale structure compared to the DNS result, while the PANS $f_k = 0.5$ and $f_k = 0.1$ results clearly show an increase in small scale structure tending towards the DNS result. Once again, the present simulations are limited

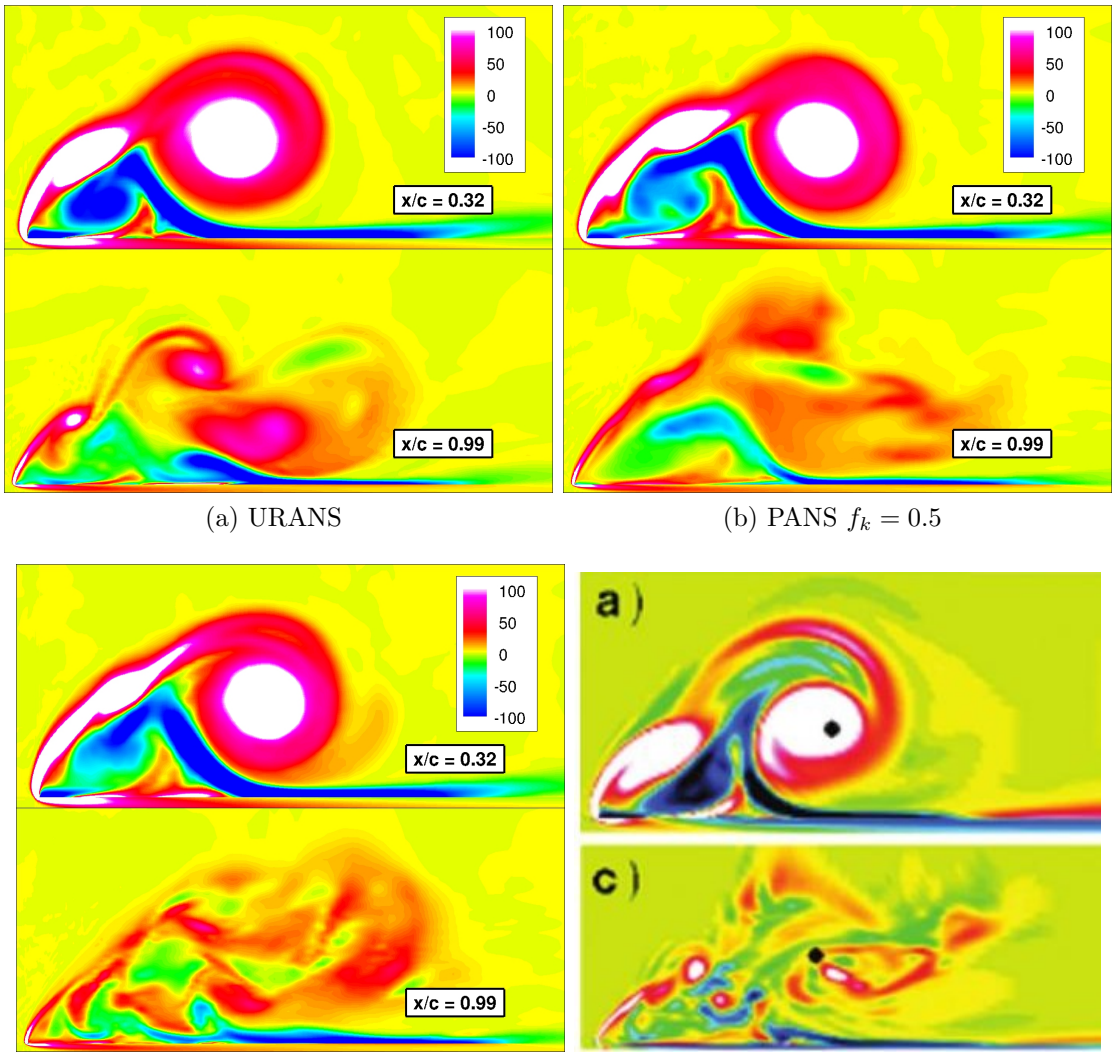

(a) URANS

(b) PANS $f_k = 0.5$

(c) PANS $f_k = 0.1$

(d) DNS [13]

Figure 4.9: Instantaneous Axial Vorticity at $x/c = 0.32$ and $x/c = 0.99$; $\alpha = 15^o$; $Re = 26,000$

in their ability to resolve the smallest structures due to the lower-order scheme, so we cannot capture the smallest scales which are present in the DNS simulation. The instabilities in the primary vortex shear layer are resolved well by both PANS simulations. Also, the PANS $f_k = 0.1$ simulation is able to detect an unsteadiness

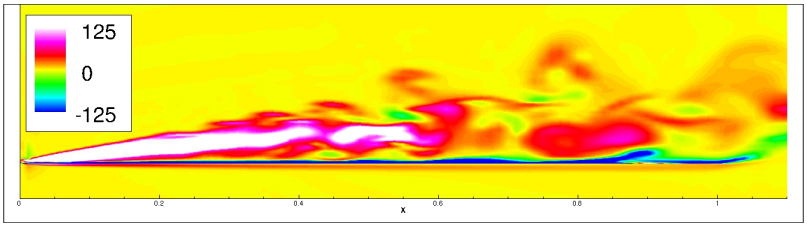

(a) URANS

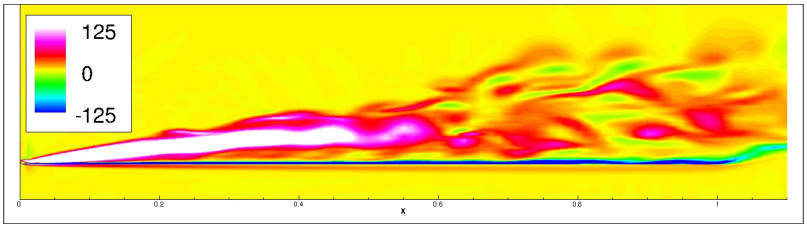

(b) PANS $f_k = 0.5$

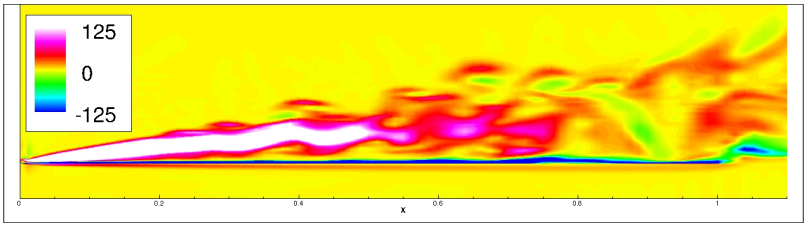

(c) PANS $f_k = 0.1$

(d) DNS X-Vorticity [13]

Figure 4.10: Instantaneous Axial Vorticity through Vortex Core; $\alpha = 15^o$; $Re = 26,000$

in the core of the primary vortex which is not seen in the URANS or PANS $f_k = 0.5$ simulations.

The individual components of the vorticity vector (x-vorticity, y-vorticity, and z-vorticity) on a vertical slice through the core of the primary vortex are shown as contour plots in Fig. 4.11. The x-vorticity component is shown in the first row of figures, the y-vorticity component is shown in the middle row of figures, and the

z-vorticity component is shown in the lower row of figures. It is clear the x-vorticity

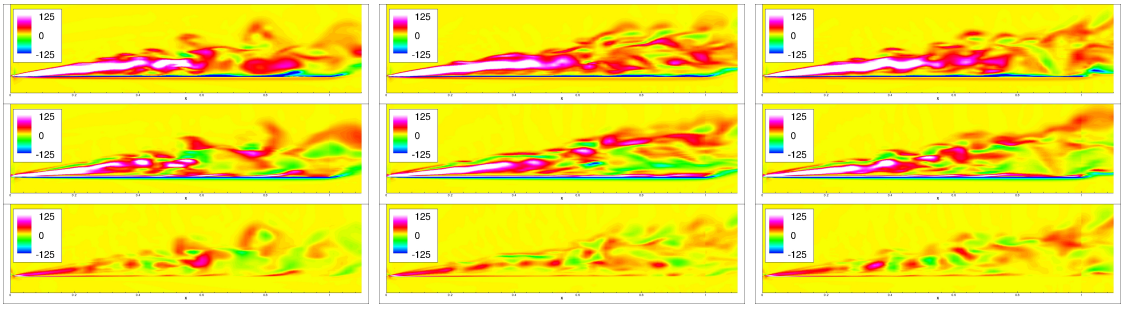

(a) URANS (b) PANS $f_k = 0.5$ (c) PANS $f_k = 0.1$

Figure 4.11: Instantaneous Vortex Core Vorticity Vector Components; $\alpha = 15^o$; $Re = 26,000$

is the dominant component in the core of the primary vortex. The y-vorticity and z-vorticity components are not as intense as the x-vorticity component for any of the simulations. We can also see a clear increase in the small scale structure with a reduction in f_k. In addition, the f_k reduction allows for more scales of motion to be liberated in the y and z directions. This is similar to previous studies of circular cylinder flow where a URANS simulation will lock the vorticity into its dominant direction instead of allowing it to be exchanged to other components [26]. The PANS simulations allow for this reorientation of vorticity.

The mean flow streamlines and pressure coefficient contours on the upper surface of the wing are shown in Fig. 4.12. The DNS results of Gordnier and Visbal [13] are presented in Fig. 4.12c while the present URANS simulation result is shown in Fig. 4.12a and the PANS $f_k = 0.1$ simulation results are given in Fig. 4.12b. The flow is from left to right, and the lower edge of the figures represents the symmetry plane of the simulation. The structure of the vortex system can be visualized by in-

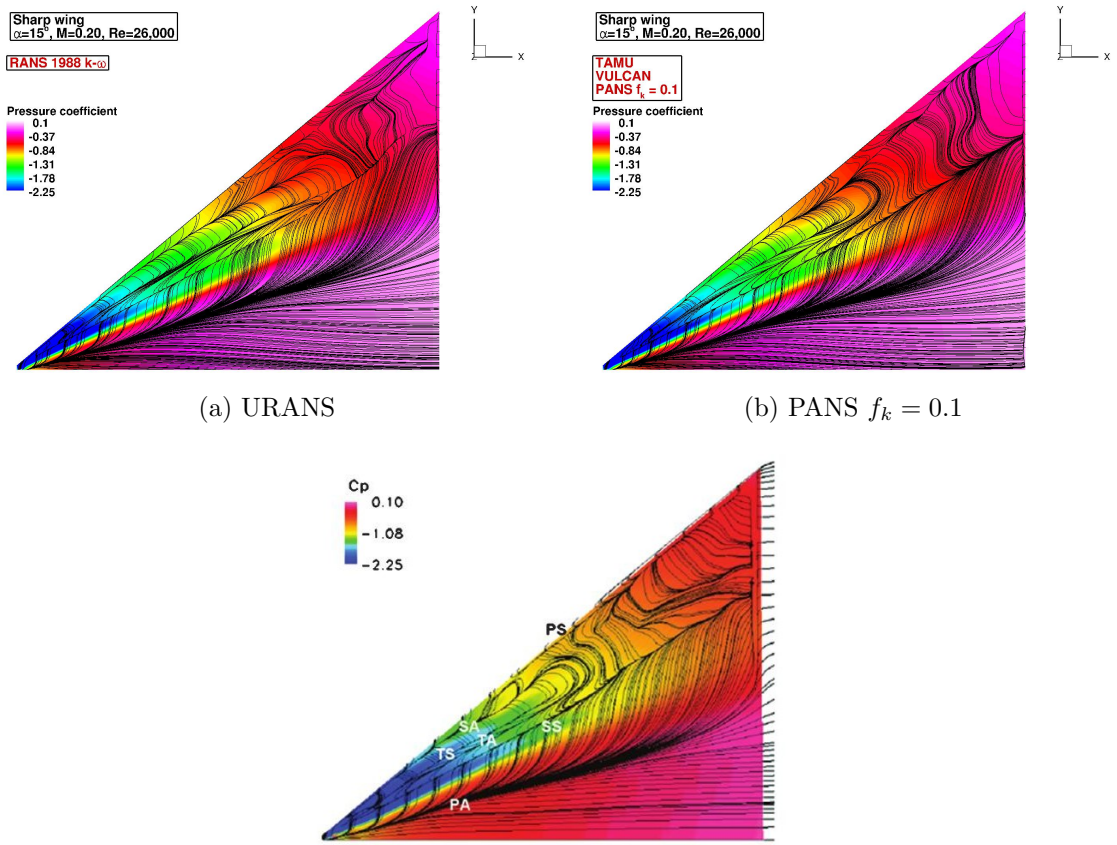

(a) URANS

(b) PANS $f_k = 0.1$

(c) DNS [13]

Figure 4.12: Mean Surface C_p with Streamlines; $\alpha = 15^o$; $Re = 26,000$

specting the surface streamlines. The locations of primary separation (PS), primary attachment (PA), secondary separation (SS), secondary attachment (SA), tertiary separation (TA), and tertiary attachment (TA) are labeled in Fig. 4.12c. The primary vortex separates along the length of the leading edge and rolls upwards, then inwards towards the symmetry plane, and finally down to the upper surface of the wing where it reattaches. This primary attachment line is visualized by the prominent cluster of surface streamlines. Once reattached, the flow is drawn outwards by the suction from the primary vortex. Once the streamlines pass the vortex centerline,

they encounter an adverse pressure gradient and separate into a secondary vortex underneath the primary vortex. These secondary separation and reattachment lines are also labeled in Fig. 4.12c. Once the secondary vortex has reattached, the flow is drawn inwards towards the wing centerline by the presence of the secondary vortex. However, once the flow traverses the centerline of the secondary vortex another adverse pressure gradient is encountered causing a small tertiary separation and subsequent reattachment. Vortex breakdown occurs approximately where the TS and TA lines make an abrupt turn. The URANS simulation maintains its well-defined separation and attachment lines much further aft than the DNS simulation, whereas the PANS $f_k = 0.1$ simulation predicts a degradation of the separation and attachment lines in locations similar to the DNS.

To add a quantitative component to the streamline patterns, we show the locations of the primary attachment, secondary separation, and secondary attachment lines as angles measure from the horizontal wing centerline in Tab. 4.2. Overall,

Table 4.2: Locations of Vortex Separation and Attachment; $\alpha = 15^o$; $Re = 26,000$

Case	PA	SS	SA
URANS	17.1^o	27.8^o	38.4^o
PANS $f_k = 0.1$	16.5^o	27.2^o	38.0^o
DNS	14.9^o	27.3^o	38.7^o

there is very little difference between the simulations. However, the PANS $f_k = 0.1$ results are in slightly better agreement with the DNS results compared to the URANS simulation.

The velocity magnitude through the vortex core is shown in Fig. 4.13 compared

with the DNS data of Visbal [13]. The results in Fig. 4.13 are obtained by taking data along a straight line along the centerline of the vortex core. The URANS

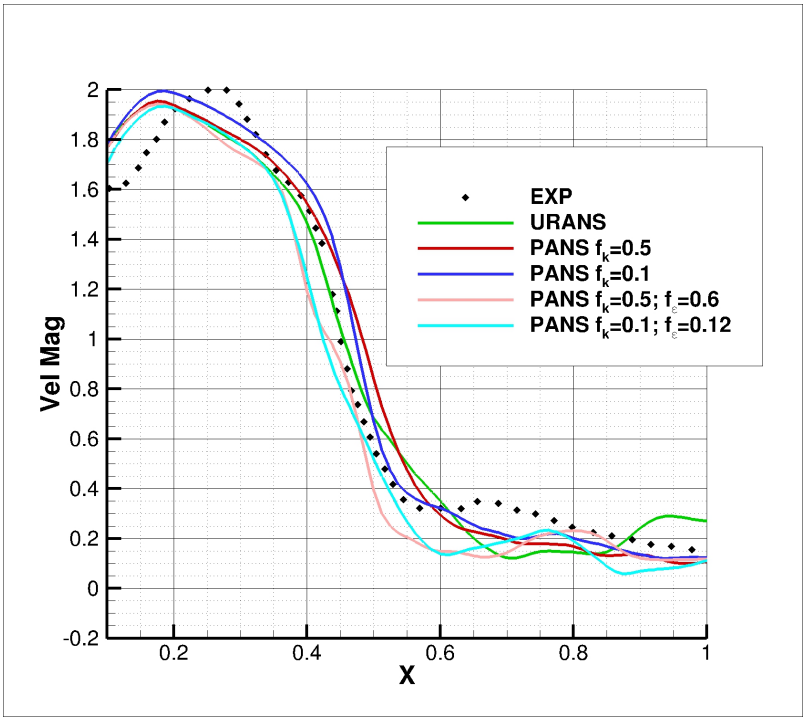

Figure 4.13: Mean Velocity through the Vortex Core; $\alpha = 15^o$; $Re = 26,000$

and PANS simulations are all able to capture the mean velocity magnitude to a reasonable degree. It is well established that the strong primary vortex acts in a jet-like manner accelerating the flow up until vortex breakdown where the vortex acts in a wake-like manner decelerating the flow. This trend is captured by the present simulations. The location of vortex breakdown correlates with the velocity peak, and the present simulations predict an early vortex breakdown compared to the DNS. As the primary vortex undergoes breakdown, the PANS simulations are able to more faithfully predict the deceleration of the mean velocity while the URANS simulation

predicts a more gradual vortex breakdown. The reduced f_ε PANS simulation results in Fig. 4.13 will be discussed in the following section which pertains to the effects of reduced f_ε.

4.5.3 Effects of Low Reynolds Number on Resolution Specification

Following the initial PANS simulations, we performed reduced f_ε PANS simulations at $f_k = 0.5$, $f_\varepsilon = 0.6$, and $f_k = 0.1$, $f_\varepsilon = 0.12$. Is was established by Reyes [43] that low Reynolds number PANS simulations require a reduction in f_ε concurrent with the reduction in f_k. Due to the narrow turbulence spectrum of the low Reynolds number flow, the low f_k PANS simulations set a spectral cut-off in the dissipative scales. Therefore, to appropriately model the dissipation of the flow, a reduction in f_ε is required. This section will identify the flow features and statistics which are sensitive to such a reduction in f_ε.

The reduced f_ε results which are shown in Fig. 4.13 are noticeably different than the other PANS and URANS results. The reduced f_ε simulations predict a similar peak velocity in the vortex core, however they do predict a slightly earlier vortex breakdown. During the velocity deceleration as the vortex breaks down, the reduced f_ε simulations tend to track the rate of deceleration more accurately than the other results.

Verhaagen [6] experimentally investigated various delta wing geometries at several Reynolds numbers and angles of attack. The results for the lift coefficient at $\alpha = 15^o$ as a function of Reynolds number are shown in Fig. 4.14 with the present data added to the data of Verhaagen. The lift coefficient is a very weak function of Reynolds number, only varying slightly over a wide range of Reynolds number. However, there is a clear trend of decreasing lift as Reynolds number is decreased. Unfortunately, we cannot directly compare our $Re = 26,000$ results to the data because the lowest

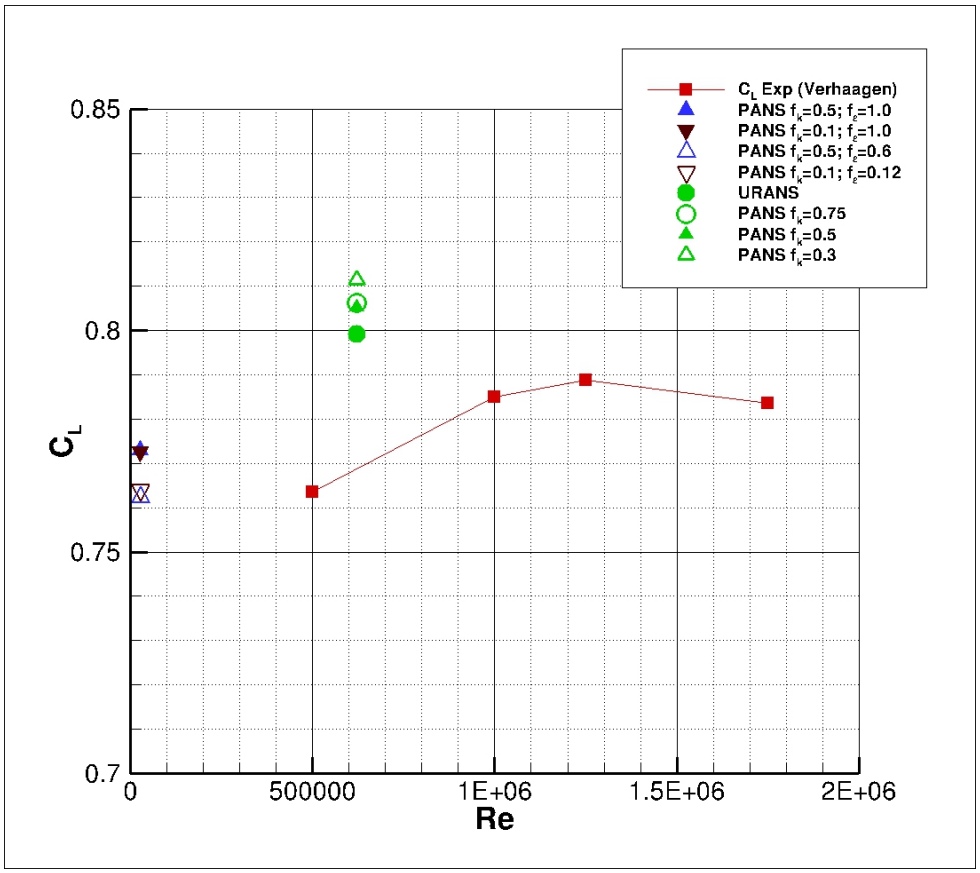

Figure 4.14: C_L as a Function of Reynolds Number; $\alpha = 15^o$

Reynolds number presented in the data is $Re = 500,000$. Nevertheless, we present the lift coefficient for our simulations along-side the available data. The $Re = 26,000$ PANS simulations all predict a lift coefficient which is commensurate with the data. There is a noticeable reduction in lift coefficient with the reduced f_ε simulations. It is difficult to definitively say that the reduced f_ε simulations provide a more accurate prediction of lift because there is no data at $Re = 26,000$, but the reduced f_ε simulation results are more in-line with the trend of a reduced lift coefficient at low Reynolds number. The $Re = 620,000$ lift coefficient results will be discussed in the following section.

Another flow feature which is more accurately captured with reduced f_ε is the instantaneous vorticity shown in Fig. 4.15. The PANS $f_k = 0.1$ $f_\varepsilon = 1.0$ result is shown in Fig. 4.15a, the PANS $f_k = 0.1$ $f_\varepsilon = 0.12$ result is shown in Fig. 4.15b, and the DNS result of [13] is shown in Fig. 4.15c. We previously discussed that neither

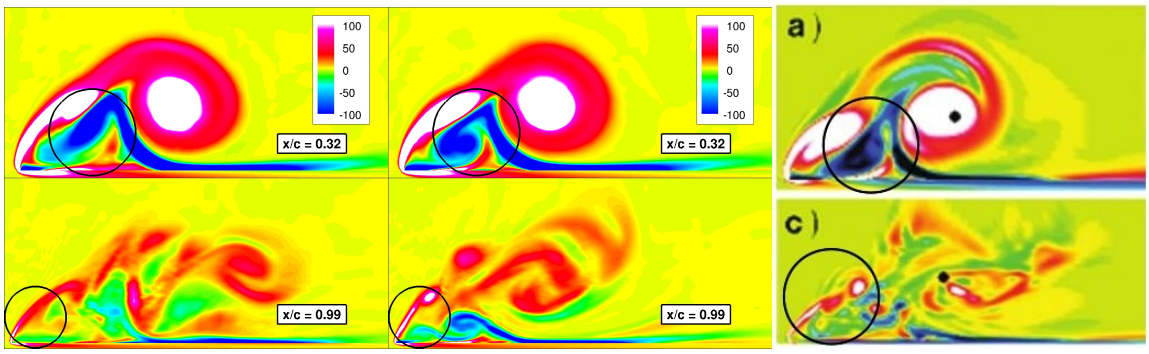

(a) PANS $f_k = 0.1$; $f_\varepsilon = 1.0$ (b) PANS $f_k = 0.1$; $f_\varepsilon = 0.12$ (c) DNS [13]

Figure 4.15: Instantaneous Vorticity Contours $x/c = 0.32$ and $x/c = 0.99$; $\alpha = 15^o$; $Re = 26,000$

the URANS nor PANS simulations were able to predict the intensity of the secondary vortex. However, the reduced f_ε simulation is able to more accurately predict the intensity and the structure of the secondary vortex at $x/c = 0.32$. In addition, the reduced f_ε simulation more accurately predicts the intensity of the vorticity in the separated shear layer, especially in the aft portion of the wing at $x/c = 0.99$.

4.5.4 Summary of Low Reynolds Number Findings

The results presented in the previous sections show that the majority of the vortical flow features can be accurately captured with either a URANS or PANS simulation for this low Reynolds number case. This section briefly lists the specific

Table 4.3: Summary of Flow Features at Variable Resolutions; $Re = 26,000$

URANS or PANS	Increase Resolution	Modify Dissipation
Location of vortex core	Instantaneous vorticity	Vortex interactions
Location of PA line	Streamline patterns	Shear layer vorticity
Mean vorticity	Vortex core deceleration	
Vortex core velocity		
Surface C_p, $x/c < 0.6$		

features, and the resolution which is required to resolve them in Tab. 4.3. For the low Reynolds number case, the disparity between the largest and smallest turbulent scales is small. Therefore the disparity between the URANS and PANS simulations is not as profound as the subsequent high Reynolds number case. As the Reynolds number is increased we expect the ratio of largest-to-smallest scales to increase dramatically, and thus more differences between URANS and PANS will emerge.

4.6 PANS Simulation Results at High Reynolds Number

This section presents results for the same sharp leading edge delta wing geometry presented in the previous section, but at $Re = 620,000$. The simulations are performed at $\alpha = 15^o$ and $\alpha = 23^o$. Comparisons are made against the ILES simulations of Gordnier et al [16] who performed simulations of a 50^o sweep sharp leading edge delta wing at $Re = 620,000$ and $\alpha = 15^o$ using a 35M-cell grid. Although there is not data available at $\alpha = 23^o$, PANS simulation results for that angle of attack are presented here to highlight the ability of the PANS model to resolve more unsteady structures. At $\alpha = 23^o$ the delta wing is very near stall, and this investigation will emphasize that this is a flight condition which warrants further detailed study.

In order to perform the simulations at this increased Reynolds number, the 4.48M-cell grid from the previous section was refined near the wall to achieve $y+ \sim O(1)$.

The number of total cells remained constant; the grid was simply compressed in this near-wall region to provide adequate resolution. As a result of this refinement, the $y+$ values were below unity for the majority of the upper surface of the wing. The small region near the wing apex is the only location where $y+$ exceeded unity.

4.6.1 $\alpha = 15^o$ Results

As in the previous low Reynolds number case, we begin with a preliminary URANS simulation which allows for an analysis of the levels of turbulence in the flow. Figure 4.16 shows contours of the ratio of largest-to-smallest length scale for the high Reynolds number URANS simulation at $\alpha = 15^o$. The turbulence spectrum

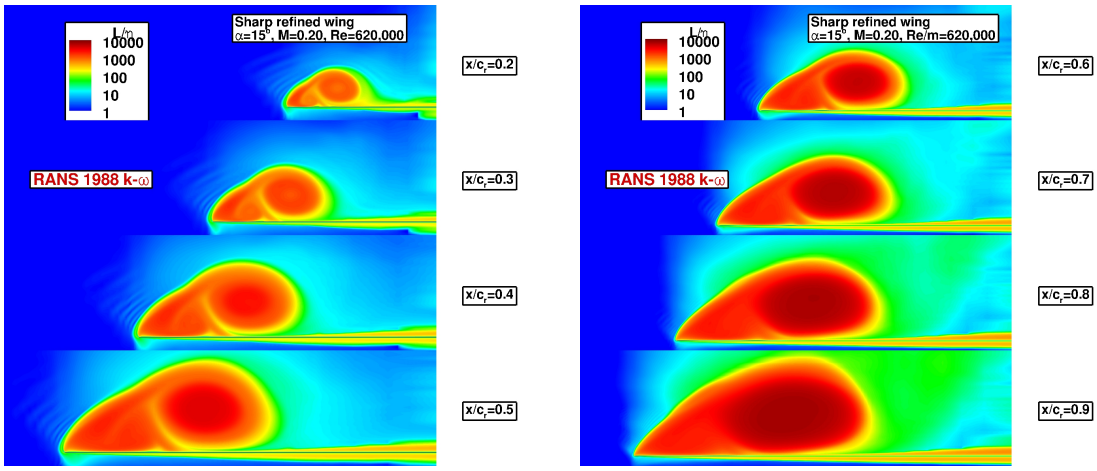

(a) Forward L/η contours (b) Aft L/η contours

Figure 4.16: URANS L/η Results; $\alpha = 15^o$; $Re = 620,000$

is clearly more broad for this high Reynolds number case. The L/η ratio is at 1,000 even near the wing apex at $x/c = 0.2$. In the aft sections of the wing, the spectrum continues to widen with L/η well over 1,000. This is in contrast to the low Reynolds

number simulations presented in the previous section where the largest values of L/η were ~ 250. Due to the well-developed, broad spectrum turbulence which is present in the vortex region for this high Reynolds number case, one would expect to see a greater disparity between the URANS and PANS simulations.

Following the URANS simulation, we perform PANS simulations at $f_k = 0.75$, $f_k = 0.5$, and $f_k = 0.3$. The lift coefficient predicted by the high Reynolds number URANS and PANS simulations are shown in Fig. 4.14. The lift coefficient is consistently over-predicted compared to the experimental data of Verhaagen [6]. In addition, one would expect to see a progressive improvement in the prediction as f_k is reduced from 1.0 in the URANS simulaion down to 0.75, 0.5, and 0.3 in the PANS simulations. In fact, the exact opposite trend is observed: the lift coefficient diverges from the experimental data with decreasing f_k. The reason for the poor lift coefficient performance is likely due to the grid used for these simulations.

We present the results for the mean axial vorticity at $x/c = 0.2$ in Fig. 4.17. The results for our URANS and PANS simulations are given in Figs. 4.17a, 4.17b, 4.17c, and 4.17d, while Fig. 4.17e shows the result from the corresponding ILES simulation and PIV experimental data. It must be noted that the results for the URANS and PANS simulations are use a non-dimensional x-vorticity scale which ranges from -600 to 600. In Gordnier et al [16] Fig. 4.17e is presented with an x-vorticity scale ranging from -250 to 250. However, given the levels of vorticity which are seen at $x/c = 0.175$ shown in Fig. 4.19, we believe that the -600 to 600 scale is more appropriate. The mean vorticity for all of the URANS and PANS simulations are in agreement with the ILES and PIV data. A strong primary and secondary vortex can be seen in all simulations at this location.

The mean surface streamlines are shown with contours of surface pressure coefficient in Fig. 4.18. The URANS and PANS $f_k = 0.75$ and $f_k = 0.3$ simulation

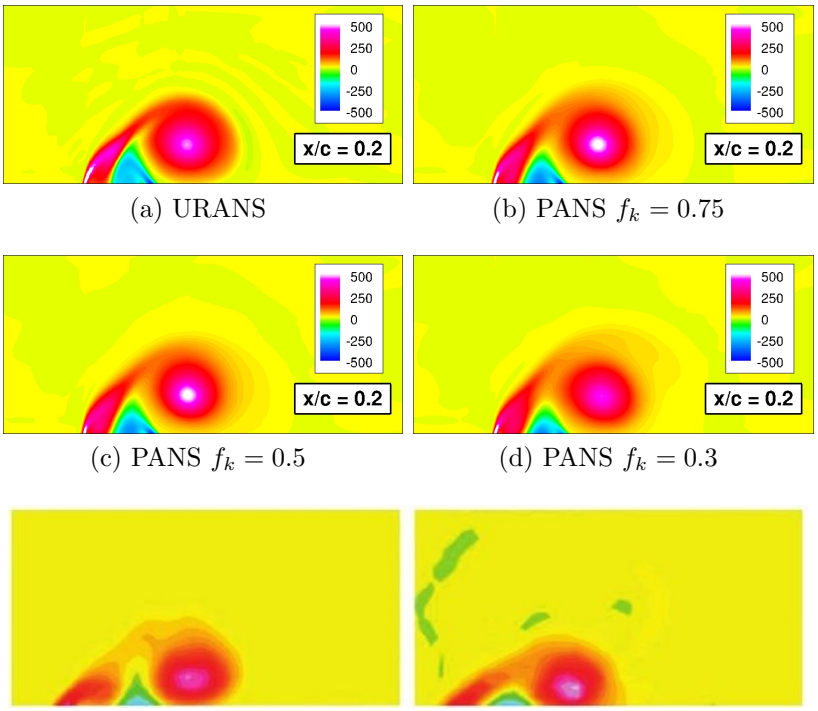

(a) URANS (b) PANS $f_k = 0.75$

(c) PANS $f_k = 0.5$ (d) PANS $f_k = 0.3$

(e) ILES and PIV [16]

Figure 4.17: Mean Axial Vorticity at $x/c = 0.2$; $\alpha = 15^o$; $Re = 620,000$

results are given in Figs. 4.18a, 4.18b, and 4.18c respectively. These simulations are compared against the streamline and pressure coefficient plot from the ILES simulation given in Fig. 4.18d. The qualitative agreement in pressure coefficient is good. The comparison of the surface streamlines is more varied. In the ILES result in Fig. 4.18d, this is a summary of the streamline features which can be seen and which we would expect our model to capture:

1. Primary attachment line: well defined

2. Secondary separation line: indistinct, tends to bend outboard, washed out in aft regions

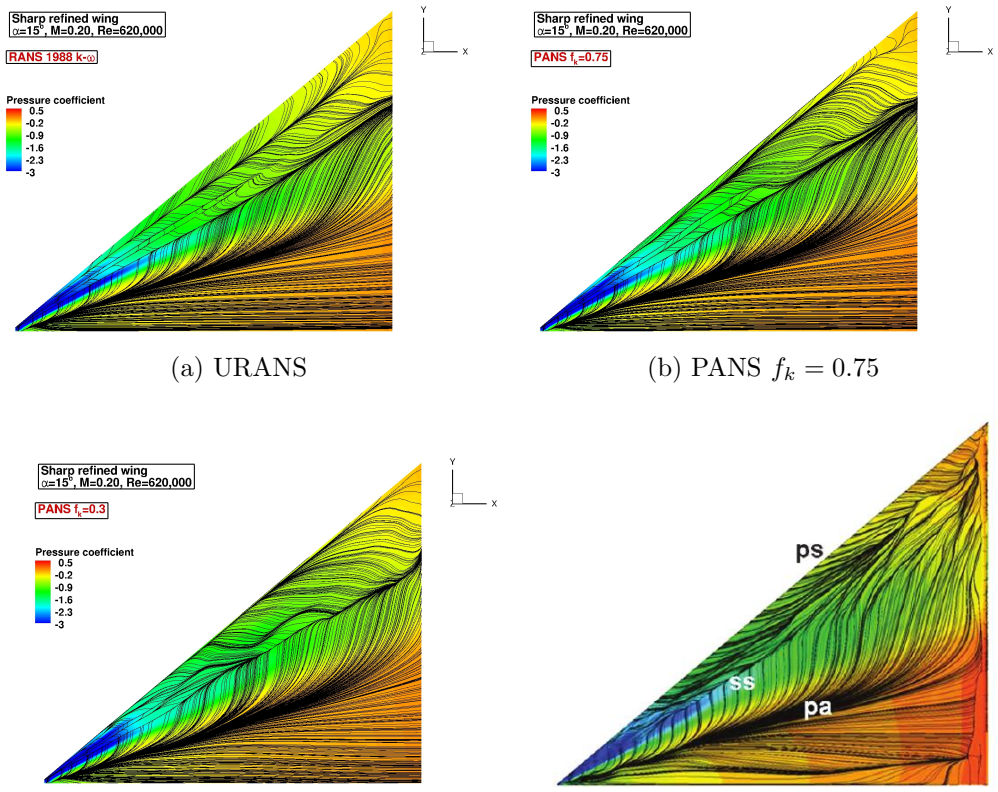

(a) URANS

(b) PANS $f_k = 0.75$

(c) PANS $f_k = 0.3$

(d) ILES [16]

Figure 4.18: Mean Surface Streamlines and Surface C_p; $\alpha = 15^o$; $Re = 620,000$

3. Secondary attachment line: not present

4. Tertiary separation and tertiary attachment lines: very faint or not present

The URANS simulation achieves only item 1. For items 2, 3, and 4, on the other hand, URANS shows well-defined and very straight lines of SS, SA, TS, and TA. The $f_k = 0.75$ result in Fig. 4.18b achieves item 1 and shows improvement on item 2, with the SS and SA lines bending outboard slightly. However, the $f_k = 0.75$ simulation also shows secondary and tertiary separation and attachment lines which are clearly more pronounced and distinct than the ILES result which means items 3 and 4 are

not captured. As f_k is reduced to 0.3, the simulation achieves items 1, 3, and 4. The primary attachment line is well defined, the SA line is no longer visible, the SS line clearly bends outboard, and the TS and TA lines are only faintly visible. This result is clearly in much closer agreement with the ILES result compared to the URANS or PANS $f_k = 0.75$ result. In summary, the streamline patterns progressively improve with f_k reduction.

Figure 4.19 shows contours of instantaneous axial vorticity at $x/c = 0.175$, $x/c = 0.612$, and $x/c = 0.875$. These locations are chosen for examination because of the existing vorticity data available for comparison from the ILES study of Gordnier et al [16] which is shown in Fig. 4.19d. The vorticity plots show a progressive increase in small scale structure as f_k is reduced from 1.0 in the URANS simulation to 0.3. The present simulations are unable to capture the finest structures because of the limitation of the 4.48M-cell grid compared to the 35M-cell grid used for the ILES.

Figure 4.20 shows contours of the three vorticity vector components on a vertical slice through the primary vortex core. The URANS result in Fig. 4.20a shows a very strong, dominant x-vorticity with limited fluctuations. The y-vorticity and (especially) the z-vorticity are weaker in intensity and also show limited fluctuation levels. On the other hand, as f_k is reduced to 0.5 and 0.3, as seen in Figs. 4.20b and 4.20c respectively, many more small-scale structures are visible. In addition, the dominant x-vorticity is exchanged for y-vorticity and z-vorticity.

Figure 4.21 compares only the z-component of vorticity for the URANS and PANS simulations against the ILES simulation of Gordnier et al [16]. There is clearly a progressive increase in small scale structure as f_k is reduced, and the vorticity structure appears to approach the levels seen in the ILES result. The PANS simulations are limited in their ability to resolve structure, however, due to the 4.48M-cell grid compared to the 35M-cell ILES grid. However, it is clear that if one is interested

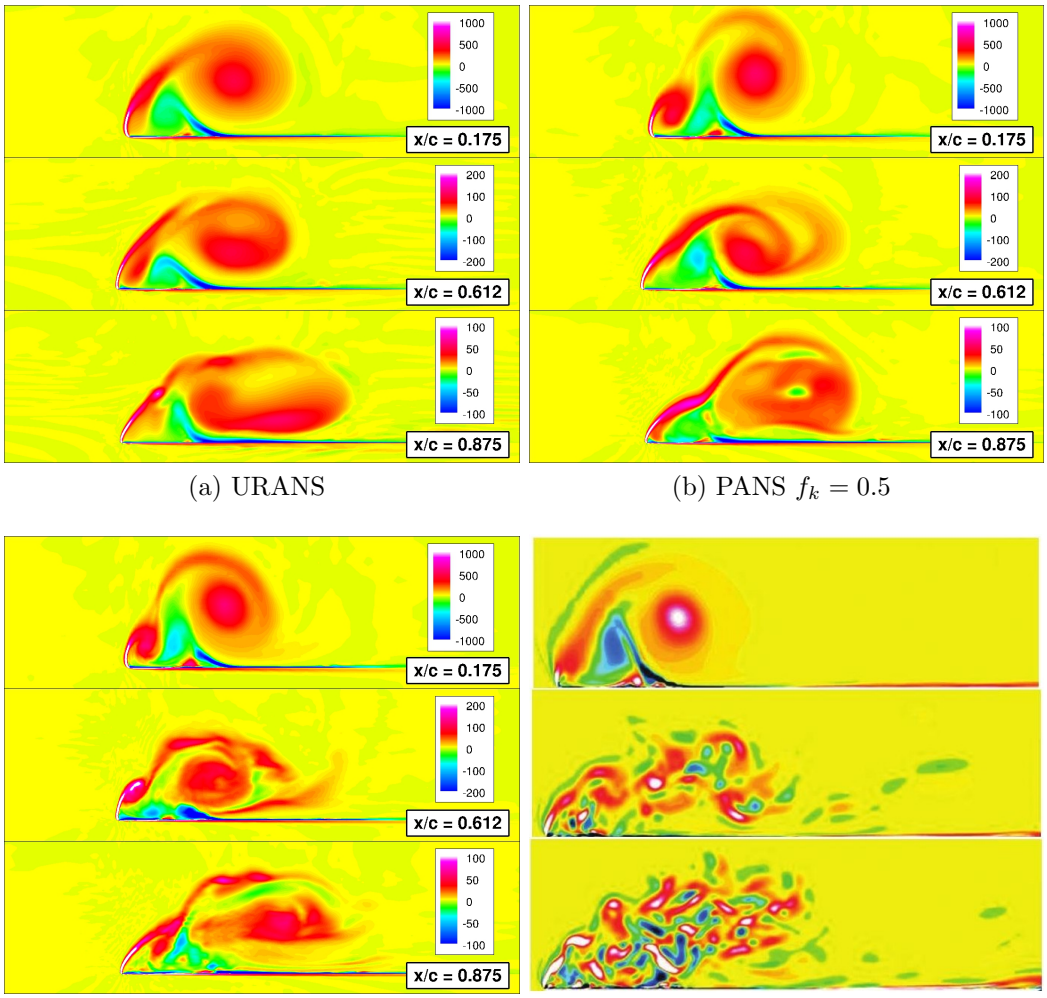

(a) URANS (b) PANS $f_k = 0.5$

(c) PANS $f_k = 0.3$ (d) ILES [16]

Figure 4.19: Instantaneous Axial Vorticity at $x/c = 0.175$, $x/c = 0.612$, and $x/c = 0.875$; $\alpha = 15^o$; $Re = 620,000$

in resolving the smallest structures that a given grid can support, then a PANS simulation can provide those structures more readily than a URANS simulation.

4.6.2 $\alpha = 23^o$ Results

This section presents results for the same sharp leading edge delta wing at $Re = 620,000$ and $\alpha = 23^o$. This angle of attack is chosen because it is at a near-stall

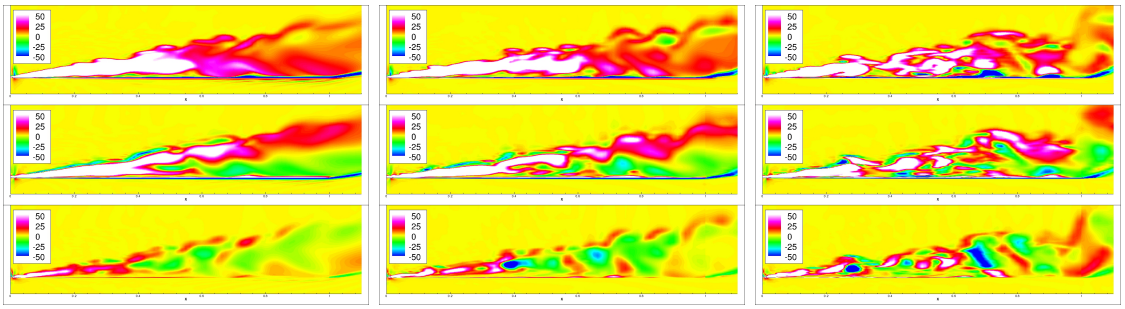

(a) URANS (b) PANS $f_k = 0.5$ (c) PANS $f_k = 0.3$

Figure 4.20: Instantaneous Axial Vorticity through Vortex Core; $\alpha = 15^o$; $Re = 620,000$

condition and presents a complex, unsteady, vortical flow field where the PANS model can be exercised. After an initial URANS simulation, PANS simulations are performed at $f_k = 0.5$, 0.3, and 0.2. Figure 4.22 shows the ratio of L/η contours for the $\alpha = 23^o$ case. The results are similar to the $\alpha = 15^o$ in that there is broad spectrum turbulence throughout the entire chord of the wing. Clearly, the turbulence levels are high enough at this Reynolds number and angle of attack to warrant a reduced f_k PANS simulation.

The instantaneous axial vorticity contours for the URANS and PANS simulations are shown in Fig. 4.23. The contours are shown at the same locations and using the same contour coloring scale as the $\alpha = 15^o$ case, although there is no experimental, or computational data for comparison at this near-stall angle of attack. The first observation to be made about the instantaneous vorticity contours is the progressive increase in small scale structure which is seen with a decrease in f_k. The URANS result in Fig. 4.23a shows so little flow structure that it appears to be a time-averaged result. As f_k is reduced to 0.5, 0.3, and 0.2 in Fig. 4.23b, 4.23c, and 4.23d, respectively, the small scale turbulence structures are liberated. Next, the intensity

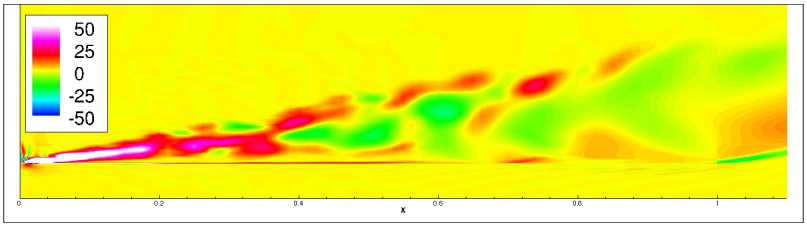

(a) URANS

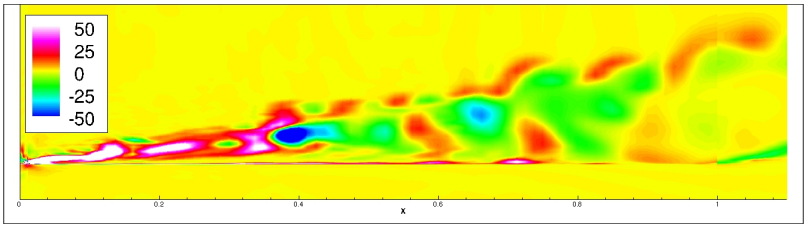

(b) PANS $f_k = 0.5$

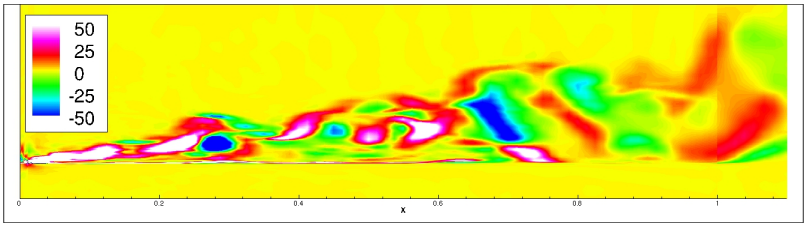

(c) PANS $f_k = 0.3$

(d) ILES Z-Vorticity [16]

Figure 4.21: Instantaneous Azimuthal Vorticity through Vortex Core; $\alpha = 15^o$; $Re = 620,000$

of the primary vortex is clearly weaker for this $\alpha = 23^o$ case as compared to the $\alpha = 15^o$ in Fig. 4.19. It is well-known that the intensity of the vortex increases with increasing angle of attack. However, this appears to be true only up until stall. At near-stall incidence angles the well-defined vortex structure is lost and the flow on

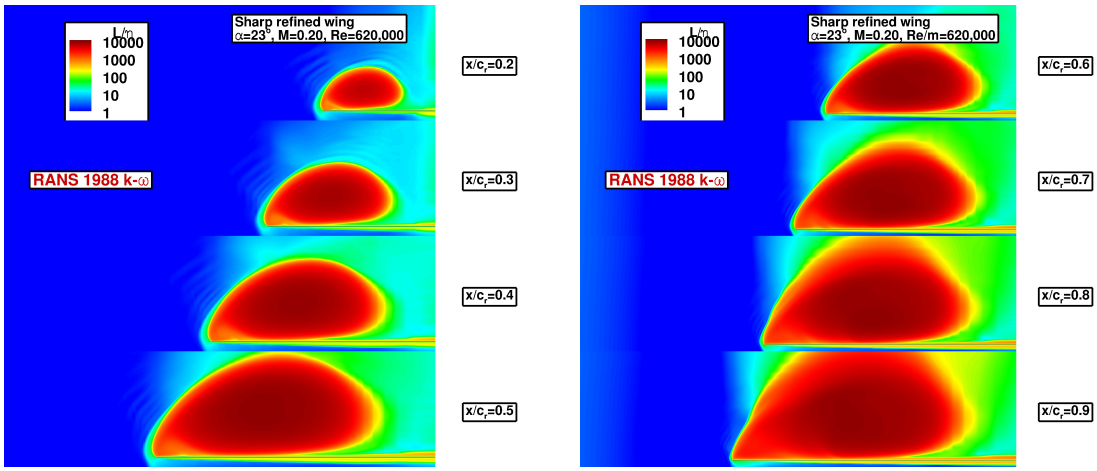

(a) Forward L/η contours

(b) Aft L/η contours

Figure 4.22: URANS L/η Results; $\alpha = 23^o$; $Re = 620,000$

the upper surface of the wing resembles a more generic separated flow.

Figure 4.24 shows contours of the three vorticity vector components on a vertical slice through the core of the primary vortex. The dominant component is clearly the x-vorticity component. The URANS simulation in Fig. 4.24a shows some large scale fluctuations in the vorticity components, but the majority of the vorticity remains in the x-component. However, as f_k is reduced to 0.5 and 0.2 in Fig. 4.24b and 4.24c respectively, more small scale fluctuations are pesent and the dominant x-vorticity is exchanged for y-vorticity and z-vorticity. This is a better reflection of the true flow structure seen in the literature.

4.6.3 Summary of High Reynolds Number Findings

At high Reynolds number, there is no experimental or DNS data for comparison so we have made comparisons with ILES data where available. We now compile a list of the specific features for the high Reynolds number case and resolution which is required to resolve them in Tab. 4.4. For the high Reynolds number case, the dis-

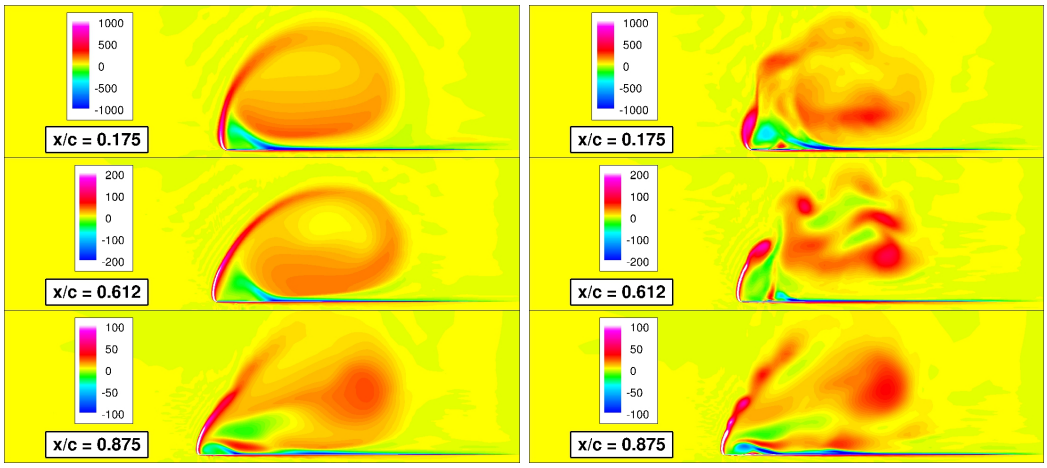

(a) URANS

(b) PANS $f_k = 0.5$

(c) PANS $f_k = 0.3$

(d) PANS $f_k = 0.2$

Figure 4.23: Instantaneous Axial Vorticity at $x/c = 0.175$, $x/c = 0.612$, and $x/c = 0.875$; $\alpha = 23^o$; $Re = 620,000$

parity between the largest and smallest scales is much greater than the low Reynolds number case. Due to this, the disparity between a URANS and PANS simulation is much more pronounced.

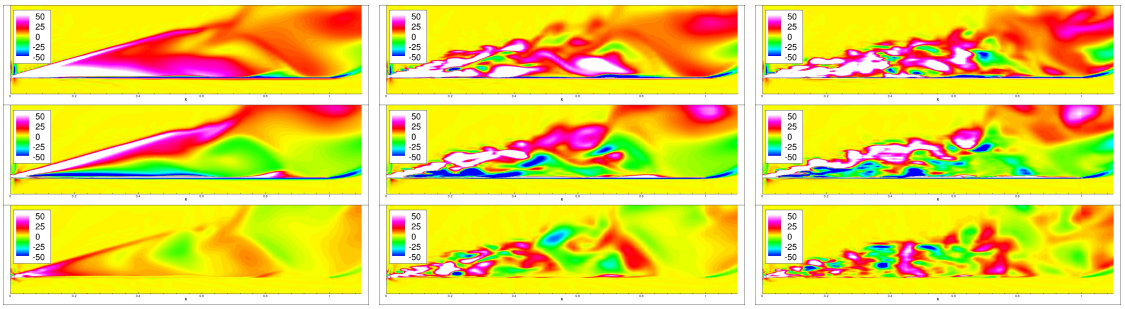

(a) URANS (b) PANS $f_k = 0.5$ (c) PANS $f_k = 0.2$

Figure 4.24: Instantaneous Axial Vorticity through Vortex Core; $\alpha = 23^o$; $Re = 620,000$

Table 4.4: Summary of Flow Features at Variable Resolutions; $Re = 620,000$

URANS or PANS	Increase Resolution
Mean vorticity structure	Instantaneous vorticity structure All separation and attachment lines

4.7 Conclusions

This study has explored the utility of the PANS turbulence model in capturing the pertinent flow physics of a delta wing flow at wide ranges of angles of attack and Reynolds number. The findings of this study are summarized here.

In the low Reynolds number case, given a grid which we know is adequate for high resolution at that Reynolds number, the laminar flow features can be captured by any model. These flow features include the locations of the vortex core, the separation and reattachment lines, and the C_p upstream of vortex breakdown. The turbulent features after breakdown such as the aft C_p and vortex structure are dependent upon the model. The lift coefficient, which is derived from the entire surface C_p appears

to also be influenced by the choice of the model. Overall, the differences between URANS and PANS simulations are few due to the narrow turbulence spectrum and the lack of disparity between the largest and smallest turbulence scales.

In the high Reynolds number case, given a grid which we know is not adequate for high resolution at that Reynolds number, one cannot expect an accurate C_L prediction and an increased resolution PANS simulation does not improve the computation of lift coefficient. If one is interested in unsteady features after breakdown (for purposes of flow buffet, or unsteady aerodynamics) a PANS simulation is required. The flow structures are limited by the grid resolution, but PANS will maximize the utility of a given grid in resolving flow structures. The primay vortex location is such a dominant flow feature that it may be independent of model or grid resolution. The $\alpha = 23^o$ near-stall case showed tremendous unsteadiness and is an excellent example of a condition where PANS is most useful at resolving the unsteadiness. The levels of turbulence seen in the L/η contours are considerably higher than the $\alpha = 15^o$ case. Vortex breakdown occurs within the first 15% of the wing at $\alpha = 23^o$ therefore the vast majority of the flow is dominated by unsteady, broken down vortices. The lift coefficient is dependent upon the model, but also upon the grid resolution. At high Re, the lift coefficient is poorly predicted. Lift coefficient requires a converged grid. The high Reynolds number case lacks a thorough experimental and/or highly resolved computational data set for benchmark quantitative comparisons. Future work should be carried out towards this goal.

5. VARIABLE RESOLUTION SIMULATIONS OF ROUND LEADING EDGE DELTA WINGS

5.1 Introduction

Delta and diamond wings with moderate sweep angles of about 50^o are ideally suited for application in unmanned combat aerial vehicles (UCAVs). A UCAV is expected to operate in a wide flight envelope spanning a large range of angles of attack and Reynolds number. The delta and diamond wing are useful because at extreme angles of attack which would be past the point of stall for many wings, the delta and diamond wing are able to maintain their lift and stability without the use of flow control devices. While sharp leading edge wings and airfoils lend themselves to easier computational analysis, structural and manufacturing considerations dictate a modest yet discernible leading edge radius. When leading edge curvature is introduced on a delta wing, forebody separation becomes significantly more complex to simulate and analyze.

The round leading edge delta wing geometry also appears in many flows in nature. For example, Johansson and Norberg [24] studied how aquatic birds generate propulsion with their delta-wing-like webbed feet. Their results shown in Fig. 5.1a indicate that as the bird pushes its feet through the power stroke, the water flows around the foot at an angle of attack well over 100^o and the propulsion is generated from drag. However, after this initial period, the angle of attack decreases to approximately 30^o and the final 60% of the propulsive force is generated from separation-induced vortex lift. Johansson and Norberg [24] also show flow visualization of a semi-slender delta wing with a geometry similar to the webbed foot of the bird. The visualization shown in Fig. 5.1b clearly shows the familiar vortical flow. The vortical flow produced from

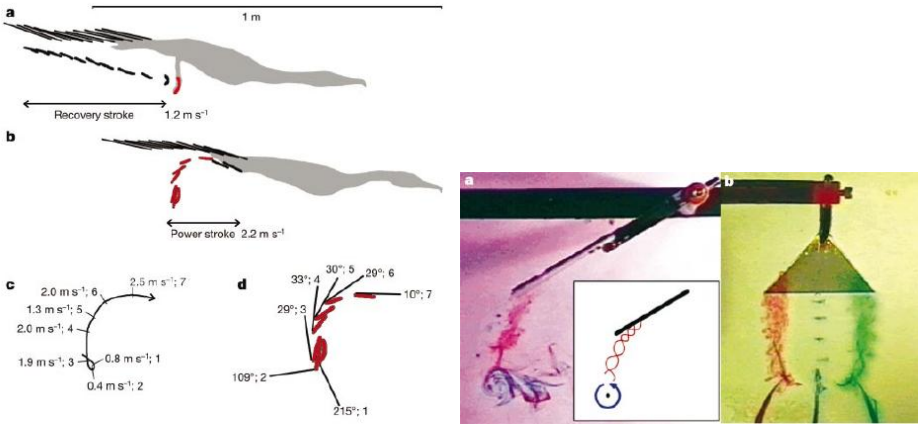

(a) A bird pushing its foot through the power stroke

(b) Vortical flow visualization

Figure 5.1: Vortical Flow Generated by an Aquatic Bird (Reprinted by permission from Macmillan Publishers Ltd: *Nature, 424(6944):6568* [24] copyright 2003)

these swimming birds is more like the vortical flow over the rounded leading edge wings of modern UCAVs than the sharp leading edge flows which have been studied extensively. It is very likely that the flow characteristics show a similar sensitivity to leading edge radius, leading edge sweep, and Reynolds number.

5.1.1 Brief Literature Survey

There have been computational and experimental studies performed on delta wings with various leading edge sweep angles and leading edge curvature. The earliest studies analyzed delta wings with with large ($> 60^o$) leading edge sweep angles and sharp leading edges [41] [20] [29] [46]. Some of the recent literature which focuses on the round leading edge delta wing comes from [50] and [42]. Luckring [32] has performed a side-by-side comparison of a sharp leading edge delta wing and a round leading edge delta wing with 65^o sweep. However, such a side-by-side comparison of a moderately swept delta wing is lacking attention in the literature.

In Section 4 we provide results for a 50^o swept, sharp leading edge, flat plate delta wing at $Re = 620,000$. Previous work has also been performed in Section 2 simulating the 53^o swept, blunt leading edge, NACA64A006 diamond wing which was used for the NATO AVT-183 working group study at $Re = 3,000,000$.

5.1.2 Flow Physics and Features

For delta wings with sharp leading edges, the vortex will always separate at the sharp leading edge, beginning at the wing apex. This is not the case for round leading edge delta wings; the separation point is dependent upon many factors including Reynolds number and angle of attack. Once separated, a shear layer is created where the fast-moving freestream interfaces with the slow-moving fluid on the suction side of the wing. The shear layer rolls up into a distinct primary vortex and is drawn towards the wing centerline and then down towards the surface of the wing where it reattaches. The intensity of the vortex is highest near the apex of the wing. The tightly-wound vortex behaves like a jet flow, accelerating fluid through its core creating a potent suction on the upper surface of the wing. Beneath the primary vortex, a secondary vortex may form from the separation of the reattached primary vortex boundary layer. In some cases, a tertiary vortex forms beneath the secondary vortex. As the vortical structure convects downstream, the interaction of the vortices with the freestream and with one another causes instabilities to develop. At a sufficient distance downstream, these instabilities casue the streamwise vortex system to break down into a complex unsteady flow strucutre with vorticity aligned in all three coordinate directions.

Hummel [21] provides a schematic in Fig. 5.2 which details the effect that Reynolds number plays in the formation of the primary vortex over slender wings with rounded leading edges. At sufficiently low Reynolds number, there is a region

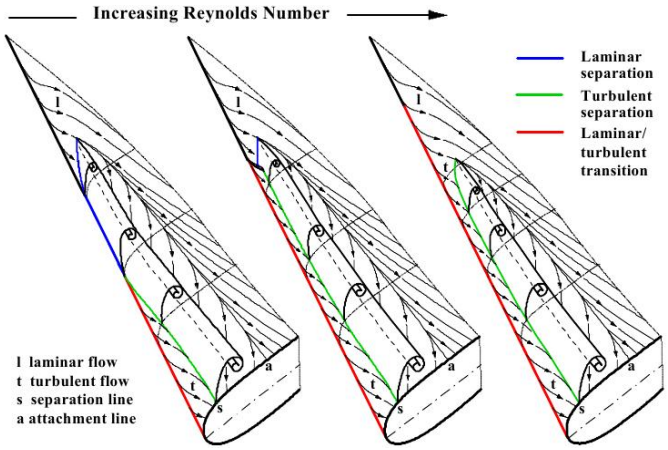

Figure 5.2: Effect of Reynolds Number on Vortex Formation for Round Leading Edge Delta Wings (Reprinted with permission from: Dietrich Hummel. "Effects of Boundary Layer Formation on the Vortical Flow Above Slender Delta Wings." Number RTO-MP-AVT-111 in RTO AVT Specialists Meeting on Enhancement of NATO Military Flight Vehicle Performance by Management of Interacting Boundary Layer Transition and Separation, Prague, Czech Republic, 2004. [21])

near the wing apex which remains laminar. The flow then undergoes a laminar separation to form the start of the primary vortex. Further aft, the flow transitions to turbulent at the leading edge. Once turbulent, the flow resists immediate separation at the leading edge. There is a small outboard region of turbulent attached flow before the flow undergoes a turbulent separation. At moderate Reynolds number, the region of laminar separation diminishes or is completely eliminated. In this parameter range the separation is almost completely turbulent. Finally at high Reynolds number, the flow completely transitions to turbulence at the leading edge and the primary vortex separation is fully turbulent in nature. Furthermore, as the Reynolds number increases the point of initial separation moves aft on the wing. Clearly the Reynolds number plays a large role in determining the point of separation and type of separation which forms the primary vortex. This dependence is not present in

the sharp leading edge wings. In the sharp leading edge case, the primary separation is always fixed at the leading edge and Reynolds number has little effect on the separation. Research by Luckring [32] has investigated the effects of compressibility, Reynolds number, and leading edge radius on delta wings. An increase in Mach number tends to promote separation, while an increase in Reynolds number tends to delay separation. The round leading edge delta wing creates surface pressure distributions which are wholly unlike those created by sharp leading edge delta wings.

5.1.3 AVT-183 Delta Wing Study Group

Due to the relative lack of attention that the round leading edge delta wing has received, A NATO (North Atlantic Treaty Organization) aerodynamics study group AVT-183: *Reliable prediction of separated flow onset and progression for air and sea vehicles* has been formed to examine the aerodynamic characteristics of semi-slender rounded leading edge diamond wings. The group has established a unit problem geometry for a detailed numerical and experimental study. Section 2 has investigated this diamond wing geometry using steady-state RANS modeling. The present work utilizes the unit geometry from the AVT-183 campaign to compare against previous sharp leading edge results.

5.1.4 Objectives and Tasks

The objective of this study is to isolate and identify the differences between round and sharp leading edge delta wing flows. The impact that these differences have upon the aerodynamic performance of the wing will also be identified. Differences between the delta and diamond wing geometries will be discussed. To achieve these objectives, we simulate the 53^o-swept round leading edge AVT-183 diamond wing and the 50^o-swept sharp leading edge delta wing of Gordnier and Visbal [13]. The

simulations are performed at multiple resolutions of the turbulence spectrum using the URANS and PANS turbulence models. We will present the flow features at a high incidence angle where vortex flow is prominent ($\alpha = 15^o$) and a highly unsteady near-stall incidence ($\alpha = 23^o$) at $Re = 620,000$.

5.1.5 Outline

This paper is organized in the following manner: Section 5.2 discusses the computational methodology and turbulence models. Section 5.3 discusses the specific numerical tool, wing geometry, and test conditions. Section 5.4 presents a comparison of round and sharp leading edge delta wings at $\alpha = 15^o$ and $\alpha = 23^o$ using URANS and PANS models and comparing against existing data where available. Section 5.5 summarizes the major findings of these studies and introduces some proposed work for future studies.

5.2 Closure Models and Governing Equations

To derive the PANS model, the flow field is decomposed into a resolved an unresolved part. Next, an arbitrary filter which can commute with temporal and spatial derivatives is applied to the Navier Stokes equations. This is a general filtering approach which utilizes an arbitrary filter, in contrast with Reynolds averaging which employs either a time-average or ensemble-average. Reynolds averaging can be viewed as a sub-set of the general filtering. The details of the filtering operation can be found in Germano [9].

$$u_i = \langle u_i \rangle + u_i'; \quad p = \langle p \rangle + p'; \quad \tau\big(u_i, u_j\big) = \langle u_i u_j \rangle - \langle u_i \rangle \langle u_j \rangle \tag{5.1}$$

$$\frac{\partial \langle u_k \rangle}{\partial x_k} = 0 \tag{5.2}$$

$$\frac{\partial\langle u_i\rangle}{\partial t}+\frac{\partial\langle u_i\rangle\langle u_j\rangle}{\partial x_j}=-\frac{\partial\langle p\rangle}{\partial x_i}+2\nu\frac{\partial\langle s_{ij}\rangle}{\partial x_j}-\frac{\partial\tau\big(u_i,u_j\big)}{\partial x_j} \tag{5.3}$$

The resulting filtered equations are similar in form to the RANS equations except that the Reynolds stress term is replaced by the generalized central moment $\tau\left(u_i,u_j\right)$. The preceding equations are filter invariant, and subsequently the generalized central moment term is invariant to the type of averaging. The PANS model is in the class of hybrid turbulence models called bridging models which purports to model a user-specified portion of the turbulence energy spectrum. The resolution is determined by the filter control parameters:

$$f_k=\frac{k_u}{k};\qquad f_\varepsilon=\frac{\varepsilon_u}{\varepsilon} \tag{5.4}$$

The parameter f_k specifies the ratio of unresolved-to-total turbulence kinetic energy and it may vary smoothly between zero and unity. A value of zero for f_k specifies that none of the turbulence energy spectrum is unresolved (i.e. the entire spectrum must be resolved by the grid). A value of unity for f_k specifies that the entire spectrum is unresolved which is identical to a RANS simulation. In essence, the f_k parameter specifies the spectral cutoff for the simulation. Any value between zero and unity may be chosen by the user, provided that the grid can support the chosen level of resolution. The parameter f_ε specifies the ratio of unresolved-to-total dissipation, and it may also vary between zero and unity. The value for f_ε will be unity unless the spectral cutoff is in the dissipative scales. The present derivation will follow a $k-\omega$ paradigm, thus we also must specify the ratio of unresolved-to-total turbulence frequency:

$$f_\omega=\frac{\omega_u}{\omega}=\frac{\varepsilon_u/\left(\beta^*k_u\right)}{\varepsilon/\left(\beta^*k\right)}=\frac{f_\varepsilon}{f_k}. \tag{5.5}$$

Just as with RANS and LES modeling, one must choose an approach to model the unresolved field and provide closure to the filtered equations. In the PANS approach, we intend to resolve the scales which are dynamically important, but still model significantly more scales than a typical LES. Because the spectral cutoff will be in the inertial range, the sub-filter closure model must be more sophisticated than the usual one-equaion model employed with a typical LES. We choose to use a Boussinesq-like two-equation closure approach for the PANS unresolved field due to the robustness of existing two-equation closures.

$$\tau\left(u_i, u_j\right) = -\nu_u \left(\frac{\partial \langle u_i \rangle}{\partial x_j} + \frac{\partial \langle u_j \rangle}{\partial x_i} \right) + \frac{2}{3} k_u \delta_{ij}; \quad \nu_u = \frac{k_u}{\omega_u} = \frac{f_k k}{f_\omega \omega} \tag{5.6}$$

Evolution equations are derived for the PANS unresolved kinetic energy k_u and the unresolved turbulence frequency ω_u, taking inspiration from the original RANS 1988 Wilcox $k-\omega$ model [51]. The full details of the derivation can be found in [26]. The final form of the PANS $k-\omega$ model equations can be summarized as:

$$\frac{\partial k_u}{\partial t} + \langle u_j \rangle \frac{\partial k_u}{\partial x_j} = P_u - \beta^* k_u \omega_u + \frac{\partial}{\partial x_j} \left[\left(\nu + \frac{\nu_u}{\sigma_{ku}} \right) \frac{\partial k_u}{\partial x_j} \right] \tag{5.7}$$

$$\frac{\partial \omega_u}{\partial t} + \langle u_j \rangle \frac{\partial \omega_u}{\partial x_j} = \alpha \frac{P_u \omega_u}{k_u} - \beta' \omega_u^2 + \frac{\partial}{\partial x_j} \left[\left(\nu + \frac{\nu_u}{\sigma_{\omega_u}} \right) \frac{\partial \omega_u}{\partial x_j} \right] \tag{5.8}$$

The RANS closure coefficients are unchanged for α and β^*, while the remaining closure coefficients are modified as given below:

$$\sigma_{ku} \equiv \sigma_k \frac{f_k}{f_\omega}; \qquad \beta' \equiv \alpha\beta^* - \frac{\alpha\beta^*}{f_\omega} + \frac{\beta}{f_\omega}; \qquad \sigma_{\omega u} \equiv \sigma_\omega \frac{f_k}{f_\omega} \tag{5.9}$$

The user can vary the filter control parameter from a coarse RANS simulation to a fully-resolved DNS simulation, provided that the grid can support such a resolution, to achieve the level of resolution demanded by the user. The derivation of the PANS model is originally performed by Girimaji [10], and it has been applied to numerous flows for validation: [28], [37], [3], [47], [11], and [27].

5.3 Flow Configuration and Numerical Approach

The simulations are performed with the CFD code VULCAN (Viscous Upwind aLgorithm for Complex flow ANalysis). The code was developed and is maintained by researchers at NASA Langley in Hampton, VA. It is a finite volume, turbulent, non-equilibrium, finite-rate chemical kinetics, Navier-Stokes flow solver for structured, cell-centered, multi-block grids. The code is parallelized using MPI, and the majority of the simulations for this work were performed using ~ 500 processors. The present simulations utilized the PANS turbulence model with the Roe upwind scheme and 4th order WENO interpolation, although the code has many other schemes and turbulence models available. The turbulence production-to-dissipation ratio was limited to 200, and the solution was integrated to the wall without the use of any wall functions.

The round leading edge delta wing geometry studied in this work is the 53^o swept, half-span, round leading edge NACA64A006 delta wing of the NATO AVT-183 study. The grid used for this study is the same grid which is employed by all AVT-183 participants. The grid domain extends 5 chord length forward of the wing apex, aft of the wing trailing edge, above the mean chord line, and below the mean chord line of the wing. The sharp leading edge delta wing geometry studied in this work is a 50^o swept, half-span, flat plate delta wing. The grid used for this study is the same 4.48M cell single-block grid which was used for the work of Gordnier

and Visbal [13] but the mesh was refined in the near-wall region. The grid domain extends 1 chord length forward of the wing apex, 1.5 chord lengths aft of the wing trailing edge, and 2 chord lengths above and below the upper and lower surfaces of the wing. Gordnier and Visbal [13] provide a dicussion of the grid development details, including grid refinements which were made in the vortex region to provide adequate flow resolution. While these two delta wing geometries are not a perfect match, their similarity should allow for a good comparison to be made between the sharp and blunt leading edge cases. Further details of the similarities and differences of the two delta wings are presented in Tab. 5.1 and Fig. 5.3. Besides the slight

Table 5.1: Comparison of Sharp and Round Delta Wings

Leading Edge Radius	Total Cells	Leading Edge Sweep	Wall Spacing
Sharp	4.48M	50^o	0.00001 m
Round $r/c = 0.00246$	3.0M	53^o	0.0000052 m

difference in leading edge sweep, the main difference between the two wing geomotries is the presence of the trailing edge sweep of the rounded leading edge wing which is not present in the sharp leading edge wing. However, our study will be restricted to the forward portions of the wing where the vortex first separates which should mitigate any influence from the trailing edge sweep.

The round and sharp leading edge delta wings are simulated with the same numerical scheme and test conditions. We perform computations at $\alpha = 15^o$ and $\alpha = 23^o$ because previous sharp leading edge studies were simulated at these angles of attack and we rely on that data for comparison. The freestream flow conditions used for this work are presented in Table 5.2.

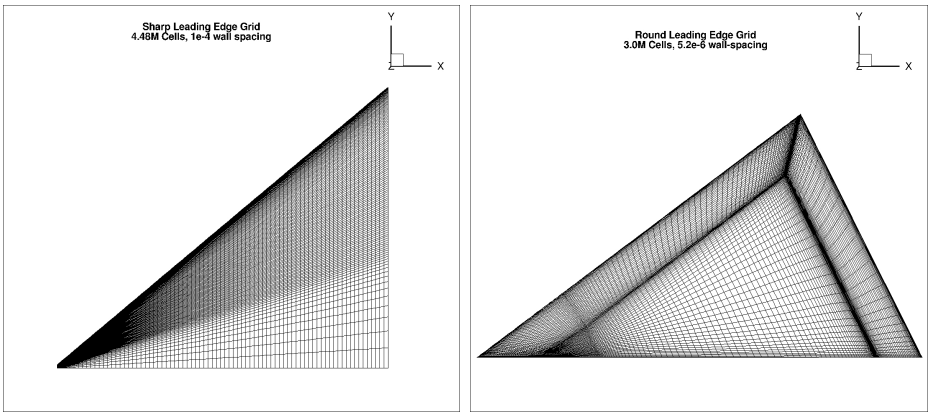

(a) Sharp Leading Edge (b) Round Leading Edge

Figure 5.3: Comparison of Sharp and Round Leading Edge Grids

Table 5.2: Freestream conditions

Mach Number	Reynolds Number	α
0.2	620,000	15^o & 23^o

5.4 Results

The results for the computational simulations are now presented. The $\alpha = 15^o$ simulations are presented first, followed by the $\alpha = 23^o$ simulations.

5.4.1 $\alpha = 15^o$ Results

This section presents a direct comparison of round and sharp leading edge delta wing flow at $\alpha = 15^o$. Figure 5.4 shows the contours of L/η which is the ratio of the largest-to-smallest turbulence length scales in the flow from the URANS simulations. This ratio gives an indication of the width of the turbulence energy spectrum for this flow. The contours for the round leading edge delta wing are presented in the left half

of the plot (Figs. 5.4a and 5.4c), while the sharp leading edge results are presented in the right half of the plot (Figs. 5.4b and 5.4d). The values for L/η are smallest

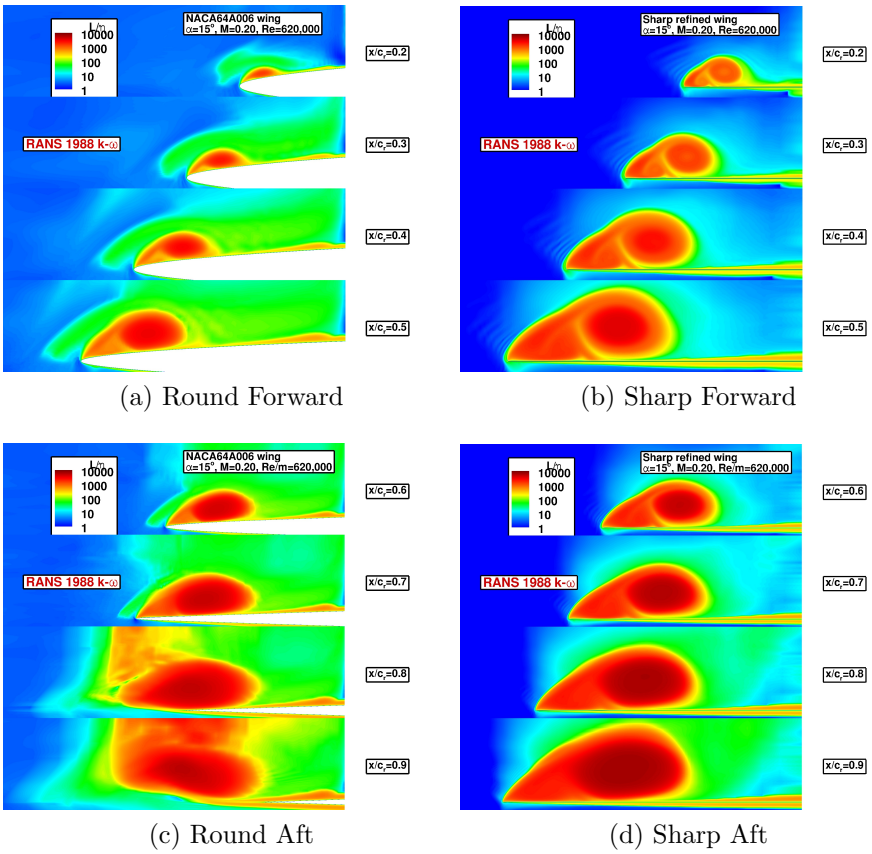

(a) Round Forward (b) Sharp Forward

(c) Round Aft (d) Sharp Aft

Figure 5.4: Contours of L/η at Various Stations Along the Wing; $\alpha = 15^o$

near the wing apex and gradually grow as the flow passes over the wing. There is a somewhat rapid increase in L/η in between $x/c = 0.5$ and $x/c = 0.6$ indicating that vortex breakdown has likely occurred in this range. The sharp leading edge case consistently displays larger L/η values compared to the round leading edge case. This is likely due to the abrupt nature of the primary vortex separation generating

significant levels of turbulence. The contours demonstrate that there is significant separation between the largest and smallest turbulent scales which is indicative of broad-spectrum turbulence, therefore a reduced f_k PANS simulation would be useful.

Following the URANS simulation, PANS simulations are carried out at $f_k = 0.75$, $f_k = 0.5$, and $f_k = 0.3$. The instantaneous axial vorticity for these PANS simulations is shown in Fig. 5.5 at three chordwise stations along the wing: $x/c = 0.2$, $x/c = 0.4$, and $x/c = 0.6$. These locations are chosen for comparison becuase they are all forward of the break in the round leading edge wing. The figures in the left column are round leading edge results while the figures in the right column are sharp leading edge results. The direction of the flow is into the page, and the right edge of the domain is the symmetry plane of the simulation. The well-known primary and secondary vortices can be seen in all of the figures. A reduction in f_k from 1.0 in the URANS case to 0.5 and 0.3 in the subsequent PANS cases provides better resolution of small scale vortical structures in the flow. The secondary vortex seems to play a more dominant role in the sharp leading edge case. While the intensity of the secondary vortex appears to be similar for both the round and sharp leading edge cases, there is more interaction between the primary and secondary vortices in the sharp leading edge case. For example, in the sharp leading edge case at $x/c = 0.4$ the secondary vortex erupts upwards and splits the primary vortex into dual vortices. This eruption and vortex splitting does not occur for the round leading edge case. In general, there is less unsteadiness in the round leading edge case. For both the round and sharp leading edge cases, the tightly-wound primary vortex breaks down sometime between $x/c = 0.4$ and $x/c = 0.6$. The only exception to this observation is the round URANS case which lacks a high intensity primary vortex.

The mean axial velocity contours at the same locations ($x/c = 0.2$, $x/c = 0.4$, and $x/c = 0.6$) are shown in Fig. 5.6. The round leading edge simulation results are

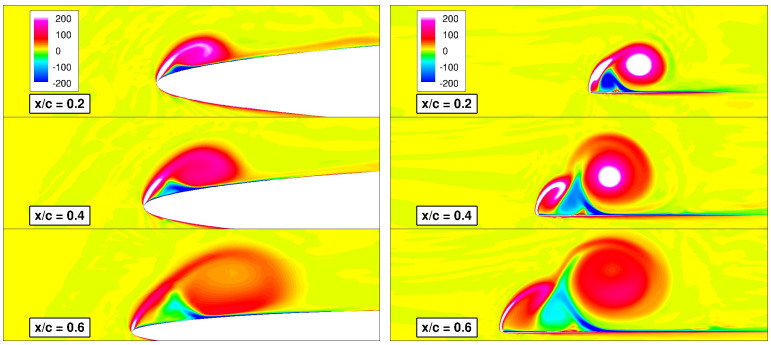

(a) Round URANS (b) Sharp URANS

(c) Round PANS $f_k = 0.5$ (d) Sharp PANS $f_k = 0.5$

(e) Round PANS $f_k = 0.3$ (f) Sharp PANS $f_k = 0.3$

Figure 5.5: Instantaneous Axial Vorticity Contour Comparison

shown in Figs. 5.6a, 5.6c, and 5.6e and the sharp leading edge simulation results are shown in Figs. 5.6b, 5.6d, and 5.6f. It is interesting to note that, in the round leading edge simulations the URANS case does not show a distinct vortex core in the forward

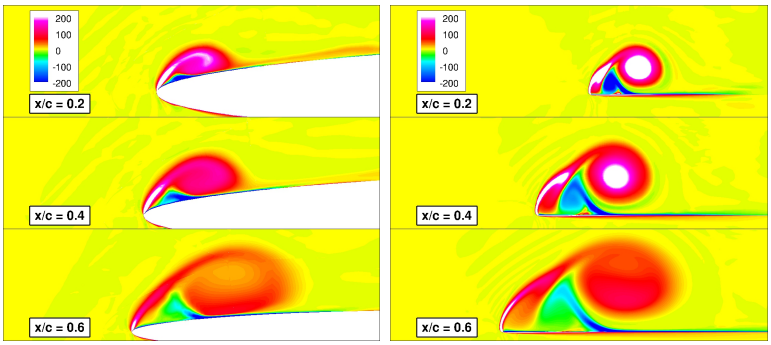

(a) Round URANS (b) Sharp URANS

(c) Round PANS $f_k = 0.5$ (d) Sharp PANS $f_k = 0.5$

(e) Round PANS $f_k = 0.3$ (f) Sharp PANS $f_k = 0.3$

Figure 5.6: Mean Axial Vorticity Contour Comparison

region ($x/c = 0.4$) while the PANS simulations do. The exact opposite is true for the sharp leading edge case: the URANS simulation does show a distinct vortex core at $x/c = 0.4$ while the PANS simulations do not. One possible explanation for this is

that the secondary vortex is much more prominent for the sharp leading edge case, and the PANS simulations liberate the instabilities in the secondary vortex and allow for it to influence and break down the primary vortex core. The secondary vortex clearly plays an active role in splitting the primary vortex into dual vortices in the sharp leading edge case. In the round leading edge case, the secondary vortex is less prominent and the URANS simulation simply dissipates away the vortex core by $x/c = 0.4$. It is somewhat curious that the secondary vortex is weaker for the round leading edge case because as the secondary vortex is forming, the boundary layer encounters an additional adverse pressure gradient in the form of the convex curvature of the wing which should promote a stronger secondary separation. An explanation for why this does not occur is offered in the following paragraph which discusses the surface streamline patterns. Another interesting observation is the presence of the inboard vortex on the round leading edge case. This inboard vortex is only resolved by the PANS simulations.

The mean surface streamlines and C_p are shown in Figs. 5.7. The round leadge edge results are shown on the left-hand side in Figs. 5.7a, 5.7c, and 5.7e while the sharp leading edge results are shown in the right-hand side in Figs. 5.7b, 5.7d, and 5.7f. An interesting observation which is apparent in the streamlines, is that the vortical structures are positioned further outboard for the round leading edge cases compared to the sharp leading edge cases. On explanation for this phenomenon is the thickness associated with the round leading edge wing. The greatest thickness of the wing is found at the wing centerline. Therefore, as the vortex rolls up and inward towards the centerline it is influenced from the growing thickness of the wing and reattaches earlier than it otherwise would without the presence of the thickness. Regardless of the reason for the outboard formation of the vortex structure, the fact that the vortices are confined to a more narrow region of the wing means that

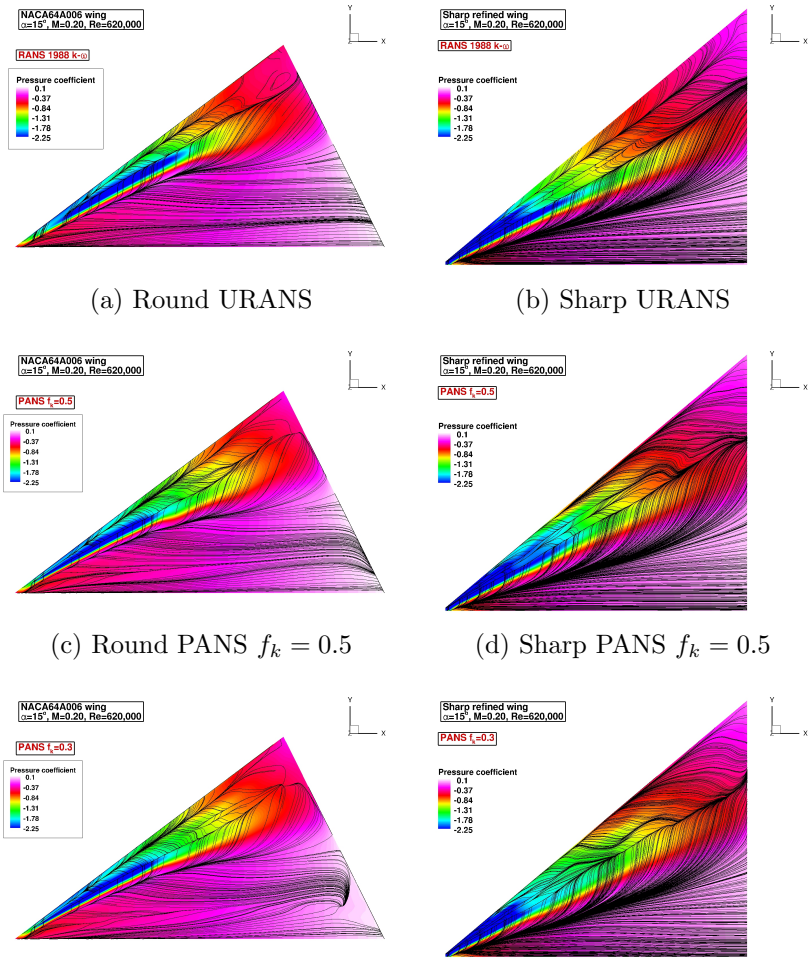

(a) Round URANS (b) Sharp URANS

(c) Round PANS $f_k = 0.5$ (d) Sharp PANS $f_k = 0.5$

(e) Round PANS $f_k = 0.3$ (f) Sharp PANS $f_k = 0.3$

Figure 5.7: Mean Surface Streamlines and C_p; $\alpha = 15^o$

there is less room for secondary and tertiary vortices to form. In fact, there are no tertiary vortices in the round leading edge case while the tertiary vortices are clearly visible in the sharp leading edge mean vorticity plots of Figs. 5.6b, 5.6d, and 5.6f, and the separation and attachment lines of the tertiary vortices are clearly visible in Figs. 5.7b, 5.7d, and 5.7f. The fact that the vortical structures are confined to the outboard reaches of the wing is likely the reason why the seondary vortices in the

round leading edge case are not as prominent as the sharp leading edge case.

A quantitative comparison can be made against the experimental C_p data from the AVT-183 campaign which uses the same geometry and grid as the present simulations. The experimental data was gathered at $Re = 3,000,000$ while the present simulations are performed at $Re = 620,000$, however it is still useful to make a quantitative comparison where available. Figure 5.8 shows the upper and lower surface C_p for the present URANS and PANS simulations compared against the AVT-183 experimental data. First, let us compare the URANS and PANS simulations to one

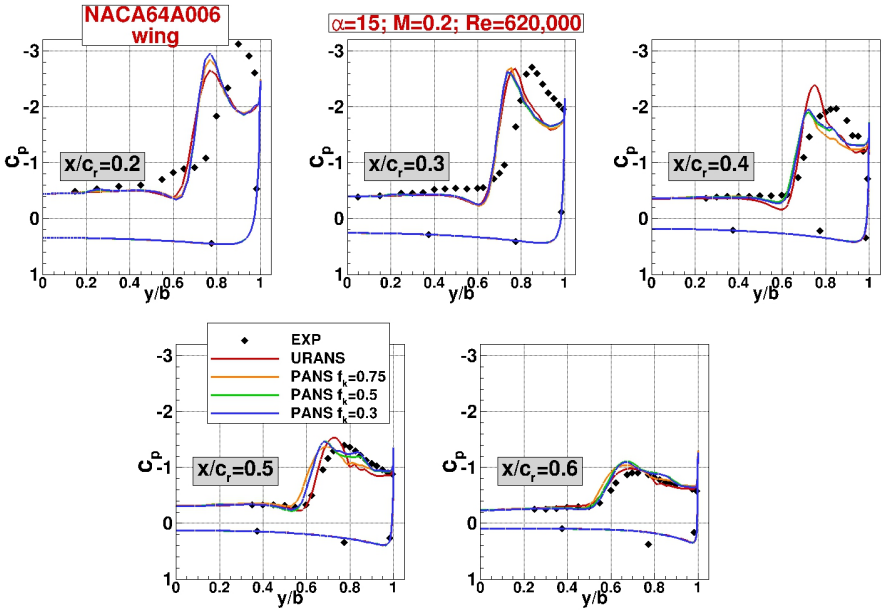

Figure 5.8: Mean Surface C_p vs. AVT-183 Experimental Data ($Re = 3.0M$)

another. At $x/c = 0.2$ there is very little difference between the simulations except at the location of the pressure peaks. The URANS pressure peak is weaker than those of the PANS simulations. Referring back to Fig. 5.6 one can observe that

the lack of a strong primary vortex core in the URANS simulation compared to the PANS simulations is likely the reason for the lower pressure peak in the URANS simulation. At $x/c = 0.3$, all of the present simulations provide essentially the same pressure coefficient. At $x/c = 0.4$, the peak of the URANS C_p is significantly higher than the PANS simulations. Again, if one refers back to Fig. 5.6, while the PANS simulations do show an intense primary vortex, it has moved slightly away from the surface at $x/c = 0.4$ and therefore does not provide the same level of suction as the URANS simulation. Vortex breakdown occurs sometime between $x/c = 0.4$ and $x/c = 0.6$, and the C_p plot at $x/c = 0.5$ demonstrates the disparities which are developing between the URANS and PANS simulations in the complex region. By $x/c = 0.6$ breakdown has occurred, and the pressure peaks are washed out. Moving to a comparison of the present simulations to the experimental data, the first observation is that the pressure peaks of our simulations are consistently inboard from the experimental data. This is an indication that for our lower Reynolds number simulations, the primary vortex core is positioned more inboard compared to a higher Reynolds number simulation. This is consistent with the result shown in Taylor and Gursul [49] for sharp leading edge delta wings.

5.4.2 $\alpha = 23^o$ Near-Stall Results

This subsection presents a comparison of the round leading edge AVT-183 delta wing with the sharp leading edge delta wing at $\alpha = 23^o$ which is a near-stall condition.

We begin by showing the ratio of L/η for a preliminary URANS simulation in order to ascertain the turbulence levels in this flow. Figure 5.9 shows the contours of L/η at several chord-wise stations along the round and sharp leading edge wings. The turbulence spectrum appears to be consistently more broad for the sharp leading edge case with values of L/η on the order of 10,000 as early as $x/c = 0.2$. The

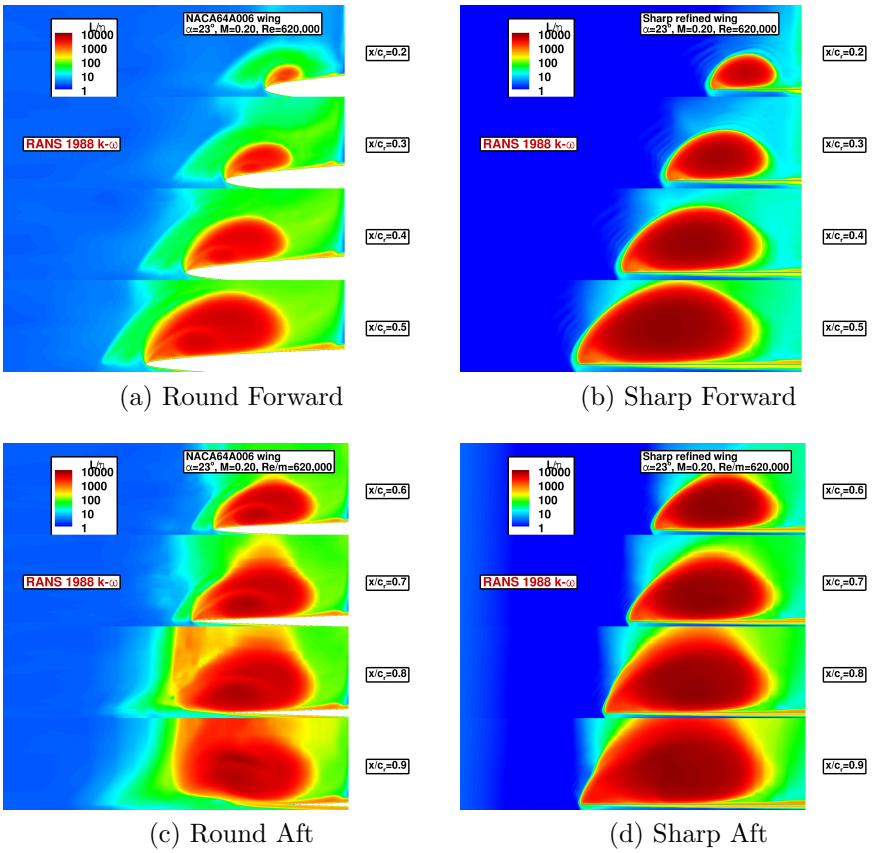

(a) Round Forward (b) Sharp Forward

(c) Round Aft (d) Sharp Aft

Figure 5.9: Contours of L/η at Various Stations Along the Wing; $\alpha = 23^o$

round leading edge case does not show any L/η values at 10,000 until approximately $x/c = 0.5$. The L/η values for this $\alpha = 23^o$ case also appear to be consistently higher than the $\alpha = 15^o$ presented in Fig. 5.4, indicating that the separation is more abrupt and generates higher levels of turbulence at $\alpha = 23^o$. Overall, the turbulence spectrum appears to be sufficiently broad for both the round and sharp leading edge cases to warrant PANS simulations with reduced values of f_k to resolve more of the turbulence spectrum.

The results for the instantaneous axial vorticity for the round and sharp leading edge delta wing simulations are presented in Fig. 5.10 at $x/c = 0.2$, $x/c = 0.4$, and

$x/c = 0.6$. In contrast to the results at $\alpha = 15^o$, for this $\alpha = 23^o$ case there is

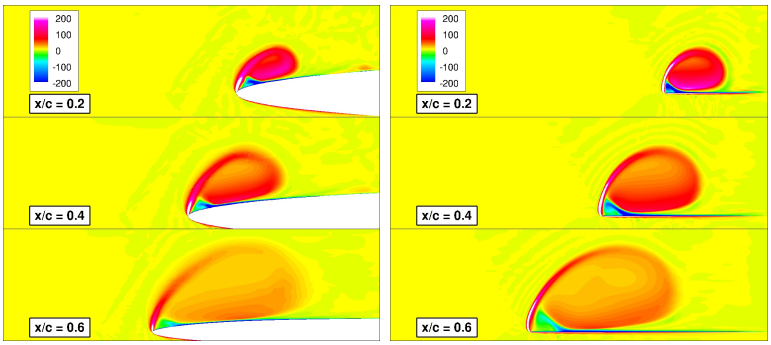

(a) Round URANS (b) Sharp URANS

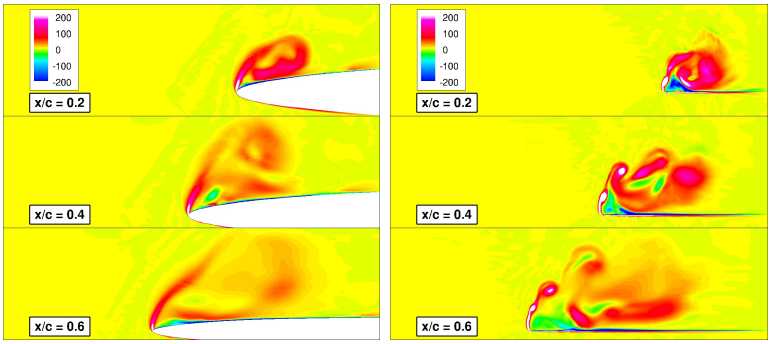

(c) Round PANS $f_k = 0.5$ (d) Sharp PANS $f_k = 0.5$

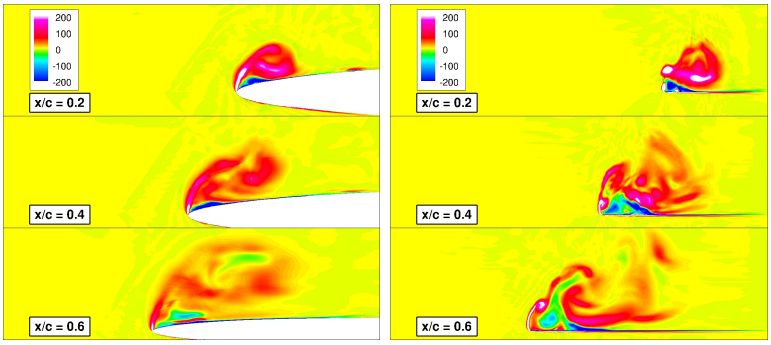

(e) Round PANS $f_k = 0.3$ (f) Sharp PANS $f_k = 0.3$

Figure 5.10: Instantaneous Axial Vorticity at $x/c = 0.2$, $x/c = 0.3$, and $x/c = 0.6$; $\alpha = 23^o$

not a distinct, intense primary vortex core in either the sharp or round leading edge simulations. Instead, the areas of most intense vorticity are concentrated along the circumference of the vortex. There is a distinct increase in the resolution of coherent structures as f_k is reduced from 1.0 in the URANS simulations of Figs. 5.10a and 5.10b to 0.5 in Figs. 5.10c and 5.10d and 0.3 in Figs. 5.10e and 5.10f. The secondary vortex is more prominent in the sharp leading edge case compared to the round leading edge case. The sharp leading edge case also exhibits more unsteadiness than the round leading edge case, likely due to the abrupt nature of the separation from the sharp leading edge and the interaction between the more prominent secondary vortex.

The mean axial vorticity for the $\alpha = 23^o$ case is shown in Fig. 5.11. The round leading edge URANS, PANS $f_k = 0.5$, and PANS $f_k = 0.3$ simulations are shown on the left side in Figs. 5.11a, 5.11c, and 5.11e respectively. The corresponding sharp leading edge results are shown on the right side in Figs. 5.11b, 5.11d, and 5.11f. The lack of an intense primary vortex at $x/c = 0.2$ is an indication that the vortex has already broken down before this location. This is a signature of high angle of attack vortical flows. Instead of an intense core of vorticity, we see an area of weak, positive vorticity in the 'core' of the primary vortex which is surrounded by a perimeter of more intense positive vorticity. Thus in the absence of a strong vortex core, at this high angle of attack, the strong vorticity is confined to a shear layer sheet which rolls up over the upper surface of the wing. This is true for both the round and sharp leading edge cases at all values for f_k. Once again, we see that the secondary vortex is more prominent in the sharp leadge edge case. The lack of a well-defined secondary vortex in the round leading edge case allows the primary vortex to fill in the void where the secondary vortex would have been, which creates a more oval-shaped primary vortex. The effect of this oval shape on the vortex dynamics is

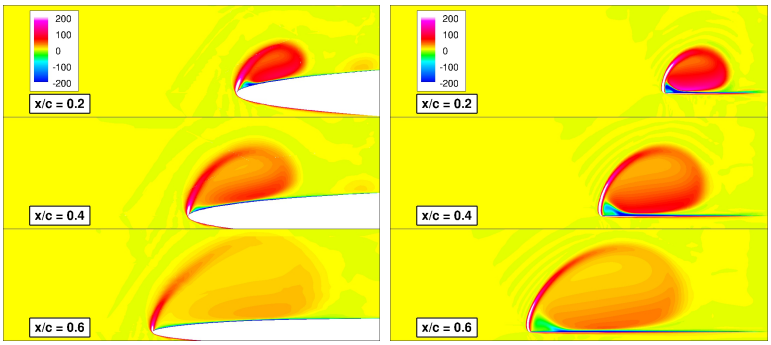

(a) Round URANS (b) Sharp URANS

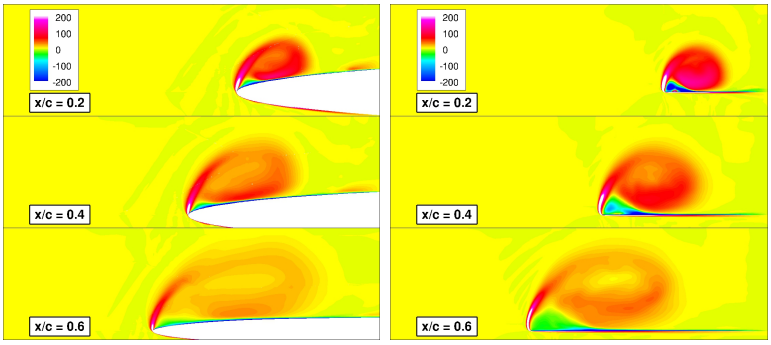

(c) Round PANS $f_k = 0.5$ (d) Sharp PANS $f_k = 0.5$

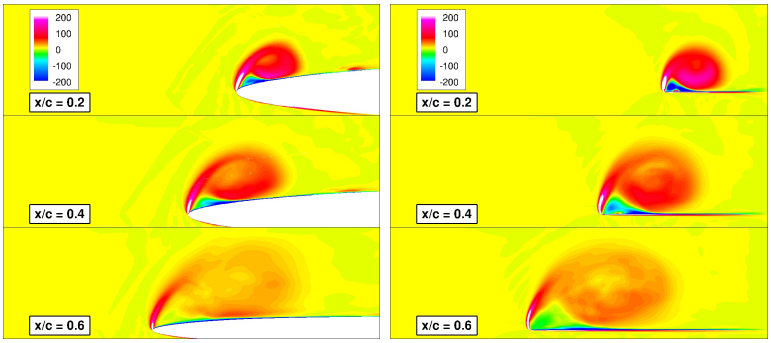

(e) Round PANS $f_k = 0.3$ (f) Sharp PANS $f_k = 0.3$

Figure 5.11: Mean Axial Vorticity at $x/c = 0.2$, $x/c = 0.3$, and $x/c = 0.6$; $\alpha = 23^o$

unclear. The instantaneous results for the URANS simulations in Figs. 5.10a and 5.10b closely resembe the mean results in Figs. 5.11a and 5.11b further illustrating that the URANS simulation is unable to resolve any of the unsteadiness present in

the flow.

The mean surface streamlines and C_p for the $\alpha = 23^o$ cases at $x/c = 0.2$, $x/c = 0.4$, and $x/c = 0.6$ are shown in Fig. 5.12. The round leading edge results are presented in Figs. 5.12a, 5.12c, and 5.12e, while the sharp leadge edge results are presented in Figs. 5.12b, 5.12d, and 5.12f. For this high-α case the dominant feature

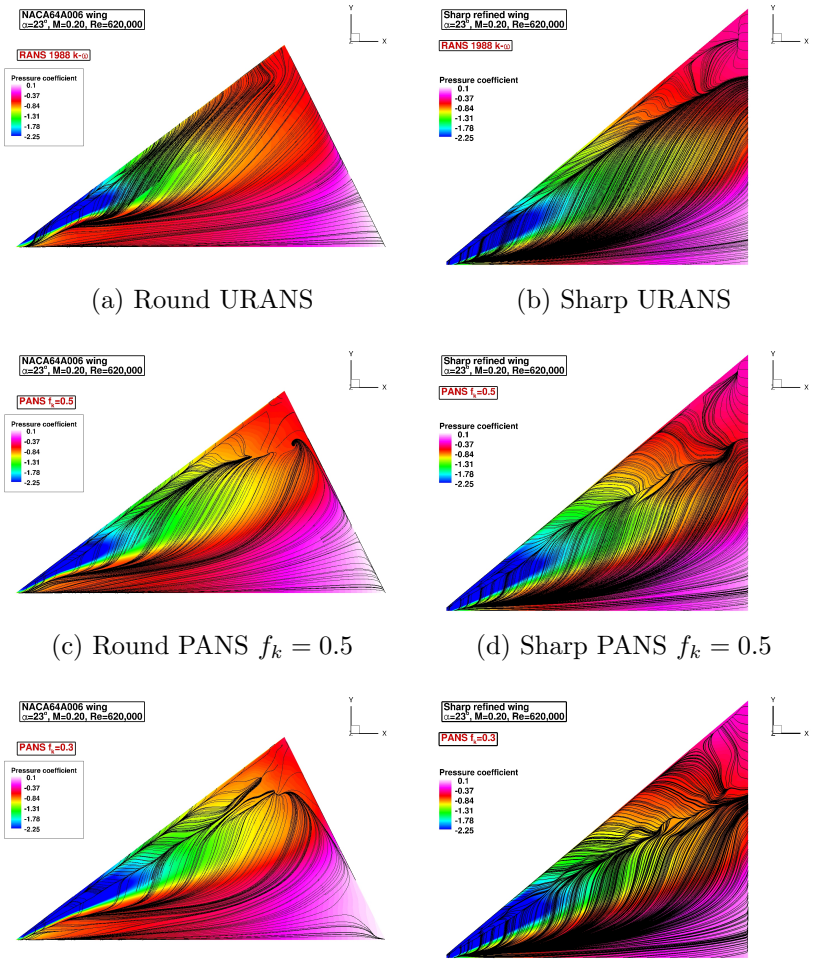

(a) Round URANS (b) Sharp URANS

(c) Round PANS $f_k = 0.5$ (d) Sharp PANS $f_k = 0.5$

(e) Round PANS $f_k = 0.3$ (f) Sharp PANS $f_k = 0.3$

Figure 5.12: Mean Surface Streamlines and C_p; $\alpha = 23^o$

is a very large primary vortex which reattaches near the wing centerline. As was seen in the $\alpha = 15^o$ case, the secondary separation and attachment lines are confined to the outboard regions on the wing and are very narrow. The only tertiary separation or attachment lines which are visible in any of the results are found in an extremely narrow region near the wing apex in the sharp leading egde PANS simulations. This is confirmed by the very small region of positive vorticity beneath the secondary vortex in Figs. 5.11d and 5.11f at $x/c = 0.2$. An interesting features which is observed in the round leading edge streamlines is the abrupt bend in the primary attachment line as the vortex ungoes an expansion at breakdown. This feature is not observed in the sharp leading edge results.

5.5 Summary and Conclusions

This section has explored the differences between the round and sharp leading edge delta wing through the use of URANS and multi-resolution PANS simulations. The key findings of this study are presented in this section. The small inboard vortex reported in literature has been confirmed for the round leading edge case. The URANS simulation was unable to resolve the inboard vortex, but the higher resolution PANS simulations clearly show its presence at both $\alpha = 15^o$ and $\alpha = 23^o$.

The following is a summary of the findings from the $\alpha = 15^o$ simulations. Vortex breakdown occurs between $0.5 < x/c < 0.6$. The sharp leading edge delta wing exhibits a more broad turbulence spectrum, likely due to the more abrupt separation from the sharp leading edge. The turbulence spectrum is significantly wider than previous low Reynolds number ($Re = 26,000$) studies. In the sharp leading edge case, the secondary vortex interacts with the primary vortex much more leading to more unsteadiness and earlier breakdown. URANS simulations predict later breakdown due to the suppression of these unsteady interactions by the URANS model. In the

round leading edge case, the secondary vortex is confined to the outboard region of the wing, possibly due to the thickness of the wing causing a more outboard primary vortex reattachment. The outboard confinement inhibits the development of tertiary vortices for the round leading edge case. We have also confirmed the trend of lower Reynolds number leading to a more inboard location of the primary vortex core.

The findings from the $\alpha = 23^o$ simulations are now summarized. As expected, there is a broader turblence spectrum for the $\alpha = 23^o$ as compared to the $\alpha = 15^o$ case. There is no distinct primary vortex core anywhere aft of $x/c = 0.2$ indicating that breakdown has already occurred forward of this location. The surface streamlines for the round leading edge case indicate a rapid vortex expansion during breakdown. This feature is not observed in the sharp leading edge case. The sharp leading edge case shows a more abrupt separation leading to a more intense shear layer. There is a dramatic increase in the unsteady vorticity structure with increased model resolution. The URANS simulations completely miss this unsteadiness. The mean vorticity is confined to a sheet on the perimeter of the vortex core. The secondary vortex is much smaller in the round leading edge case leading to an oval-shaped primary vortex as it fills in the secondary vortex void. There is no known experimental or high-fidelity computational data available at the near-stall angle of attack. The rich, unsteady flow features which are shown in this study should motivate future study at this critical near-stall condition.

6. CONCLUSIONS

This dissertation has investigated the aerodynamics of delta and diamond wings at low and high angles of attack and Reynolds number using multi-resolution turbulence modeling. The main conclusions of each of the four studies included in this document are summarized in this section.

The first study used RANS modeling to investigate the round leading edge AVT-183 delta wing which is a candidate wing for use on modern UCAVs. RANS simulations were performed and the coefficients of pressure, lift, and drag were investigated along with visualization of the surface streamline patterns. The qualitative aerodynamic trends establised in literature, such as the location of vortex separation moving aft with increasing Reynolds number and moving forward with increasing angle of attack, have been confirmed for the AVT-183 diamond wing. Recent lift and drag coefficient experimental data from the AVT-183 campaign has been reproduced quite accurately. The flight envelope including take-off, ceiling cruise, and combat maneuver conditions have been examined. The RANS model performed well in accurately predicting the lift and drag for low to moderate angles of attack. Near the location of primary vortex separation from the curved leading edge, the RANS model struggles to accurately reproduce the surface pressure coefficient, indicating that higher resolution turbulence models may be needed in these regions.

The second study identified the challenges in applying variable resolution models to separated delta wing flows. While most aerodynamic flows of practical relevance involve high Reynolds numbers, many of the high fidelity experimental and numerical studies are carried out at a much lower Reynolds number. Thus the development of a practical CFD tool can be extensively validated only at low Reynolds number, even

though they are purported for use at significantly higher Reynolds number. In this study we performed URANS and PANS simulations of a low Reynolds number sharp leading edge delta wing flow in order to assess their performance against availabe DNS data. We have demonstrated that a preliminary URANS simulation is beneficial in assessing whether a PANS simulation will provide increased resolution for a particular flow. By studying the contours of turbulent Reynolds number (R_t) and the f_k parameter, it is straightforward to determine if the case will benefit from a PANS simulation. In addition, the f_k contours provide an indication of where an increase in grid resolution may be necessary. The coarse grid results suffer from inadequate grid resolution in the pre-breakdown area. Because of this upstream deficiency, the remainder of the downstream flow was not accurately predicted. The conclusion is that for this type of separated laminar vortical flow, one must "pay the price" and sufficiently resolve the laminar vortex which is present pre-breakdown. Both the fine grid and the coarse grid cases showed some increase in small scale structure in the PANS simulations compared to the more dissipative URANS simulations. To realize the full benefit of higher fidelity closure, the flow must exhibit a broad turbulence spectrum. In many near-laminar unsteady flows with under-developed turbulence spectra, DNS, URANS, and PANS will yield similar results for low order statistics. Future work should be done to simulate separated delta wing flows at high Reynolds number where the increased turbulence levels would make the flow more appropriate for fine resolution modeling.

In the third study, low and high Reynolds number simulations are made of the 50^o-sweep, sharp leading edge delta wing. In the low Reynolds number case, given a grid which we know is adequate for high resolution at that Reynolds number, the laminar flow features can be captured by any model. These flow features include the locations of the vortex core, the separation and reattachment lines, and the C_p up-

stream of vortex breakdown. The turbulent features after breakdown, such as the aft C_p and vortex structure, are dependent upon the model. The lift coefficient, which is derived from the entire surface C_p, appears to also be influenced by the choice of the model. Overall, the differences between URANS and PANS simulations are few due to the narrow turbulence spectrum and the lack of disparity between the largest and smallest turbulence scales. In the high Reynolds number case, given a grid which we know is not adequate for high resolution at that Reynolds number, one cannot expect an accurate C_L prediction and an increased resolution PANS simulation does not improve the computation. If one is interested in unsteady features after breakdown (for purposes of flow buffet, or unsteady aerodynamics) a PANS simulation is required. The flow structures are limited by the grid resolution, but PANS will maximize the utility of a given grid in resolving flow structures. The primay vortex location is such a dominant flow feature that it may be independent of model or grid resolution. The $\alpha = 23^o$ near-stall case showed tremendous unsteadiness and is an excellent example of a condition where PANS is most useful at resolving the unsteadiness. The levels of turbulence seen in the L/η contours are considerably higher than the $\alpha = 15^o$ case. Vortex breakdown occurs within the first 15% of the wing at $\alpha = 23^o$ therefore the vast majority of the flow is dominated by unsteady, broken down vortices. The lift coefficient is dependent upon the model, but also upon the grid resolution. At high Re, the lift coefficient is poorly predicted. Lift coefficient requires a converged grid. The high Reynolds number case lacks a thorough experimental and/or highly resolved computational data set for benchmark quantitative comparisons. Future work should be carried out towards this goal.

The fourth study has explored the differences between the round and sharp leading edge delta wing through the use of URANS and multi-resolution PANS simulations. The small inboard vortex reported in literature has been confirmed for the

round leading edge case. The URANS simulation was unable to resolve the inboard vortex, but the higher resolution PANS simulations clearly show its presence at both $\alpha = 15^o$ and $\alpha = 23^o$. In the $\alpha = 15^o$ simulations, vortex breakdown occurs between $0.5 < x/c < 0.6$. The sharp leading edge delta wing exhibits a more broad turbulence spectrum, likely due to the more abrupt separation from the sharp leading edge. The turbulence spectrum is significantly wider than previous low Reynolds number ($Re = 26,000$) studies. In the sharp leading edge case, the secondary vortex interacts with the primary vortex much more leading to more unsteadiness and earlier breakdown. URANS simulations predict later breakdown due to the suppression of these unsteady interactions by the URANS model. In the round leading edge case, the secondary vortex is confined to the outboard region of the wing, possibly due to the thickness of the wing causing a more outboard primary vortex reattachment. The outboard confinement inhibits the development of tertiary vortices for the round leading edge case. We have also confirmed the trend of lower Reynolds number leading to a more inboard location of the primary vortex core. In the $\alpha = 23^o$ simulations, as expected, there is a broader turblence spectrum compared to the $\alpha = 15^o$ case. There is no distinct primary vortex core anywhere aft of $x/c = 0.2$ indicating that breakdown has already occurred forward of this location. The surface streamlines for the round leading edge case indicate a rapid vortex expansion during breakdown. This feature is not observed in the sharp leading edge case. The sharp leading edge case shows a more abrupt separation leading to a more intense shear layer. There is a dramatic increase in the unsteady vorticity structure with increased model resolution. The URANS simulations completely miss this unsteadiness. The mean vorticity is confined to a sheet on the perimeter of the vortex core. The secondary vortex is much smaller in the round leading edge case leading to an oval-shaped primary vortex as it fills in the secondary vortex void. There is no known experimental

or high-fidelity computational data available at the near-stall angle of attack. The rich, unsteady flow features which are shown in this study should motivate future study at this critical near-stall condition.

REFERENCES

[1] X47 Gallery. http://archive.darpa.mil/j-ucas/X-47/gallery.htm.

[2] Ira H. Abbott and Albert E. von Doenhoff. Summary of Airfoil Data. Technical Report 824, National Advisory Committee for Aeronautics, 1945.

[3] B. Basara, S. Krajnović, and S. S. Girimaji. Partially Averaged Navier-Stokes (PANS) method for turbulence simulation. Accepted to AIAA Journal.

[4] C. Breitsamter and A. Hovelmann. STO-AVT-183 Experimental Force and Pressure Data. Private communication, 2013.

[5] M. Breuer, N. Jovicic, and K. Mazaev. Comparison of DES, RANS and LES for the Separated Flow Around a Flat Plate at High Incidence. *International Journal for Numerical Methods in Fluids*, 41(4):357–388, 2003.

[6] Verhaagen N. G. Leading-Edge Radius Effects on Aerodynamic Characteristics of 50-Degree Delta Wings. *Journal of Aircraft*, 49(2):521531, 2012. doi: 10.2514/1.C031550.

[7] Mohamed Gad-el Hak and RF Blackwelder. The Discrete Vortices From a Delta Wing. *AIAA Journal*, 23(6):961–962, 1985.

[8] Thomas B. Gatski, Christopher L. Rumsey, and Remi Manceau. Current Trends in Modelling Research for Turbulent Aerodynamic Flows. *Philosophical Transactions: Mathematical, Physical and Engineering Sciences*, 365(1859):pp. 2389–2418, 2007.

[9] M Germano. Turbulence: The Filtering Approach. *Journal of Fluid Mechanics*, 238:325–336, 1992.

[10] S. S. Girimaji. Partially-Averaged Navier-Stokes Method for Turbulence: A Reynolds-Averaged Navier-Stokes to Direct Numerical Simulation Bridging Method. *Journal of Applied Mechanics*, 73:413–421, 2006.

[11] S. S. Girimaji, E. Jeong, and R. Srinivasan. Partially Averaged Navier-Stokes Method for Turbulence: Fixed Point Analysis and Comparison with Unsteady Partially Averaged Navier-Stokes. *Journal of Applied Mechanics*, 73:422–429, 2006.

[12] Sharath S Girimaji and Khaled S Abdol-Hamid. Partially Averaged Navier–Stokes Model for Turbulence: Implementation and Validation. *AIAA paper*, 502:2005, 2005.

[13] Raymond E. Gordiner and Miguel R. Visbal. Higher-Order Compact Difference Scheme Applied to the Simulation of a Low Sweep Delta Wing Flow. 41st Aerospace Sciences Meeting and Exhibit, Reno, NV, January 2003.

[14] Raymond E Gordnier. Computation of a Kelvin-Helmholtz Instability for Delta Wing Vortex Flows. Technical report, DTIC Document, 1991.

[15] Raymond E Gordnier. Numerical Simulation of a 65-degree Delta-wing Flowfield. *Journal of Aircraft*, 34(4):492–499, 1997.

[16] Raymond E Gordnier, Miguel R Visbal, Ismet Gursul, and Zhijin Wang. Computational and Experimental Investigation of a Nonslender Delta Wing. *AIAA Journal*, 47(8):1811–1825, 2009.

[17] Gursul Ismet. Unsteady Flow Phenomena Over Delta Wings at High Angle of Attack. *AIAA Journal*, 32(2):225231, 1994. doi: 10.2514/3.11976.

[18] M. Hahn and D. Drikakis. Implicit Large-Eddy Simulation of Swept-Wing Flow Using High-Resolution Methods. *AIAA Journal*, 47(3):618–630, 2009.

[19] K. Hanjalic. Advanced Turbulence Closure Models: a View of Current Status and Future Prospects. *International Journal of Heat and Fluid Flow*, 15(3):178 – 203, 1994.

[20] Dietrich Hummel. On the Vortex Formation Over a Slender Delta Wing at Large Angles of Incidence. Technical Report 15, Technische Universitat Braunschweig, 1978.

[21] Dietrich Hummel. Effects of Boundary Layer Formation on the Vortical Flow Above Slender Delta Wings. Number RTO-MP-AVT-111 in RTO AVT Specialist's Meeting on Enhancement of NATO Military Flight Vehicle Performance by Management of Interacting Boundary Layer Transition and Separation, Prague, Czech Republic, 2004.

[22] Dietrich Hummel. Review of the Second International Vortex Flow Experiment. Number AIAA-2008-377 in AIAA 46th Aerospace Sciences Meeting and Exhibit, Reno, NV, 2008.

[23] J. H. Morrison J. A. White. A Pseudo-Temporal Multi-Grid Relaxation Scheme for Solving the Parabolized Navier-Stokes Equations. *AIAA Journal*, 99(3360):908–922, 1999.

[24] L Christoffer Johansson and R Åke Norberg. Delta-wing Function of Webbed Feet Gives Hydrodynamic Lift for Swimming Propulsion in Birds. *Nature*, 424(6944):65–68, 2003.

[25] John D. Anderson Jr. *Introduction to Flight*. McGraw-Hill, 2000.

[26] S. Lakshmipathy. *Partially Averaged Navier-Stokes Method for Turbulence Closures: Characterization of Fluctuations and Extension to Wall Bounded Flows*. PhD thesis, Texas A&M University, College Station, TX, 2009.

[27] S. Lakshmipathy and S. S. Girimaji. Partially Averaged Navier-Stokes: PANS Method for Turbulence Simulations: Flow Past a Circular Cylinder. *Journal of Fluids Engineering*, 132(121202), 2010.

[28] Sunil Lakshmipathy. PANS Method for Turbulence: Simulations of High and Low Reynolds Number Flows Reynolds Number Flows Past a Circular Cylinder. Master's thesis, Texas A&M University, 2004.

[29] Daniel Levin and Joseph Katz. Dynamic Load Measurements with Delta Wings Undergoing Self-Induced Roll Oscillations. *J. Aircraft*, 21(1):30–36, 1983.

[30] Martin V Lowson. The Three Dimensional Vortex Sheet Structure on Delta Wings. *Fluid Dynamics of Three-Dimensional Turbulent Shear Flows and Transition*, pages 11–1 – 11–16, 1988.

[31] MV Lowson and AJ Riley. Vortex Breakdown Control by Delta Wing Geometry. *Journal of Aircraft*, 32(4):832–838, 1995.

[32] James M. Luckring. Reynolds Number, Compressibility, and Leading-Edge Bluntness Effects on Delta-Wing Aerodynamics. 24th International Congress of the Aeronautical Sciences, Hampton, VA, 2004.

[33] James M. Luckring. A Survey of Factors Affecting Blunt Leading-edge Separation for Swept and Semi-slender Wings. Number AIAA-2010-4820 in AIAA 28th Applied Aerodynamics Conference, Chicago, IL, 2010.

[34] James M Luckring and Okko J Boelens. A Unit-Problem Investigation of Blunt Leading-Edge Separation Motivated by AVT-161 SACCON Research. 2011.

[35] M Menke, H Yang, and I Gursul. Experiments on the Unsteady Nature of Vortex Breakdown Over Delta Wings. *Experiments in Fluids*, 27(3):262–272, 1999.

[36] J Miau, KT Kuo, WH Liu, SJ Hsieh, JH Chou, and CK Lin. Flow Developments Above 50-deg Sweep Delta Wings with Different Leading-edge Profiles. *Journal of Aircraft*, 32(4):787–794, 1995.

[37] Aditya Murthi. Effect of Turbulent Transport Models and Grid Spacing on PANS Calculations of a Lid-driven Cavity. Master's thesis, Texas A&M University, 2004.

[38] Aditya Murthi, D. A. Reyes, S. S. Girimaji, and B. Basara. Turbulent Transport Modeling for PANS and other Bridging Closure Approaches. V European Conference on Computational Fluid Dynamics, Libson, Portugal, June 2010.

[39] Michael V Ol and Morteza Gharib. Leading-edge Vortex Structure of Nonslender Delta Wings at Low Reynolds Number. *AIAA Journal*, 41(1):16–26, 2003.

[40] FM Payne, T Ng, RC Nelson, and LB Schiff. Visualization and Wake Surveys of Vortical Flow Over a Delta Wing. *AIAA Journal*, 26(2):137–143, 1988.

[41] Edward C. Polhamus. Predictions of Vortex-Lift Characteristics by a Leading-Edge Suction Analogy. *Journal of Aircraft*, 8:193–199, 1971.

[42] D.I.A. Poll. Transition in the Infinite Swept Attachment Line Boundary Layer. *Aeronautical Quarterly*, 30:607–629, 1979.

[43] Dasia Ann Reyes. *Advancing the Throretical Foundation of the Partially-averaged Navier-Stokes Approach.* PhD thesis, Doctoral dissertation, Texas A&M University. Available electronically from http://hdl. handle. net/1969. 1/149535, 2013.

[44] Osborne Reynolds. On the Dynamical Theory of Incompressible Viscous Fluids and the Determination of the Criterion. *Philosophical Transactions of the Royal Society of London*, 186:123–164, 1895.

[45] J. Smagorinsky. General Circulation Experiments With the Primitive Equations. *Monthly Weather Review*, 91:99–164, 1963.

[46] B. I. Soemarwoto and O. J. Boelens. Simulation of Vortical Flow over a Slender Delta Wing Experiencing Vortex Breakdown. Technical Report NLR-TP-2003-396, National Aerospace Laboratory NLR, 2003.

[47] C. Song and S. Park. Numerical Simulation of Flow Past a Square Cylinder Using Partially-Averaged Navier-Stokes Model. *Journal of Wind Engineering and Industrial Aerodynamics*, 97:37–47, 2009.

[48] P. R. Spalart, W. H. Jou, M. Strelets, and S. R. Allmaras. Comments on the Feasibility of LES for Wings, and on a Hybrid RANS/LES Approach. In C Liu andZ Liu, editor, *In Advances in DNS/LES*, pages 137–147, Columbus, OH, 1997. Greyden Press.

[49] G. S. Taylor and I. Gursul. Buffeting Flows over a Low-Sweep Delta Wing. *AIAA Journal*, 42(9):1737–1745, 2004.

[50] G. S. Taylor and I. Gursul. Unsteady Vortex Flows and Buffeting of a Low Sweep Delta Wing. *AIAA Journal*, (1066), 2004.

[51] D. C. Wilcox. Reassessment of the Scale-Determining Equation for Advanced Turbulence Models. *AIAA Journal*, 26(11):1299–1310, 1988.

[52] A. Benmeddour X. Z. Huang, Y. Mebarki and T. Brown. Experimental and Numerical Studies of Geometry Effects on UCAV's Aerodynamics. Number AIAA-2004-403 in AIAA 42nd Aerospace Sciences Meeting and Exhibit, Reno, NV, 2004.